

UNIVERSITÀ DELLA CALABRIA



UNIVERSITÀ DELLA CALABRIA

PHYSICS DEPARTMENT

DOTTORATO IN SCIENZE ED INGEGNERIA DELL'AMBIENTE,
DELLE COSTRUZIONI E DELL' ENERGIA
CYCLE XXX

**Search for long-lived neutral particles
decaying into lepton-jets with ATLAS
detector and construction of
MicroMegas SM1 modules**

Del Gaudio Michela

A Dissertation Presented to the
University of Calabria in Candidacy
for the Degree of Doctor of Philosophy

Advisor: Prof. Marco Schioppa

November 2017

UNIVERSITÀ DELLA CALABRIA



UNIVERSITÀ DELLA CALABRIA

PHYSICS DEPARTMENT

DOTTORATO IN SCIENZE ED INGEGNERIA DELL'AMBIENTE,
DELLE COSTRUZIONI E DELL' ENERGIA
CYCLE XXX

Search for long-lived neutral particles decaying into lepton-jets with ATLAS detector and construction of MicroMegas SM1 modules

SSD: FIS/01

External Referees:

Prof. Evangelos N. Gazis (NTU-Athens)

Dr. Philippe Schune (CEA-Saclay, IRFU)

PhD Coordinator: **Prof. S. Critelli**

PhD candidate:

Del Gaudio Michela

Advisor:

Prof. Marco Schioppa

November 2017

To my family

*”Considerate la vostra semenza:
fatti non foste a viver come bruti,
ma per seguir virtute e canoscenza”.*

Dante Alighieri (1265-1321)
Divina Commedia, Canto XXVI

Contents

List of Figures	iv
List of Tables	vii
Nomenclature	viii
Introduction	1
1 Standard Model and beyond	4
1.1 The Standard Model	4
1.1.1 Fermions	5
1.1.2 Interactions and gauge bosons	7
1.2 Standard Model limitations	8
1.3 Some theories beyond the Standard Model	11
2 LHC and the ATLAS detector	14
2.1 The Large Hadron Collider	14
2.2 CERN accelerator complex	18
2.3 The ATLAS detector	21
2.3.1 The coordinate system and kinematic variables	26
2.3.2 The magnet system	28
2.3.3 The Inner Detector	32
2.3.4 The Calorimeters	36
2.3.5 The Muon Spectrometer	41
2.3.6 LUCID	46
2.3.7 The Trigger System	46

CONTENTS

2.4	The Phase-I ATLAS Upgrade	49
3	The Atlas New Small Wheels	52
3.1	Motivation of the Small Wheel Upgrade	52
3.2	The ATLAS New Small Wheel	56
3.3	The MicroMegas detectors	57
3.4	The MicroMegas SM1 quadruplets	62
3.5	Main aspects of the construction procedure	64
3.5.1	Construction of readout panels	66
3.5.2	Construction of drift panels	69
3.5.3	Mesh stretching	70
3.5.4	Quadruplet assembly	72
3.6	Drift panel finalization	73
3.6.1	Finalization-tables	74
3.6.2	Sealing procedure of PCB-PCB junction	76
3.6.3	Positioning of the interconnection drift spacers	78
3.6.4	Local gas tightness test	79
3.6.5	Positioning of mesh-frames	80
3.6.6	Glue dispenser tool	83
3.6.7	Measurement of interconnection drift spacer and mesh- frame height	84
3.6.8	Measurement of panel gas tightness	86
3.6.9	Cold vulcanization of O-Ring and its test	86
3.6.10	Mesh washing: procedure and tools	88
3.6.11	Mesh gluing and tension measurement	89
3.6.12	High voltage test	90
3.6.13	Drift panel finalization work flow	92
3.7	Production status	94
4	Lepton-Jets search	96
4.1	Hidden Sector and Lepton-Jets	96
4.2	The FRVZ benchmark models	98
4.3	Monte Carlo and data samples	100

CONTENTS

4.3.1	Collision data sample	100
4.3.2	Monte Carlo signal sample	101
4.3.3	Empty data samples	102
4.3.4	Monte Carlo background samples	102
4.4	LJ reconstruction	103
4.5	Triggers for LJ selection	107
4.6	FRVZ LJ reconstruction efficiency	108
4.7	Main source of background	111
4.8	Selection requirements on single LJ	113
5	Event selection and systematics	122
5.1	Selection requirements at event level	122
5.2	Results of cut-flow	125
5.3	Systematics uncertainties	127
5.3.1	On standalone muon reconstruction efficiency	127
5.3.2	On Narrow-Scan trigger efficiency	130
5.3.3	Other systematics	131
6	Results and interpretations	132
6.1	Data-driven background estimation	132
6.2	Limits in FRVZ models	136
	Conclusions	141
	Appendices	146
I	Interaction of charged particles with matter	146
II	Gas tightness test of SM1 MicroMegas panel	150
II.a	Gas leak rate specification	150
II.b	The measurement method	151
II.c	Pressure drop correction for temperature	154
II.d	The atmospheric pressure effect on the gas leak	158
	Bibliography	161
	References	161

List of Figures

1.1	Standard Model fundamental particles	5
1.2	Astrophysical anomalies detected by PAMELA	11
2.1	Map of LHC at CERN	14
2.2	LHC integrated luminosity recorded by ATLAS	15
2.3	LHC superconducting magnets	16
2.4	LHC schematic view	17
2.5	CERN accelerator complex	20
2.6	The ATLAS detector	24
2.7	Number of interactions per crossing during the Run-2	26
2.8	The ATLAS Magnet System	31
2.9	The ATLAS Inner Detector	35
2.10	The ATLAS Calorimeter	37
2.11	The ATLAS electromagnetic Calorimeter	38
2.12	The ATLAS hadronic calorimeter	40
2.13	The ATLAS Muon Spectrometer cutview	42
2.14	The ATLAS Muon spectrometer subdetectors	44
2.15	The LUCID detector	46
2.16	The ATLAS trigger system	48
2.17	LHC long term schedule	51
3.1	ATLAS Small Wheel	53
3.2	MDT chamber efficiency as a function of the hit rate	54
3.3	Fake trigger in the end-cap muon spectrometer	54
3.4	Level-1 Muon end-cap trigger rate during Run-2	55

LIST OF FIGURES

3.5	The New Small Wheel	57
3.6	Operation of a MicroMegas detector	58
3.7	Electric field for a MicroMegas	61
3.8	MicroMegas SM1 Module-0	62
3.9	Cross section view of a MM quadruplet	64
3.10	SM1 Module-0 test beam results	65
3.11	Construction of MM SM1 quadruplets	67
3.12	Construction drift and readout panels	68
3.13	Tools used for the readout panel construction	69
3.14	Planarity limbo test for drift panels	71
3.15	Measurement of the tension of a mesh	72
3.16	Exploded view of a SM1 drift panel	75
3.17	Finalization-table	75
3.18	Finalization-table for gluing the mesh on drift panel	76
3.19	Finalization-table for the gas tightness test	77
3.20	Interconnection system	78
3.21	Positioning of interconnection drift spacers	79
3.22	Tester head for local gas tightness test	81
3.23	Mesh-frames positioners	82
3.24	Mesh-frames glue curing	82
3.25	Glue dispenser tool	83
3.26	Measurements of interconnection drift spacers and mesh-frames height	84
3.27	Mesh-frames height measurement	85
3.28	Measurement of interconnection drift spacers	85
3.29	Measurement of panel gas tightness	87
3.30	O-Ring cold vulcanization	88
3.31	Mesh washing cabin	89
3.32	Drawing of mesh gluing on drift panel	91
3.33	Mesh tension test	91
3.34	HV test on drift panels	92
4.1	γ_d branching ratio as a function of its mass	98

LIST OF FIGURES

4.2	Generic LJ compositions	99
4.3	The FRVZ benchmark models	100
4.4	Classification of displaced LJs	103
4.5	Muonic LJs angular opening distribution	105
4.6	Number of reconstructed jets per LJ	106
4.7	Reconstruction eff. for $\gamma_d \rightarrow \mu\mu$ for $H \rightarrow 2\gamma_d + X$ model	109
4.8	Reconstruction eff. for $\gamma_d \rightarrow ee(\pi\pi)$ for $H \rightarrow 2\gamma_d + X$ model	112
4.9	Source of background	114
4.10	Jet EM fraction distribution	115
4.11	Jet width distribution	116
4.12	Jets η distribution in the calorimeter transition region	118
4.13	Jet timing distribution	119
4.14	Muon impact parameter distribution	120
5.1	Isolation of LJ tracks in ID	123
5.2	Azimuthal angle between two LJs	125
5.3	Systematics on standalone muon reconstruction efficiency	129
6.1	ABCD method	134
6.2	γ_D detection efficiency as a function of $c\tau$	137
6.3	95% upper limits on the $\sigma \times \text{BR}$ for 125 GeV Higgs	139
6.4	95% upper limits on the $\sigma \times \text{BR}$ for 800 GeV Higgs	140
6.5	Exclusion limits for 800 GeV Higgs assuming $\sigma \times \text{BR} = 10$ pb	140
6	Energy loss curve for a charged particle	148
7	Electron avalanche	148
8	Gas volume in the vessel as a function of the overpressure	152
9	Set up used for the gas tightness test	153
10	overpressure monitoring	154
11	Logarithmic PV as a function of time	157
12	Air leak after temperature correction	158
13	Pressure of gas as a function of temperature	158
14	Air temperature as a function of time	159
15	Atmospheric pressure as a function of time	159

List of Tables

2.1	LHC performance parameters.	19
2.2	Magnet system main parameters	29
2.3	Parameters of ATLAS Inner Detector	33
2.4	The ATLAS calorimeters energy resolution	39
3.1	NSW MicroMegas performance parameters	60
3.2	MicroMegas construction requirements	65
4.1	Parameter of the FRVZ benchmark models	101
4.2	Trigger efficiency for FRVZ MC samples	108
4.3	Selection requirement on single LJ	121
5.1	Cut-flow results on data	126
5.2	Systematic uncertainties	127
6.1	Results of full cut-flow on data	135
6.2	Summary of ABCD and full cut-flow results on data	135
6.3	Results of full cut-flow on MC samples	136

Nomenclature

<i>T&P</i>	Tag-and-Probe
ALFA	Absolute Luminosity For ATLAS
ALICE	A Large Ion Collider Experiment
ATLAS	A Toroidal Lhc ApparatuS
BIB	Beam Induced Background
BR	Branching Ratio
BSM	Beyond of the Standard Model
BT	Barrel Toroid
CERN	Conseil européen pour la recherche nucléaire
CLIC	Compact Linear Collider
CMM	Coordinate Measuring Machine
CMS	Compact Muon Solenoid
CNGS	CERN Neutrinos to Gran Sasso
CS	Central Solenoid
CSC	Cathode Strip Chambers
dLJ	displaced Lepton-Jet

NOMENCLATURE

DM	Dark Matter
EC	End-Cap
ECal	Electromagnetic CALorimeter
ECT	End-Cap Toroid
EF	Event Filter
EM	ElectroMagnetic
EMEC	ElectroMagnetic LAr End-Cap calorimeter
FCal	Hadronic LAr Forward Calorimeter
FRVZ	Falkowski-Ruderman-Volansky-Zupan
FTK	hardware Track Finder
GRL	Good Run List
GUT	Grand Unified Theory
HCal	Hadronic Calorimeter
HEC	Hadronic LAr End-Cap calorimeter
HEP	High Energy Physics
HLSP	Hidden Lightest Stable Particle
HLT	High Level Trigger
HS	Hidden Sector
HV	High Voltage
IBL	Insertable B-Layer
ID	Inner Detector
ISOLDE	Online Isotope Mass Separator

NOMENCLATURE

JVT	Jet Vertex Tagger
L1	Trigger Level-1
LAr	Liquid Argon
LEIR	Low Energy Ion Ring
LHC	Large Hadron Collider
LHCb	Large Hadron Collider beauty
LINAC2	Linear Accelerator2
LJ	Lepton-Jet
LNF	Laboratori Nazionali di Frascati
LS1	First Long Shutdown
LS2	Second Long Shutdown
LUCID	LUMinosity measurement using Cherenkov Integrating Detector
MC	Monte Carlo
MDT	Monitor Drift Tube
MET	Transverse Missing Energy
MicroMegas	Micro-MESH Gaseous Structure
MM	MicroMegas: Micro-MESH Gaseous Structure
MS	Muon Spectrometer
NMSSM	Next-to-Minimal Supersymmetric Standard Model
non-CB	non-combined
NSW	New Small Wheel

NOMENCLATURE

nTOF	neutron time-of-flight facility
PMTs	Photomultipliers
PS	Proton Synchrotron
PSB	Proton Synchrotron Booster
QA/QC	Quality Assurance/Quality control
QA/QC	Quality assurance and Quality Control testing
QCD	Quantum ChromoDinamics
RASNIK	Red Alignment System of NIKhef
RoI	Region of Interest
RPC	Resistive Plate Chambers
SCT	SemiConductor Tracker
SI	Internasional System of units
SM	Standard Model
SP	Separation Power
SPS	Super Proton Synchrotron
sTGC	small strip Thin Gas Chambers
SUSY	SUper SYmmetric model
TDAQ	Trigger DAta acQuisition system
TGC	Thin Gap Chambers
TileCal	Tile Calorimeter
TRT	Transition Radiation Tracker
UEH-LLP-LJ	Unconventional Exotic Long Lived Particles LJ
ZDC	Zero-Degree Calorimeter

Introduction

The Standard Model (SM) is a quantum field theory developed in the second half of the 20th century by Weinberg and Salam using Glashow's idea and Higgs contribution. It is a renormalizable non-abelian gauge theory which classifies all known elementary particles: the *fermions*, which are fundamental spin $\frac{1}{2}$ particles constituting the matter, and the *bosons*, which are integer spin particles. Furthermore the SM theory describes with great precision three of the four fundamental interactions of particles: the strong, weak and the electromagnetic forces.

The SM represents one of the greatest achievements for particle physics indeed, in the last years many high energy physics (HEP) experiments confirmed the SM agreement with the experimental data. The last important achievement was the discovery of the Higgs boson in the 2012 made at CERN by ATLAS and CMS experiments.

Despite of the important fulfillments, the Standard Model faces serious problem: it does not include gravity, it has too many free parameters, and it fails to high energies. For these and other causes, it is necessary to built a theory beyond the Standard Model (BSM), which leads to the same correct SM predictions without its issues.

An example of BSM theory are SUSY(SUper SYmmetric model), the NMSSM (Next-to-Minimal Supersymmetric Standard Model), the GUT (Grand Unified Theory) and others. In this work a light *Hidden Sector* (HS) is considered as BSM model.

The Hidden Sector is a sector weakly coupled to the SM, and the most simple modelling consists of U(1) simmetry. The corresponding hidden pho-

ton, also called *dark photon* kinetically mixes with the ordinary photon and produces, in the final state, collimated SM particles with *Lepton-Jets* structures. The search displayed in this thesis is largely model independent with a general definition of LJ. The aim is finding a set of selection criteria to isolate the LJ signature from background, and also to set upper limits on non-SM Higgs boson decays to LJs according to a specific Hidden Sector model (the Falkowski-Ruderman-Volansky-Zupan model).

Currently, the ATLAS detector is non designed for exotic physics searches which predict the existence of long lived particles. In fact, the ATLAS standard triggers require tracks pointing to the proton-proton interaction point, moreover, the ATLAS reconstruction capabilities are not designed to detect particles with very small angles. For this reason, in order to improve the detector capabilities for searches beyond the Standard Model, the ATLAS Collaboration planned a Phase-II upgrade 2024 – 2027. One sub-detector system that will be implemented in the Phase-II upgrade improving the exotics physics searches is the New Small Wheels, which will be installed during the Phase-I upgrade in the inner part of the end-cap Muon Spectrometer.

The description of the emphNew Small Wheels (NSW), and of the construction of one of its detector constituents: the MicroMegas SM1 detectors is the second research activity presented in this thesis The *MicroMegas* are gaseous detectors that will be installed in the End-Cap muon spectrometer as part of the *New Small Wheels* during the Phase-I upgrade (2019-2020). The upgrade aims to improve the detector performance at high luminosity ($2 \times 10^{34} \text{ cm}^{-2} \text{ s}^{-1}$) installing a set of precision tracking and trigger detectors able to work at high rates of particles. Each MicroMegas detector has trapezoidal shapes with surface area between 2 and 3 m², the spatial resolution is better than 100 μm and the rate capability is up to 15 kHz/cm². It is the first time that large resistive MicroMegas detectors are employed in HEP experiment. Moreover the challenge of this technology lies in the high mechanical and construction precision needed to achieve the required 15% transverse momentum resolution for 1 TeV muons.

This thesis is summarized as follow:

Chapter 1 describes the main concepts of the Standard Model and its main issues, focusing on the Beyond Standard Model theories.

Chapter 2 describes the Large Hadron Collider and the ATLAS detector showing all the sub-detectors.

Chapter 3 describes the MicroMegas detector technology and the New Small Wheels, focusing on the construction and QA/QC tests of SM1 modules.

Chapter 4 focuses on the Hidden Sector and Lepton-Jets search, showing the Falkowski-Ruderman-Volansky-Zupan models used in this thesis, the data and Monte Carlo samples, and the trigger applied.

Chapter 5 presents the procedure to select the dark photon signature and to estimate the background.

Chapter 6 presents the Lepton-Jets search results on proton-proton collisions at $\sqrt{s} = 13$ TeV center of mass energy collected by ATLAS experiment during 2015 data taking.

CHAPTER 1

Standard Model and beyond

1.1 The Standard Model

The *Standard Model* (SM) is a non-Abelian and renormalizable theory, which is invariant under the $SU(3) \times SU(2) \times U(1)$ gauge transformations. It describes three of four fundamental forces (the electromagnetic, weak, and strong interactions) as well as it defines all the elementary particles currently known. Presented in the late 60s, the Standard Model finds its pillar from electro-weak unification, explained by Weinberg and Salam using the spontaneous symmetry breaking, which leads to the introduction of the weak boson mediators.[1][2] The spontaneous symmetry breaking was also used by Higgs (and independently by Brout and Englert) as mechanism by which particles get masses in order to obtain a renormalizable theory. Indeed, the Higgs mechanism allows to avoid the problem of the Goldstone theorem (associated to the spontaneous symmetry breaking) introducing a gauge field called the *Higgs field*: a scalar spin 0 field which permeates all universe. The proof of the validity of Higgs mechanism was the discovery of the Higgs boson in 2012 by the ATLAS and CMS experiments at CERN.

1.1. THE STANDARD MODEL

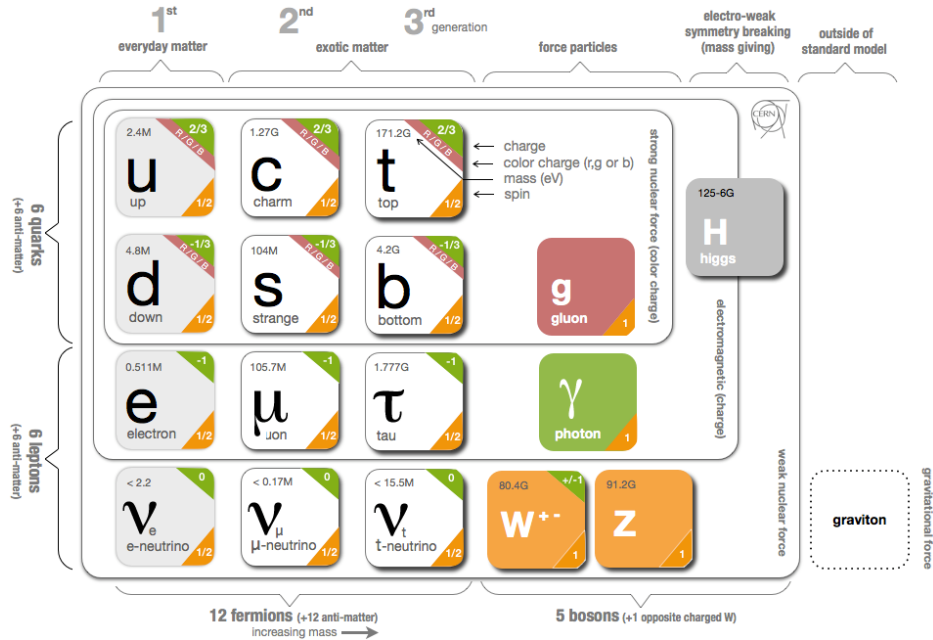


Figure 1.1: Scheme of fundamental particles and interactions included in the Standard Model. The graviton boson, which is not yet experimentally observed, is reported too.

1.1.1 Fermions

The SM establishes that all known matter is made of elementary particles which obey the Fermi-Dirac statistics: the **fermions**. Fermions are $\frac{1}{2}$ spin particles and they are divided in two main classes: **quarks**¹ and **leptons**².^[5] Each class consists of six particles related in pairs, usually called *generations*. The first generation, constituted by the lightest and most stable particles, makes up all the stable matter in the universe, while the other two generations

¹Regarding the quark name, Gell-Man in his book said: «In 1963, when I assigned the name “quark” to the fundamental constituents of the nucleon, I had the sound first, without the spelling, which could have been “kwork”. Then, in one of my occasional perusals of Finnegans Wake, by James Joyce, I came across the word “quark” in the phrase “Three quarks for Muster Mark”»... «the number three fitted perfectly the way quarks occur in nature.»^[3]

²“From $\lambda\epsilon\pi\tau\omicron\varsigma$ which means small, thin, delicate to denote a particle of small mass. Today definition has nothing to do with the mass of the particles but only with the fact that leptons do not have strong interaction but only weak interaction, and, when electrically charged, also electromagnetic interactions.”^[4]

1.1. THE STANDARD MODEL

are constituted by heavier and less stable particles, see Fig. 1.1.

In particular, the six leptons are paired in three generations corresponding to three *leptonic flavours*: the electron (e^-) and electron neutrino (ν_e), the muon (μ^-) and muon neutrino (ν_μ), the tau (τ^-) and tau neutrino (ν_τ). The SM establishes that electron, muon and tau are massive and electrically charged leptons (with negative charge $-e$ where $e \equiv 1.6 \times 10^{-19}$), while **neutrinos**³ are massless with no electrical charge. Moreover all leptonic particles have *weak isospin*, in particular for the left-handed leptonic particles (which are the only experimentally discovered leptons) it is $\pm\frac{1}{2}$. Additionally to these features, the SM indicates that each leptonic generation is characterized by a specific *leptonic number* which is conserved. Electron and electron neutrino have an electronic number $L_e = 1$, muon and muon neutrino have a muonic number $L_\mu = 1$, while tau and tau neutrino have tauonic number $L_\tau = 1$. The conservation of the individual leptonic numbers $L_e = 1$ implies that the number of leptons of the same type remains the same.

The SM indicates that for each leptonic particles there is an antileptonic particle: e^+ , μ^+ , μ^+ , $\bar{\nu}_e$, $\bar{\nu}_\mu$, $\bar{\nu}_\tau$. Each *antilepton* differs from the lepton only because some of its properties have equal magnitude but opposite sign⁴.

On the other hand, the quarks are massive particles with fractional electrical charge of $+\frac{2}{3}e$ or $-\frac{1}{3}e$, carry also weak isospin of $\pm\frac{1}{2}$. Like leptons, the quarks are classified in three generations of particles: up (u) and down (d), strange (s) and charmed (c), top (t) and bottom (b). In order to keep valid the Pauli principle for quark composites, quarks have a *quantum number colour* which can assume three values: red, blue and green.[6] The SM establishes that only color-neutral particles can exist as free particle, there-

³“The name ‘neutrino’ (a funny and grammatically incorrect contraction of ‘little neutron’ in Italian: *neutronino*) entered the international terminology through Fermi, who started to use it sometime between the conference in Paris in July 1932 and the Solvay Conference in October 1933 where Pauli used it. The word came out in a humorous conversation at the Istituto di Via Panisperna. Fermi and Amaldi discussed about the Pauli’s hypothesis of ‘light neutron’. For distinguishing this particle from the Chadwick neutron Amaldi jokingly used this funny name.”[4]

⁴Regarding neutrinos, there are not yet enough experimental observations to conclude if they are Dirac or Majorana fermions, i.e. if they are their own antiparticles.

fore quark can't be isolated but they are found only within **hadrons**⁵. This phenomenon, known as *color confinement*, allows only the formation of color-neutral hadronic particles like *mesons* (which are constituted by a quark and an antiquark), and *baryons* (which consists of three quarks). Similarly to the leptons, the SM establishes that for every quark flavour there is a corresponding type of *antiquark* denoted with the symbols \bar{u} , \bar{d} , \bar{s} , \bar{c} , \bar{t} , \bar{b} . The antiquarks differ from the quark only because some of its properties have equal magnitude but opposite sign.

1.1.2 Interactions and gauge bosons

The Standard Model describes three of the four fundamental interactions between the fermion constituents, as resulting of exchanging force-carrier particles which are *gauge bosons*. As shown in Fig. 1.1, for each fundamental force there is a gauge boson: the massless *gluons* for the strong interaction, the *photon* for the electromagnetic one, the massive W^\pm and Z^0 bosons for the weak interaction and finally the graviton, which is not yet observed, is supposed to be the massless spin 2 gauge boson of gravity.

The SM includes:

- the **strong interaction** (or strong nuclear force) between “coloured” particles like quarks and gluons at a range of $\sim 10^{-15}$ m. It is responsible for the confinement of quarks in hadrons, and also of binding protons and neutrons in the atomic nuclei.
- the **weak interaction** (or weak nuclear force) which acts only on leptons and quarks and it is responsible for radioactive decay and nuclear fission.
- the **electromagnetic interaction** affects only the electrical charged particles and it is responsible for extra-nuclear physics phenomena like interactions among atoms or molecules. As already said, in the late of

⁵Strongly interacting particles. From Greek $\alpha\delta\pi\omicron\varsigma$ which means large, massive, in contrast to $\lambda\epsilon\pi\tau\omicron\varsigma$.

1.2. STANDARD MODEL LIMITATIONS

60s the description of electromagnetic and weak forces was unified in the *electro-weak interaction*.

The last fundamental force is the **gravity** which is not included in the SM theory. Although all massive particles undergo gravitational interactions, it is negligible at quantum level.

1.2 Standard Model limitations

Although the Standard Model has demonstrated huge successes in providing experimental predictions, it is not a complete theory.[7] Indeed it leaves many unanswered theoretical questions and unexplained experimental phenomena which are considered as a smoking gun evidence for physics beyond the SM.

Here a list of the main SM limitations:

- the SM does not explain why the fundamental particles are divided in three generations and why all matter only consists of first generation quarks.
- The SM Lagrangian depends on **19 free parameters** (6 quark masses, 3 lepton masses, 3 CKM mixing angles, the CKM CP-violating Phase, 3 gauge couplings, the QCD vacuum angle, the Higgs vacuum expectation value and the Higgs mass) which are not predicted by the theory but only experimentally obtained.
- The SM is supposed to be a low energy effective theory of a more general theory valid at the Planck scale⁶. Indeed at Planck energy the coupling constants should be unified, and a grand unified theory (GUT) must be used. Therefore, there are two very different scales: the electroweak breaking scale (~ 100 GeV) and the grand unification scale ($\sim 10^{19}$ GeV). The huge difference between these two scales is indicated

⁶The Planck scale is constituted by values of mass, energy, time and length for which the gravitational quantum effects are not negligible: $M_P \sim 10^{-8}$ kg, $E_P \sim 10^{19}$ GeV, $t_P \sim 10^{-44}$ s and $l_P \sim 10^{-35}$ m

1.2. STANDARD MODEL LIMITATIONS

as **hierarchy problem** or “naturalness problem”. Moreover, there is the problem of Higgs mass instability to high energies caused by the presence of quadratic divergences ($\propto \Lambda^2$) in the quantistic corrections of Higgs mass parameter.[8]

- As already said, the SM does not describe phenomena at the Planck energy scale ($\sim 10^{19}$ GeV). At this energy level, in fact, the gravity is not renormalizable, then no longer negligible. Therefore the SM does not include one of the four fundamental interactions: the **gravity**.
- The SM does not solve the matter-antimatter asymmetry in the universe which leads to an imbalance between barionic and antibarionic matter, usually known as **baryogenesis**. [7]
- Despite of the SM indications for which neutrinos are massless, in 1998 was observed for the first time, the **neutrino oscillation**. Predicted in 1957 by Bruno Pontecorvo, it implies that neutrino has non-zero mass, moreover this process violates the conservation of the individual leptonic numbers (still preserving the conservation of the total leptonic number).
- In the SM, each lepton ($l = e, \mu, \tau$), as Dirac fermion, has a magnetic moment along its spin, given by

$$\vec{\mu}_l = g_l \frac{Q}{2m_l} \vec{s} \quad (1.1)$$

where m_l is the lepton mass, $Q = \pm e$ is the electric charge and g_l is a dimensionless quantity called *g-factor*. The Dirac theory predicts that for all leptons $g_l = 2$, but from the experimental observations it is known to be greater than 2. Theoretically, the SM explains this small deviation, called *anomaly*, with respect to the Dirac value as quantum fluctuations, therefore the g-2 factor can be defined as:

$$g_l = 2(1 + a_l), \quad a_l = \frac{g_l - 2}{2} \quad (1.2)$$

1.2. STANDARD MODEL LIMITATIONS

where a_l represents the anomaly. Unfortunately the experimental value of the muon magnetic moment does not confirm the theoretical SM predictions, also taking into account the anomaly. In particular, between the theoretical value and the experimental observations made at Brookhaven National Laboratory, there is a difference of 3 – 4 standard deviations.[9] This phenomenon, known as **muon anomalous magnetic dipole moment**, is one of the most compelling indicators of physics beyond the SM.

- The SM does not explain the nature of the **Dark Matter**⁷ even if, from cosmological observations the dark energy makes up approximately the 68% of the universe. The dark energy, indeed, is evenly distributed throughout the universe, therefore it does not have any local gravitational effects, but it does have a global effect on the whole universe.[10] Two of the most known astrophysical anomalies which may constitute indirect evidence of DM coming from the PAMELA and FERMI satellites. Indeed both the experiments detected an excess of leptonic cosmic-rays which could be explained assuming DM annihilations.[11][12]

In particular, PAMELA is a Russian satellite with the purpose of studying the cosmic radiation in the range 1.5 – 100 GeV. As shown in Fig. 1.2, PAMELA has detected in the range 10 – 100 GeV an excess of positron fraction $\left(\frac{N_{e^+}}{N_{e^+}+N_{e^-}}\right)$ with respect to the electrons fraction. This abundance of cosmic-ray positrons is not explained by the SM, for which the cosmic positrons are generated by the “secondary production”, i.e., by interactions between cosmic-ray nuclei and interstellar matter.

On the other hand, the FERMI satellite is a gamma-ray space telescope launched into the space in 2008, which observed an excess of e^+e^- cosmic-rays with respect to the SM predictions, at energies above 1 TeV.

⁷Dark Matter and dark energy are different concepts. Dark Matter is responsible for the unexpected rotational speed of galaxy, while dark energy answers the increasing linear acceleration of the galaxies.

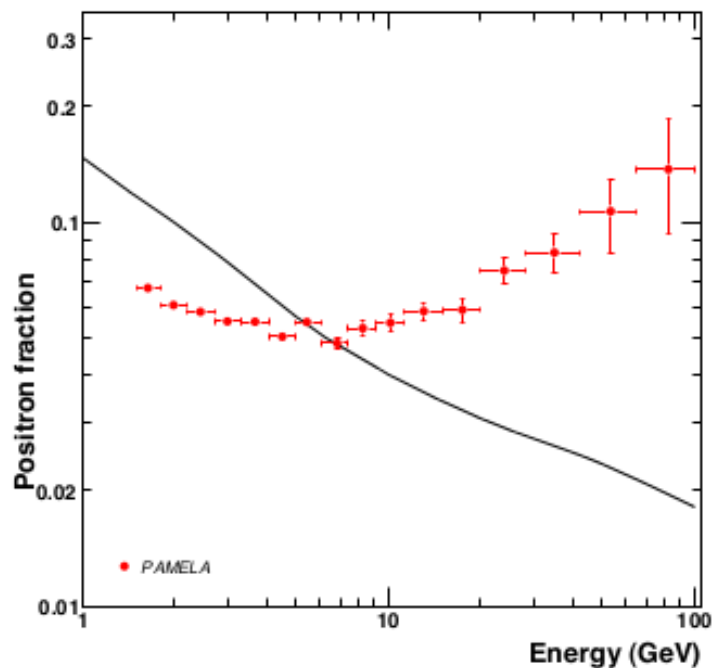


Figure 1.2: Picture showing the comparison between the positron cosmic-ray fraction observed by PAMELA (red points) and the SM expected one calculated according to the mechanism of secondary production (black curve). Data and theoretical expectation disagreed in the whole studied cosmic ray energy range, except the energy interval 5-7 GeV.

As will be described in the chapter 4, a possible explanation for these anomalies consists to suppose that the DM is charged under a hidden sector. Therefore the DM can annihilate into the hidden sector gauge boson, called dark photon γ_D , which can decay back to the SM. If the dark photon is light ($m_{\gamma_D} \sim \mathcal{O}(1 \text{ GeV})$) the annihilation rate obtained can explain the PAMELA and FERMI anomalies.[13]

1.3 Some theories beyond the Standard Model

Physics beyond the Standard Model (BSM) refers to the theories developed to solve the Standard Model limitations. Unfortunately, none of the mentioned above defects sharply points to a specific SM extensions, nor sug-

1.3. SOME THEORIES BEYOND THE STANDARD MODEL

gestes us which kind of experiments to use. Therefore during the last years, a wide range of theories has been elaborated, and many physics experiments all over the world are looking for experimental evidences.

A possible SM extension that would solve the hierarchy problem, is obtained introducing a new symmetry, called **supersymmetry** (in the following SUSY). Through the introduction of new supersymmetrical particles, the quadratic divergences in the Higgs mass parameter, will be cancelled in perturbation theory. The supersymmetric theory establishes that each SM particle has an identical *superpartner*, which differs only for the spin of $\pm\frac{1}{2}$. Therefore to each SM fermion corresponds a supersymmetric boson with spin=0, wiceversa to each SM boson corresponds a supersymmetric fermion. For example to the SM Higgs boson (with spin 0) will correspond the SUSY fermion higgsino (with spin= $\frac{1}{2}$); to the SM photon corresponds the SUSY photino ($s=\frac{1}{2}$) and to the SM electron ($s=\frac{1}{2}$) corresponds the selectron (spin=0). Conventionally, SUSY fermions, associated to SM bosons, have the suffix “-ino”, while SUSY bosons, associated to SM fermions, have the prefix “s-”. The supersymmetric particles can be considered as dark matter constituents because it is always possible formulate the existence of a lightest supersymmetric particle which should be light and permanent.

Although SUSY was considered for years as a front-runner of BSM theories, up to now there are no experimental evidences of the validity of this theory.

An ulterior example of theory beyond the SM is the **Grand Unified Theory** (GUT), in which the three gauge groups SU(3), SU(2) and U(1) corresponding to the SM interactions strong, weak and electromagnetic, are embedded in a grand unified gauge group. Therefore, at sufficiently high energies ($\sim 10^{16}$ GeV, called GUT scale), all the interactions would be described by one single coupling constant g_G . Two possible Lie groups wich could be the GUT symmetry group are SU(5) or SO(10). Historically, the first GUT was developed by Georgi and Glashow in 1974, using the SU(5) symmetry group.[7]

Following this idea, several models were developed in order to built the **Theory of Everything** (ToE), which would unify all the fundamental in-

1.3. SOME THEORIES BEYOND THE STANDARD MODEL

interactions of nature. The ToE, in fact, should provide the unification of the GUT force with gravity at the Planck energy ($\sim 10^{19}$ GeV). Unfortunately at the moment there are no experimental evidences of GUT or ToE.

CHAPTER 2

LHC and the ATLAS detector

2.1 The Large Hadron Collider

The Large Hadron Collider (LHC) is a circular proton-proton collider located at CERN nearby Geneva, Switzerland. Founded in the 1954, CERN holds the largest particle physics laboratory in the world, with 2500 employers who design and build particle accelerators ensuring their smooth operation. Some 12 000 visiting scientists from over 70 countries and with 105 different nationalities, come to CERN for their research. CERN laboratories are also involved in technology transfer and engineering, energy and computing researches.

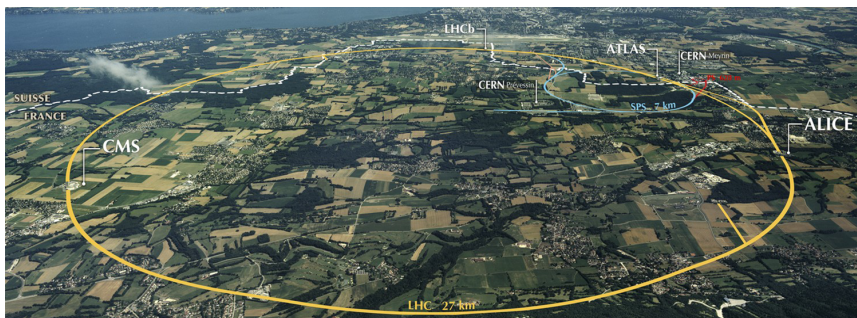


Figure 2.1: With a circumference tunnel of almost 27 km, the Large Hadron Collider lies up to 100-175 m beneath the French-Swiss border near Geneva.[14]

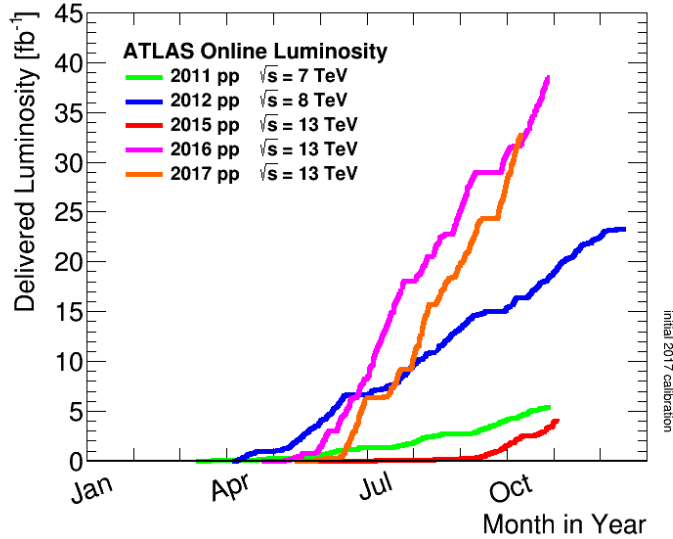


Figure 2.2: Cumulative luminosity versus day delivered to ATLAS during stable beams. All data-taking periods with the corresponding center of mass energy for proton-proton collisions are reported.[15]

The main accelerator located at CERN is LHC, which has been put into operation in 2008, and it is constituted by a circular ring of 26.7 km length lied at 100-175 m below the ground.

LHC is designed to accelerate in opposite directions hadron, protons or even heavy ions beams. In case of protons beams the technical specifications provide a *center of mass energy* of $\sqrt{s} = 14$ TeV and an instantaneous luminosity of $\mathcal{L} = 2 - 3 \times 10^{34} \text{ cm}^{-2} \text{ s}^{-1}$. During the so-called Run-2 data taking, which covers the period 2015 – 2018, the center of mass energy for proton-proton collisions is 13 TeV. Up to 9 October 2017 the instantaneous luminosity peak is $1.74 \times 10^{34} \text{ cm}^{-2} \text{ s}^{-1}$, and the integrated luminosity recorded is 68.7 fb^{-1} . [15] Fig. 2.2 show the center of mass energy and the integrated luminosity for every data taking periods.

LHC is composed by two rings of 4.2 km radius corresponding to two beamlines travelling in opposite directions and horizontally distant 194 mm. Each beam is constituted by bunches of $1.15 \cdot 10^{11}$ protons, separated by 25 ns (*bunch spacing*). [16] The number of bunches per beam is 2835. Conventionally the clockwise circulating beam is called beam 1, while the anticlockwise

2.1. THE LARGE HADRON COLLIDER

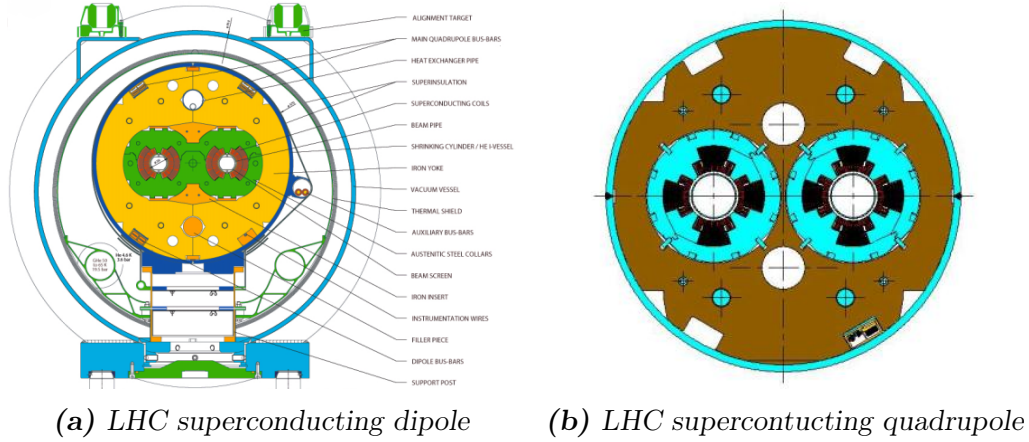


Figure 2.3: Schematic cross section view of LHC superconducting magnet: the picture 2.3a shows a dipole, while the 2.3b shows a quadrupole magnet

circulating one is beam 2.

To bend the beams in order to keep them in the right direction, 1232 superconducting *dipoles* of 15 m length are installed, while to keep the beams focused 392 superconducting *quadrupole* magnets are installed, see Fig. 2.3 for a schematic view of their cross sections. The LHC superconducting magnets take advantage of a technology based on Rutherford Cables (constituted by $6 \mu\text{m}$ thick filaments of Niobium-Titanium) dipped in *superfluid helium* at a temperature of 1.9 K, wrapped in coils which generate, with the passage of current, a magnetic field of almost 8.4 T.[17]

The LHC structure, see Fig. 2.4, is constituted of eight bending arcs separated by eight insertions. The middle of each insertion is called *insertion point* (IP), therefore there are eight insertion point IP1, IP2, etc. The part of the ring between two successive insertion points is called *sector*. The two beams cross at particular insertion points called *interaction points*, with an angle of $200 \mu\text{rad}$. The angle is small in order to reduce the number of unwanted proton-proton interactions occurred near the interaction point. For data-taking period Run-2 during 2017, the mean number of inelastic interactions per bunch-crossing is almost 32 (see Fig. 2.7 for the *pile-up* distribution).[15]

As shown in Fig. 2.4, at each of the four LHC interaction points, a physics experiment is located:

2.1. THE LARGE HADRON COLLIDER

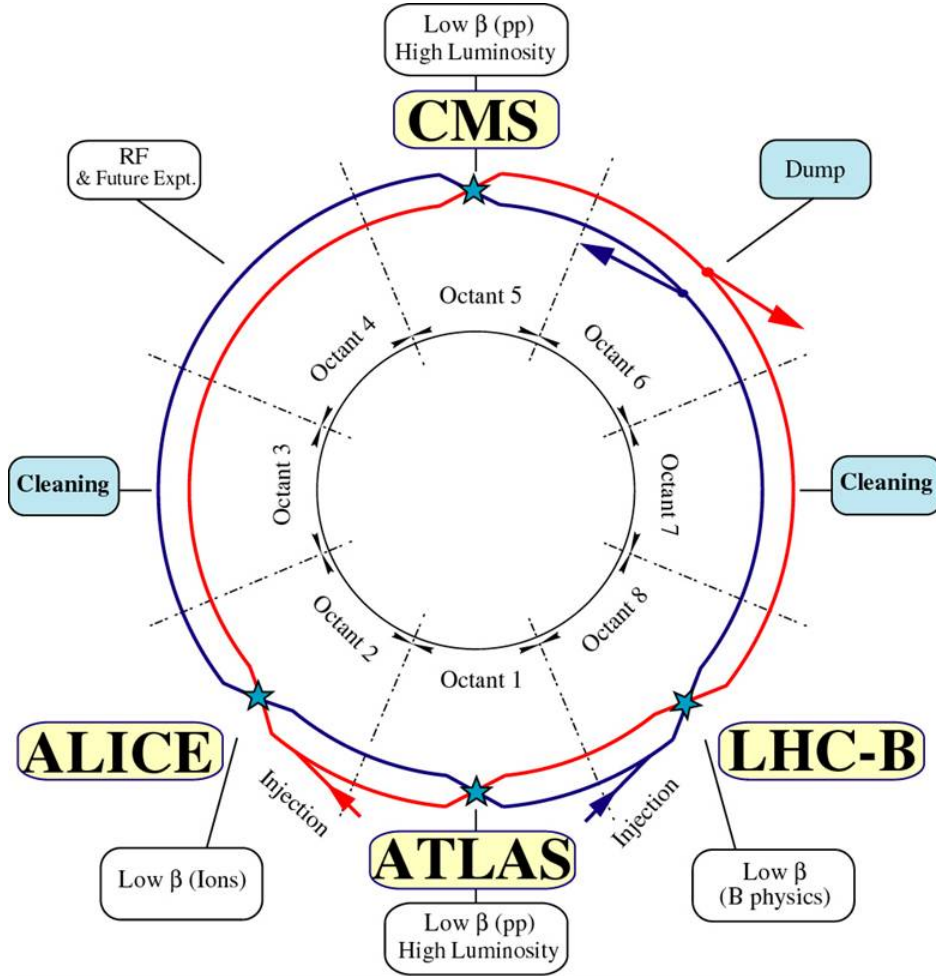


Figure 2.4: Schematic view of LHC ring showing the four interaction points with the corresponding experiments.

- ATLAS placed at the insertion Point-1. See Sec. 2.3 for details.[18]
- ALICE placed at the insertion Point-2.[19]
- CMS placed at the insertion Point-5.[20]
- LHCb placed at the insertion Point-8.[21]

The number of events produced per unit time ($\frac{dN_{ev}}{dt}$) is called *rate*, and it is proportional to LHC *instantaneous luminosity* (\mathcal{L}) and to the proton-

2.2. CERN ACCELERATOR COMPLEX

proton cross-section (σ):

$$\frac{dN_{ev}}{dt} = \sigma \cdot \mathcal{L} \quad (2.1)$$

The unit of measurement in the international system (SI) is $\text{s}^{-1}\text{cm}^{-2}$, in the non-SI units is $\text{b}^{-1} \text{s}^{-1}$.[\[6\]](#) The instantaneous luminosity \mathcal{L} doesn't depend on physics process, but only on beam properties:

$$\mathcal{L} = \frac{N^2 n_b f_{rev} \gamma_r}{4\pi \epsilon_n \beta^*} F \quad (2.2)$$

where N is the number of protons per bunch; n_b is the number of bunches per beam; f_{rev} is the revolution frequency, i.e. the frequency with which bunches interact; γ_r the relativistic factor. The denominator represents the cross-sectional area of overlap of the beams: ϵ_n is the normalized transverse emittance; β^* is the value of beta function at interaction point and F is the luminosity reduction factor caused by the crossing angle.[\[16\]](#) For the value of these parameters at LHC see Tab. [2.1](#).

The *integrated luminosity* (L_{int}) is defined as the amount of data collected in a time $L_{int} = \int \mathcal{L} dt$. It is very important because it is directly related to the number of observed events:

$$N_{ev} = \sigma \cdot L_{int} \quad (2.3)$$

The unit of measurement in SI is cm^{-2} , in the non-SI units is b^{-1} .

2.2 CERN accelerator complex

LHC is not the unique machine located at CERN. To reach the record energy of 6.5 TeV for each of the two proton beams, LHC requires a succession of machines that boosts the energy of particles before injecting the beam into the next machine. This chain of accelerators, most of which have their own experimental halls for experiments at lower energy, is called CERN accelerator complex, see [2.5](#).[\[22\]](#)

The protons source is a simple bottle of gas hydrogen in which an elec-

2.2. CERN ACCELERATOR COMPLEX

Parameter	Symbol	Unit	Value
Machine circumference	$2\pi R$	[m]	26658.883
Number of arc			8
Ring separation		[mm]	194
Number of insertion			8
Number of interaction point			4
Energy	E	[TeV]	7.0
Dipole field	B	[T]	8.4
Luminosity	\mathcal{L}	[$\text{cm}^{-2}\text{s}^{-1}$]	10^{34}
Injection energy	E_i	[GeV]	450
Number of bunches	n_b		2835
Bunch spacing	τ_b	[ns]	24.95
Particle per bunch	N		$1.05 \cdot 10^{11}$
Stored beam energy	E_s	[MJ]	334
Normalized transverse emittance	ϵ_n	[$\mu\text{m rad}$]	3.75
β -value at IP	β^*	[m]	0.5
rms beam radius at IP	σ^*	[μm]	16
γ transition	γ		53.7
Luminosity per bunch collision	L_b	[cm^{-2}]	$3.14 \cdot 10^{26}$
Crossing angle	ϕ	[μrad]	200
Revolution frequency	f_{rev}	[kHz]	11.1
Luminosity reduction factor	F	[rad]	0.9

Table 2.1: LHC performance parameters.

2.2. CERN ACCELERATOR COMPLEX

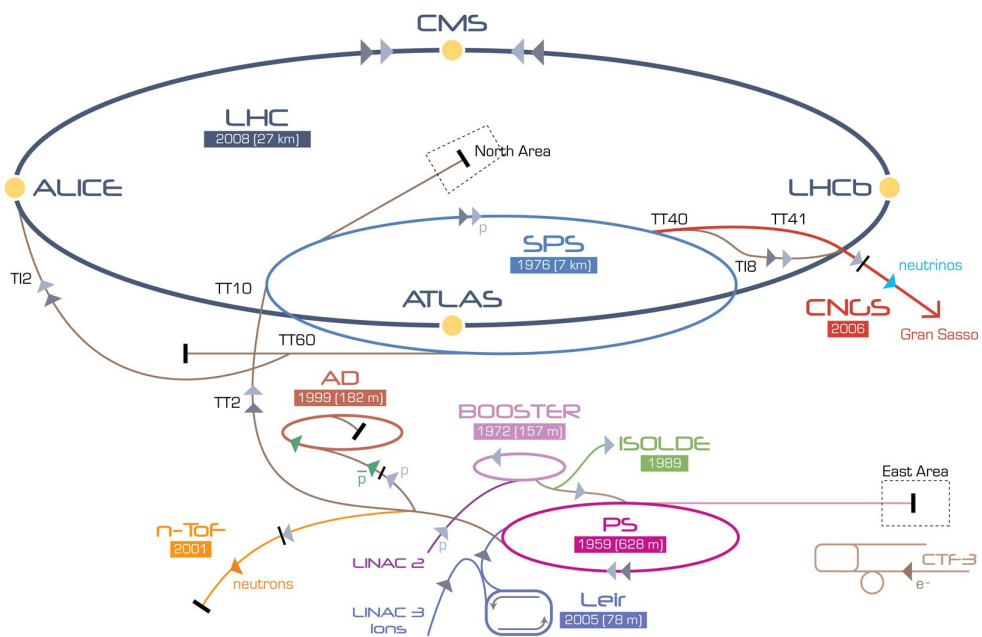


Figure 2.5: Schematics view of the entire CERN accelerator and detector complex. Length of circumference and start of physics data collisions are reported.

tric field is used to remove electrons from the atoms, and obtain protons. *LINAC2* is the first accelerator of the chain where protons are brought up to the energy of 50 MeV. Subsequently, they are injected in *Proton Synchrotron Booster* (PSB) which accelerates them up to the energy of 1.4 GeV.

Later, the beam is injected in *Proton Synchrotron*¹ (PS) which brings it up to 25 GeV of energy. PS is followed by *Super Proton Synchrotron*² (SPS) which accelerates the protons up to an energy of 450 GeV. Finally the protons are injected in LHC in two different pipes and they are brought up to 6.5 TeV during the Run-2.

Protons are not the only particles colliding in LHC, in fact lead nuclei are accelerated first by *LINAC3*, subsequently by *Low Energy Ion Ring* (LEIR) and then after the same chain of machines as the proton, they are injected in LHC.

Finally, we must say that the CERN accelerator complex includes also the *Antiproton Decelerator*, the *Online Isotope Mass Separator* (ISOLDE) facility. Moreover the accelerator complex feeds the *CERN Neutrinos to Gran Sasso* (CNGS) project and the *Compact Linear Collider* (CLIC) test area, as well as the *neutron time-of-flight facility* (nTOF).

2.3 The ATLAS detector

As a *general-purpose detector*, ATLAS does not focus on a single topic, but investigates a wide area of physics researches involving not only proton-proton collisions but also heavy ions collisions (in particular lead nuclei at 5.5 TeV). The ATLAS main physics researches[23] are:

Higgs boson The Higgs mechanism, theorized in 1960, explains how the elementary particles gain mass by the interaction with the *Higgs field*.

¹With 627 m of length and 100 dipoles, the Proton Synchrotron was the first synchrotron built at CERN in 1959.

²With a circumference of 7 km and 744 dipoles, the Super Proton Synchrotron is the second biggest CERN machine. It was inaugurated in 1976 and it was used for important scientific researches like the discoveries of W and Z in 1983.

2.3. THE ATLAS DETECTOR

The carrier particle Higgs boson was discovered in 2012 and the theoretical physicist Peter Higgs and François Englert received the Nobel Prize the next year.

Dark matter The matter of Universe is dominated by an unknown type of matter called dark matter. If the constituents of dark matter are new particles, ATLAS should discover them and solve the mystery of dark matter. It is possible that this new particle is the lightest particle postulated in theories of supersymmetry.[24]

Antimatter There is no intrinsic difference between particles and antiparticles³, this means that the laws of physics for particles and antiparticles are almost identical, therefore it is not explained why in the universe there is a big difference between the amount of matter and antimatter. In order to answer this question, we need to better understand that tiny part of the laws of physics that differ for matter and antimatter and, therefore, is important to study the differences in the decays of B-mesons and their antiparticle partners.

Extra dimension An indication for extra dimensions may be the extreme weakness of gravity compared with the other three fundamental forces. This weakness may be due to gravity's force field spreading into other dimensions. The ATLAS experiment may see evidence that extra dimensions exist via collision events in which a graviton particle disappears into other dimensions, in this case ATLAS should detect a large imbalance of energy in the event.

³In 1927 Dirac formulated an equation to describe free electrons with energy given by relativistic formula $E^2 - p^2c^2 = m^2c^4$, but it leads to the conclusion that for every positive-energy solution it is admitted a corresponding solution with negative energy. This meant that the electron should run away to increasingly negative states, radiating off an infinite amount of energy. To rescue his equation, Dirac postulated that the negative energy states are all filled by an infinite sea of electrons. *The absence of one electron in the sea, would be interpreted as a net positive charge and a net positive energy.* In 1931 Carl D. Anderson, with a cloud chamber, photographed a track left by cosmic ray particle which had positive charge and mass close to that of the electron: he discovered the positron, the electron antiparticle. [25]

2.3. THE ATLAS DETECTOR

New forces Many *grand unified theories* predict the existence of two carrier particles called Z prime (Z') and W prime (W') which lead to the theorization of new forces.

In order to investigate all these physics topics, the ATLAS detector must satisfy technical characteristics:

- Very good electromagnetic calorimetry for electron and photon identification, complemented by hadronic calorimetry for accurate jet and missing transverse energy measurement.
- Good charged-particle momentum resolution and good reconstruction efficiency in the innermost tracking detectors.
- Good muon identification and momentum resolution over a wide range of momenta, and the capacity to determine without ambiguity the charge of high p_t muons.
- Large acceptance in pseudorapidity⁴ with almost full azimuthal angle coverage.
- Highly efficient triggering on low transverse momentum objects with sufficient background rejection.

The Fig. 2.6 shows the structure of the ATLAS detector. In order to detect almost all types of particles produced in proton-proton collisions, ATLAS is cylindrically shaped and structured like an onion with different layers of concentric detectors. In this way ATLAS is nominally forward-backward symmetric with respect to the interaction point. The external dimensions are 44 m in length and 25 m in height, with an overall weight of 7000 tonnes.

The main components of the ATLAS detector are:

1. **Magnet system** for bending the charged-particle path.
2. **Inner Detector** which reconstructs the particle flight and determines primary and secondary vertex.

⁴See Sec. 2.3.1 for a mathematical definition.

2.3. THE ATLAS DETECTOR

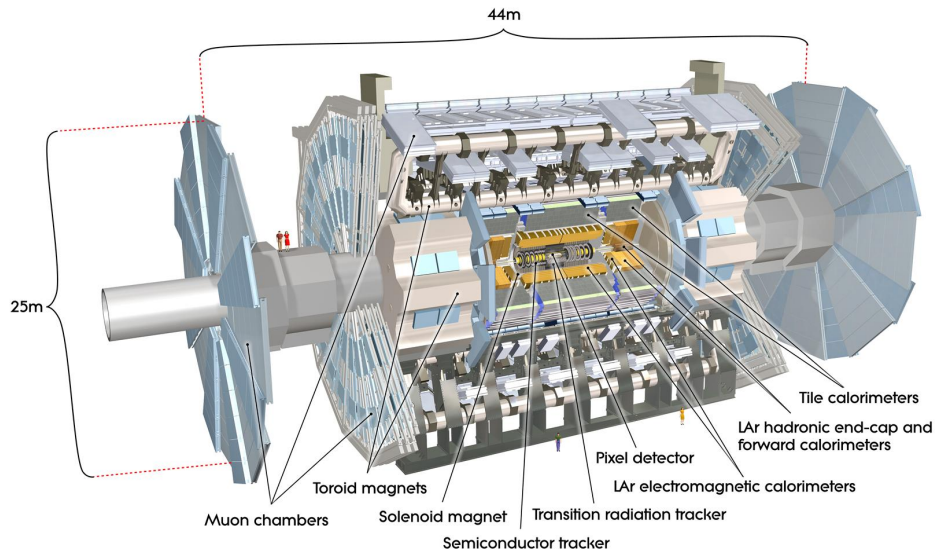


Figure 2.6: Schematic overview of the ATLAS detector and its subdetectors.

3. **Calorimeters** which measure electrons, photons and jets energy.
4. **Muon Spectrometer** for muon identification and momentum measurement.

The magnet configuration, see Sec. 2.3.2, is based on an inner superconducting solenoid around the inner detector cavity, and three large superconducting air-core toroids (one barrel and two End-Caps (EC) magnets). This air-core toroid system is able to generate a large field volume and strong bending power.

The Inner Detector (ID), see Sec. 2.3.3, is embedded in a magnetic field from a 2 T solenoidal. Momentum and vertex measurement are achieved with a combination of high-resolution pixel and strip detector in the inner part of the tracking volume.

Around the ID, electromagnetic and hadronic calorimeters are located. The *Liquid Argon (LAr) electromagnetic calorimeter* covers the pseudorapidity range $|\eta| < 3.2$. It is highly granular sampling and allows to reach ex-

2.3. THE ATLAS DETECTOR

cellent performance in terms of energy and position resolution. On the other hand, the hadronic calorimeter is constituted by a *scintillator-tile calorimeter* which covers the pseudorapidity region $|\eta| < 1.7$. The Tile calorimeter consists of one barrel cylinders and two smaller EC cylinders. Moreover in the EC region a *LAr hadronic End-Cap calorimeter* is installed to extend the η coverage up to $3.2 < |\eta| < 4.9$. See Sec. 2.3.4 for a detailed description.

The most external detector is the Muon Spectrometer (MS), see Sec. 2.3.5. It is immersed in a toroidal magnetic field, and it allows to keep track of muons which reach the last layer of ATLAS. The MS detector has an excellent muon momentum resolution, achieved using three stations of high-precision tracking chambers. Moreover the MS consists of fast trigger chambers with time resolution of almost 1-2 ns.[18] In addition to the main subdetectors, ATLAS consists of three smaller detectors installed at very high η region:

- **LUMinosity measurement using Cherenkov Integrating Detector (LUCID)** which is a relative luminosity detector,
- **Zero-Degree Calorimeter (ZDC)** which detects forward neutrons in heavy-ion collisions,
- **Absolute Luminosity For ATLAS (ALFA)**.

In particular, the LUCID detector, described in Sec. 2.3.6, is a Cherenkov light detector dedicated to detect inelastic proton-proton scattering in order both to measure the integrated luminosity and to provide online monitoring of the instantaneous luminosity and beam conditions. The ATLAS recorded luminosity has lower efficiency with respect the LHC delivered one, e.g. for the Run-2 data-taking the delivered luminosity is 74.6 fb^{-1} while the ATLAS recorded one is 68.7 fb^{-1} . This is due to the DAQ inefficiency and to the so called *warm start* of the detectors. In fact when the stable beam flag is raised, the tracking detectors need time to undergo a ramp of the high-voltage and, the pixel system to turn on the preamplifiers.[15] The online

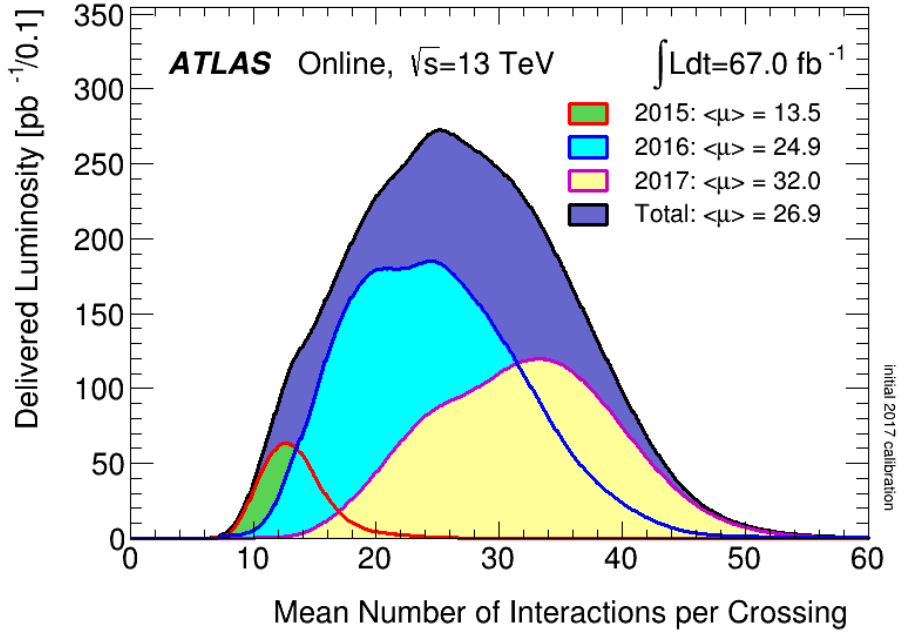


Figure 2.7: Luminosity-weighted distribution of the mean number of interactions per crossing for proton-proton collisions collected during Run-2 (up to 13 September 2017). The mean number of interactions per crossing μ corresponds to the mean of the poisson distribution of the number of interactions per crossing calculated for each bunch. It is calculated from the instantaneous luminosity per bunch L_{bunch} , the inelastic cross section σ_{inel} and the revolution frequency f_{rev} as $\mu = \frac{L_{bunch} \cdot \sigma_{inel}}{f_{rev}}$. [15]

luminosity measurement is used for the calculation of the number of inelastic interactions per bunch crossing (usually referred to as *pile-up*), see Fig. 2.7.

2.3.1 The coordinate system and kinematic variables

The coordinate system used in ATLAS is right-handed with origin in the nominal interaction point. [26] The z-axis is oriented along the beam pipe and the x-y plane is transverse to the beam direction (with the x-axis pointing towards the center of the LHC ring and the y-axis points vertically upward). Conventionally *side-A* refers to the ATLAS detector with positive z-axis, while *side-C* refers to the ATLAS detector with negative z-axis. Due to the ATLAS cylindrical symmetry, in the tranverse plane cylindrical coordinates

2.3. THE ATLAS DETECTOR

are used: the azimuthal angle ϕ is measured around the beam pipe, the polar angle θ is measured with respect to the beam pipe.[27]

Usually in particle physics, rather than use θ , it is used the **pseudorapidity** η , which is related to the angle of the particle with respect to the beam pipe as:

$$\eta = -\ln \left[\tan \left(\frac{\theta}{2} \right) \right] \quad (2.4)$$

In HEP experiments the pseudorapidity is used because it coincides with the *rapidity*.⁵ The advantage is that the particle production is constant as a function of rapidity and differences in rapidity are Lorentz invariant under boosts along the longitudinal axis. In the ATLAS detector the “forward” (“backward”) direction refers to regions close to the beam axis at high $|\eta|$, with positive (negative) z-direction.

Other useful physics quantities to describe the relativistic kinematics of a particle are:

- The **transverse momentum**, the **transverse energy** are defined in the x-y plane, i.e., in the transverse plane to the beam pipe. The transverse momentum is defined as $p_T = \sqrt{p_x^2 + p_y^2}$, while the transverse energy of a massive particle is defined as $E_T = \sqrt{m^2 + p_T^2}$.
- The missing transverse momentum, also called **transverse missing energy** (MET), is related to the energy expected (from the laws of energy conservation and momentum conservation) but not detected due to several effects: (i) the presence of weakly, or not, interacting particles; (ii) dead detector regions; (iii) particles not coming from the primary collision. In proton-proton high energy collisions MET is intensively used, because although the proton energy is known, the energy of inter-

⁵The rapidity is defined as:

$$y = \frac{1}{2} \ln \left(\frac{E + p_z}{E - p_z} \right)$$

where $p_z = |\vec{p}| \cdot \cos \theta$ and $E = \sqrt{m^2 + \vec{p}^2}$. For highly collimated particles $|\vec{p}| \gg m$, therefore

$$y \simeq \frac{1}{2} \ln \left(\frac{1 + \cos \theta}{1 - \cos \theta} \right) \simeq \eta$$

acting quarks and gluons is unknown. Since the transverse momentum of incident quarks and gluons is negligible ($p_T^i \simeq 0$), the total transverse momentum in the initial state is zero $\sum_i p_T^i \simeq 0$, therefore also the total transverse momentum in the final state has to be zero⁶. The imbalance in the total transverse momentum is the transverse missing energy.

- The 3-D angular separation of two particles is expressed in terms of ΔR which is defined in the η - ϕ space as:

$$\Delta R = \sqrt{(\Delta\eta)^2 + (\Delta\phi)^2} \quad (2.5)$$

- The **invariant mass** m_{inv} of two or more i-particles is defined as:

$$m_{inv} = \sqrt{\sum_i p_i^2} \quad (2.6)$$

where $p_i = (E_i, \vec{p}_i)$ is the four-momenta of the considered i-th particles.

- The **radiation length** X_0 is defined as the mean path length required to reduce the energy of an electron of a factor $\frac{1}{e}$. The radiation length depends on the atomic number of the material and on the mass of the incident particle. This physics quantity is important for electromagnetic calorimeter.
- The **nuclear interaction length** λ , similarly to X_0 , is defined as the mean path length required to reduce the energy of a hadronic charged particle of a factor $\frac{1}{e}$.

2.3.2 The magnet system

The ATLAS magnet system is particular important to measure the transverse momentum of produced charged particle, and it consist of:

⁶Effects like the initial state radiation of interacting quarks, the presence of dead detector regions have to be taken into account.

2.3. THE ATLAS DETECTOR

Property	Feature	Unit	CS	BT	ECT
Size	Inner diameter	m	2.46	9.4	1.65
	Outer diameter	m	2.56	20.1	10.7
	Axial length	m	5.8	25.3	5.0
	Number of coils	m	1	8	2 x 8
Mass	Conductor	tons	3.8	118	2 x 20.5
	Coil mass	tons	5.4	370	2 x 140
Coils	Turns per coil		1154	120	116
	Nominal current	kA	7.73	20.5	20.5
	Stored energy	GJ	0.04	1.08	2 x 0.25
	Field in the windings	T	2.6	3.9	4.1
	Field in the bore	T	0.9 - 2.0	0.2 - 2.5	0.2 - 3.5
Conductor	Number of strands		12	38 - 40	40
	Strand diameter	mm	1.22	1.3	1.3
	Temperature margin	K	2.7	1.9	1.9

Table 2.2: Magnet system main parameters.[28]

2.3. THE ATLAS DETECTOR

- A *Central Solenoid* (CS)[29]
- An air-core *Barrel Toroid* (BT)[30]
- Two air-core *End-Cap Toroids* (ECT)[31]

The main parameters characterizing all the elements of the ATLAS magnet system are summarized in Tab. 2.2.

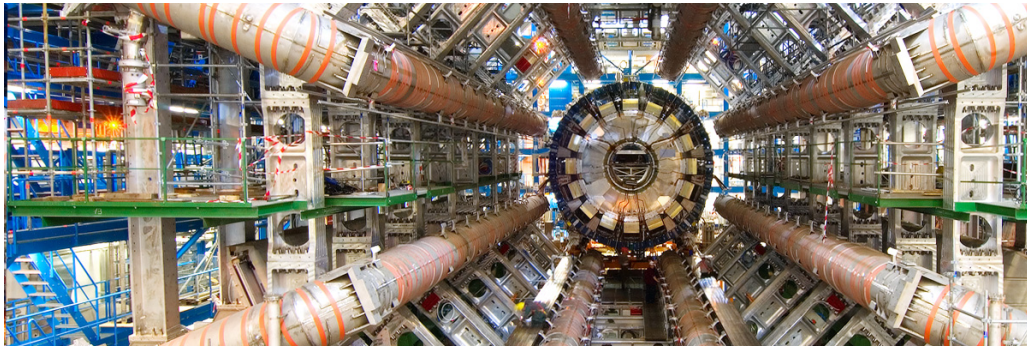
The **Central Solenoid**, see Fig. 2.8b, consists of a single layer coil of 5.3 m long and 5 tons heavy which axis coincides with the beam axis. The superconducting coil is wound with an Al stabilized NbTi conductor and operates at a nominal current of 7.73 kA, allowing a stored energy of 38 MJ.[32][28] With 1173 turns, it is designed to provide 2 T axial field pointing in the positive z-direction. Moreover, to achieve the desired calorimeter performance, the layout was optimized to keep the material thickness in front of the calorimeter as low as possible, in fact, the total solenoid (coil plus cryostat wall) thickness is $0.83 X_0$. This requires that the solenoid windings and LAr calorimeter share a common vacuum vessel.[33]

The **Barrel Toroid**, see Fig. 2.8a, is 25.3 m long, with an outer diameter of 20.1 m, and it consists of 8 superconducting coils with 120 turns. Each coil is 25 m long and 5 m large with a diameter of 1 m and operates at a temperature of 4.5 K. The barrel toroid operates at a nominal current of 20.5 kA providing a 4T axial field. The advantage of using a magnet toroid is that the magnetic field direction is almost perpendicular to the particle direction of flight. Moreover an air-core toroid can minimize the number of multiple scattering from particles cross through the detector.

The **End-Cap Toroid**, see Fig. 2.8c, consists of 8 superconducting coils with 116 turns, bolted and glued together into a rigid structure able to resist the Lorentz forces.[33][18]. The EC toroid generates the magnetic field requiring for optimizing the bending power in the EC regions of the muon spectrometer system.

The superconducting ATLAS magnet system takes advantages of the cryogenic and vacuum system. Regarding the *vacuum system* the insulat-

2.3. THE ATLAS DETECTOR



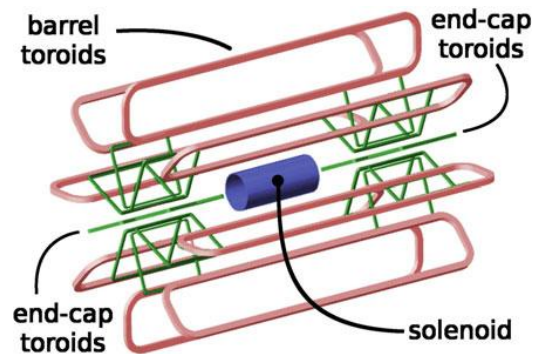
(a) Barrel magnet toroid



(b) Central magnet solenoid



(c) Lowering of the End-Cap magnet toroid



(d) Schematic view of magnet system

Figure 2.8: Overview of the different parts of the ATLAS Magnet System: Fig. 2.8a shows a picture of the barrel toroid, Fig. 2.8b of the central solenoid and Fig. 2.8c of the End-Cap toroid. To summarize, Fig. 2.8d is a digital picture representing the windings of the entire ATLAS magnet system.

2.3. THE ATLAS DETECTOR

ing of the barrel and EC toroids is achieved with diffusion pumps directly attached to the coils. The insulating of the central solenoid is installed inside the cryostat of the LAr barrel calorimeter, therefore the insulation vacuum is controlled by the LAr cryogenic system, not by the magnetic system.

The *cryogenic system* is very important for the functioning of the ATLAS superconducting magnets. Three different cryogenic fluids are used:

- Helium for cooling the superconducting magnets up to 4.5 K,
- Argon for the detector calorimetry,
- Nitrogen as an auxiliary fluid.

All the ATLAS coils take advantage of He circulating in Al cooling tubes connected to the cold mass. In particular, in the barrel toroid, each coil has its own cryostat, instead, in the EC toroid, due to the small dimension, one large cryostat per side is used.[18]

2.3.3 The Inner Detector

The Inner Detector is the innermost part of the ATLAS detector. It is designed to provide excellent momentum resolution and track reconstruction for charged particles with $p_T > 0.5$ GeV and $|\eta| < 2.5$. [34]

In particular the resolution of the momentum measurement is given by⁷:

$$\frac{\sigma_{p_T}}{p_T} = 0.05\% \cdot p_T \oplus 1\% \quad (2.7)$$

The ID is surrounded by the central solenoid, see Sec. 2.3.2, therefore it is immersed in a 2 T magnetic axial field.

As shown in Fig. 2.9, the ID consists of a barrel part constituted by cylindrical layers of sensors, and two EC parts where the sensors are arranged in disks. The ID is constituted by three distinct subdetectors:

1. *Pixel detector*

⁷The symbol \oplus means quadratic sum.

2.3. THE ATLAS DETECTOR

System	Position	Channels (10^6)	Area [m^2]	Resolution [μm]	η cover
Pixels	1 removable barrel	16	0.2	z=115 R ϕ =10	± 2.5
	2 barrel layers	80	1.4	z=115 R ϕ =10	± 1.7
	2 x 4 EC disks	43	0.7	R=77 R ϕ =12	1.7-2.5
SCT	4 barrel layers	3.2	34.4	z=580 R ϕ =17	± 1.4
	2 x 9 EC wheels	3.0	26.7	R=580 R ϕ =17	1.4-2.5
TRT	axial barrel straw	0.1		170 (per straw)	± 0.7
	radial EC straw	0.35		1370 (per straw)	0.7-2.5

Table 2.3: Main parameters of the ATLAS Inner Detector. The resolutions mentioned are mean values (the real resolution in each detector depends on $|\eta|$).

2. *SemiConductor Tracker* (SCT)

3. *Transition Radiation Tracker* (TRT).

The main technical parameters of these three subdetectors are summarized in Tab. 2.3.

The *Silicon Pixel Detector* is designed to provide a very high-granularity and high-precision track measures as close as possible to the interaction point. As solid-state ionization chamber, when each pixel is crossed by charged particles there is the production of an electron-hole pair which generates an electric signal. The Silicon Pixel Detector is able to provide excellent transverse impact parameter and vertex resolution also in presence of high track density. Moreover, it is designed to find short-lived particles such as b-quarks and τ -leptons, therefore the Silicon Pixel Detector provides excellent b-tagging and b-triggering abilities.[35]

In the barrel region the system consists of four coaxial cylindrical pixel layers with a radius of almost 3 cm, 5 cm, 9 cm and 12 cm, as shown in

2.3. THE ATLAS DETECTOR

Fig. 2.9, while in each of the EC regions there are three pixel disks. The innermost layer of Pixel Detector is called **Insertable B-Layer** (IBL).[36] The IBL is the closest detector to the interaction point and it was installed during the first Long Shutdown LS1 in 2013-2014.

Totally the Silicon Pixel Detector is composed by more than 2000 modular units and almost 80 million readout channels. Each pixel is 256 μm thick with a surface $R\phi \times z$ of $50 \times 400 \mu\text{m}^2$, and the spatial resolution is 14 μm on $R\phi$ -coordinate and 115 μm on z -coordinate.[37]

The *SemiConductor Tracker*, like the Pixel Detector is a silicon-based detector, but the SCT takes advantage of microstrips technology which allows to provide a bidimensional position measurement.

With a length of 5.4 m and more than 6 million of readout channels, the SCT is the intermediate detector of ATLAS ID and it consists of a barrel and two EC parts. The barrel part covers a radial range of ~ 30 -51 mm and it consists of four concentric cylinder layers each of which contains 2112 silicon modules. Instead each EC part contains 1976 silicon modules arranged in nine disks.

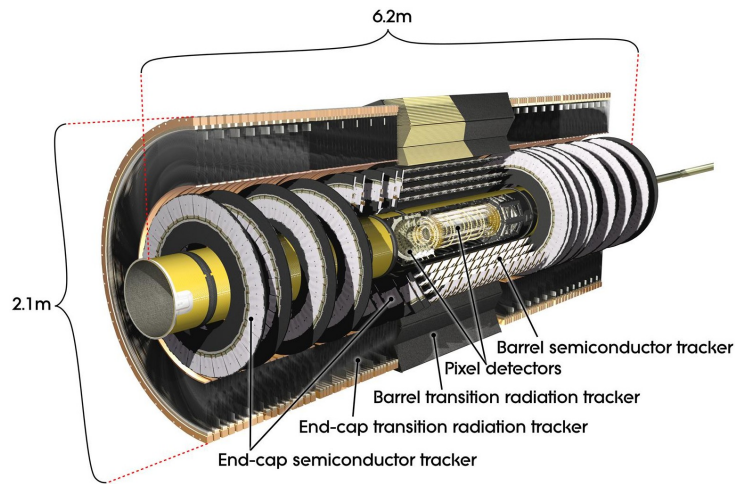
The SCT detector provides a spatial resolution per layer of 17 μm on $R\phi$ -direction (because the strips are 80 μm apart) and 580 μm on z -direction.[37]

The *Transition Radiation Tracker*, see Fig. 2.9, is constituted by a barrel and two end-cap components. It is the outermost detector of the ATLAS ID and it is designed to provide position measurement in $R\phi$ -coordinate.[38]

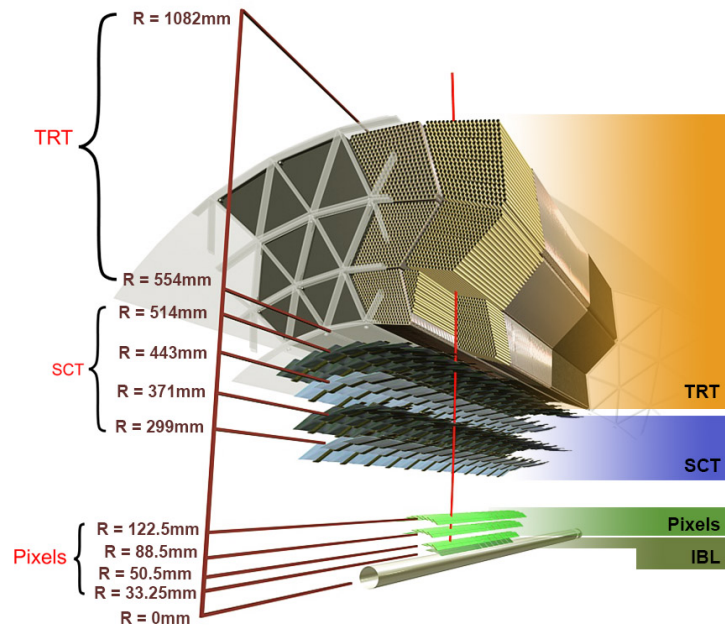
The basic TRT detector elements are proportional drift tubes (called straw tubes or simply straws) with a diameter of 4 mm which act as a cathode. In the center of each straw tube, as anode, a 0.03 mm diameter gold-plated tungsten wire is placed.[37] Each straw is filled with a gas mixture of 70% Xe + 27% CO₂ + 3% O₂ which guarantees the following requirements:

- efficient transition radiation photon absorption,
- good electrical stability for straw,

2.3. THE ATLAS DETECTOR



(a) View of the ATLAS Inner Detector



(b) Cut-away view of Inner Detector

Figure 2.9: The ATLAS Inner Detector showing the different sub-detectors.

- compatibility with the detector and gas system materials,
- not inflammability,
- dissociation products with minimum aggressive properties.

In order to allow the TRT detector to provide electron-pion discrimination, the transition radiation emitted by particles that flew through the detector is measured. For this reason the straw tubes are interleaved with radiators: polypropylene foils for the EC regions, polypropylene fibres for the barrel region.⁸ In the barrel region the TRT covers the radial range ~ 55 - 108 cm and it is composed by more than 50 000 straws, all 144 cm long and parallel to the beam pipe. On the other hand, in each EC region there are 18 wheels containing 250 000 straws which are 39 cm long and perpendicular to the beam pipe. The TRT geometry guarantees that particles that pass through the detector cross 35-40 straw tubes, with a spatial resolution of $170 \mu\text{m}$ per straw. The total number of readout channels is approximately 350 000.[37]

2.3.4 The Calorimeters

The ATLAS calorimeter, see Fig. 2.10, provides high precise measurement of energy and position of photons and electrons which pass through the detector, moreover it provides an accurate measurement of jets and transverse missing energy. The calorimeters operation is based on stopping (*absorbing*) most of the particles coming from the interaction point, forcing them to deposit all their energy within the detector by the production of cascade of particles, called *shower*.⁹[40] Therefore the calorimeters need to have good containment for electromagnetic and hadronic showers limiting *punch-through* to the muon system which surrounds the calorimeters.

The ATLAS calorimeters are *sampling detectors* constituted by layers of “passive” (or absorbing) high-density material interleaved with layers of “active” material which detects the energy deposits. Totally the calorimeters cover the pseudorapidity range $|\eta| < 4.9$. In particular over the η region matched to the ID, the electromagnetic calorimeter has fine granularity in order to measure electrons and photons, instead in the rest of the pseudorapid-

⁸Typically the transition radiation energy depositions is almost 9 keV for photon and 2 keV for minimum-ionizing particles like pions.[39]

⁹Different type of particles produce different types of showers: electrons and photons produce electromagnetic showers, while hadrons produce hadronic shower.

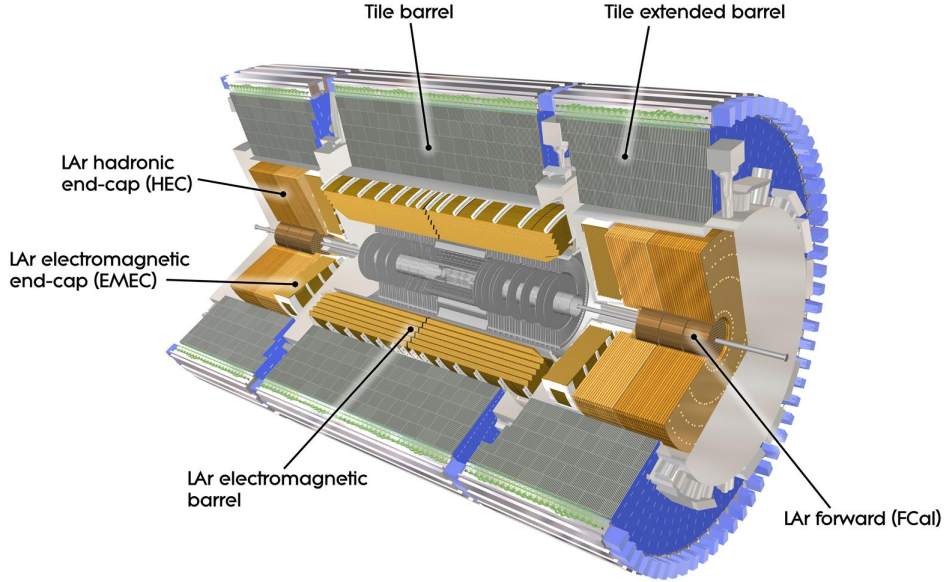


Figure 2.10: Schematic cut-away view of the ATLAS calorimeter detectors.

ity range a lower granularity is sufficient for jet reconstruction and transverse missing energy measurements.[33]

The calorimeter energy resolution improves with the energy of the particles which pass through the detector, and it can be parameterized by¹⁰:

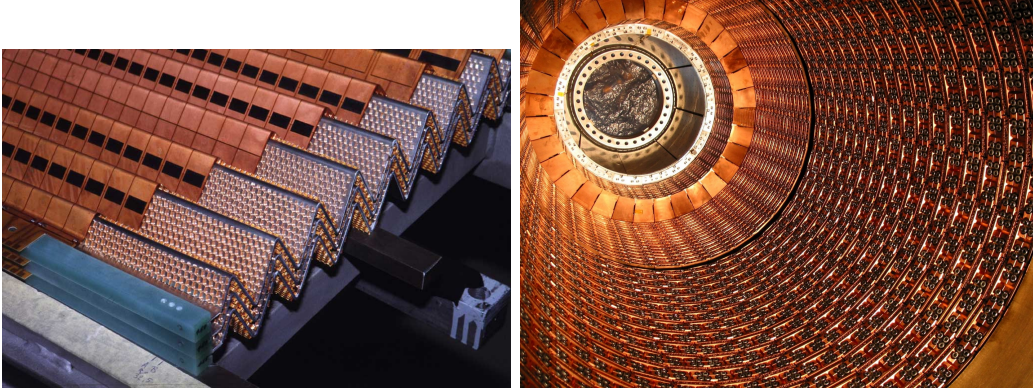
$$\frac{\sigma_E}{E} = \frac{a}{\sqrt{E}} \oplus \frac{b}{E} \oplus c \quad (2.8)$$

where a , b , c parameters are η -dependent and are related to different calorimeter properties: a depends by calorimeter material and by its sampling (e.g for electromagnetic calorimeter $a = \frac{10\%}{\sqrt{E}}$); b is related to the electronic noise and it is negligible at very high energies; c is a constant term which depends by the calorimeter inhomogeneities.

The ATLAS electromagnetic calorimeter

The electromagnetic calorimeter (ECal) identifies a wide energy range of electrons and photons, and also measures their energy and the total MET.[18]

¹⁰The symbol \oplus means quadratic sum.



(a) ECal accordion structure

(b) ATLAS EMEC calorimeter

Figure 2.11: The ATLAS electromagnetic calorimeter: the Fig. 2.11a shows a detail of the structure showing the accordion-shape; the Fig. 2.11b shows a view of the ATLAS End-Cap electromagnetic LAr calorimeter placed inside the End-Cap cryostat.

The ECal consists of different components: a barrel and two end-cap ones. The barrel part which is $24 X_0$ thick, covers the region $|\eta| < 1.475$ and shares the vacuum vessel and the cryostat with the central solenoid. Instead each end-cap part (EMEC), with a thickness of $26 X_0$, is housed in its own cryostat and extends the coverage of the ECal up to the region $1.375 < |\eta| < 3.2$. [41]

As shown in Fig. 2.11, ECal is a sampling calorimeter with accordion geometry and it is constituted by lead plates as passive material and LAr as scintillating material. The thickness of the lead plates is optimized as a function of η in order to obtain high granularity in the region devoted to precision physics measurements. The lead was chosen due to its short radiation length ($X_0 = 0.561$ cm), while the advantage of LAr is the radiation-hardness and stability response during the time. Moreover the accordion geometry provides complete ϕ symmetry with fine granularity.

The electromagnetic barrel calorimeter is constituted by two identical half-barrels separated at $z = 0$ by a gap of 4 mm, and it consists of three layers. The first one is $4.3 X_0$ thick and it has a granularity 0.03×0.1 in $\Delta\eta \times \Delta\phi$; the second layer is $16 X_0$ thick and it is segmented in square towers with a higher granularity 0.025×0.025 ; finally the third layer has a granularity of 0.05×0.025 .

Calorimeters	Energy resolution
EM Barrel	$\frac{\sigma_E}{E} = \frac{10\%}{\sqrt{E}} \oplus 0.7\%$
EM End-Cap	$\frac{\sigma_E}{E} = \frac{10\%}{\sqrt{E}} \oplus 0.7\%$
HEC	$\frac{\sigma_E}{E} = \frac{50\%}{\sqrt{E}} \oplus 3\%$
FCAL	$\frac{\sigma_E}{E} = \frac{100\%}{\sqrt{E}} \oplus 10\%$
TileCal	$\frac{\sigma_E}{E} = \frac{50\%}{\sqrt{E}} \oplus 3\%$

Table 2.4: Design energy resolutions of the ATLAS calorimeter subdetectors. The detectors EM barrel, EM end-cap, HEC and FCAL are Liquid-Argon Calorimeters.[42]

Each electromagnetic EC calorimeter consists of two coaxial wheels: an outer wheel of radius ~ 210 cm which covers the region $1.375 < |\eta| < 2.5$, and an inner wheel of radius ~ 33 cm which covers the region $2.5 < |\eta| < 3.2$.

The Tab. 2.4 reports the design energy resolutions for all electromagnetic calorimeter subdetectors.

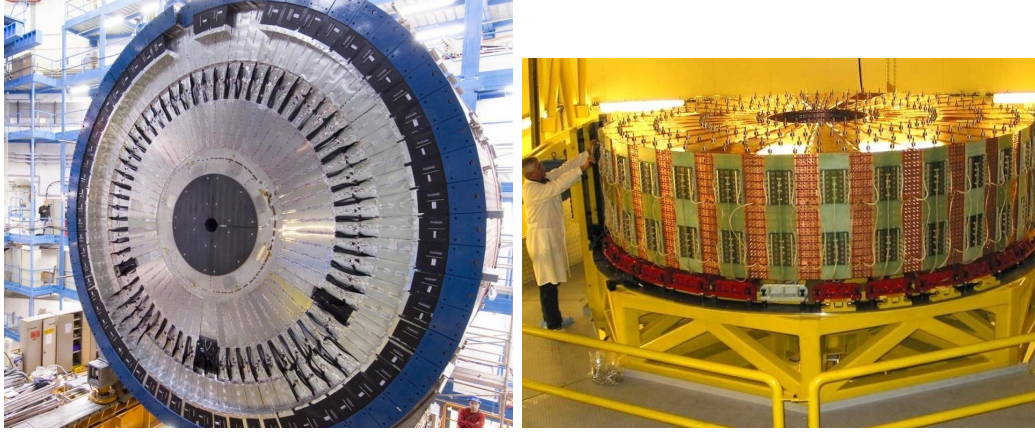
The ATLAS hadronic calorimeter

The Hadronic Calorimeter (HCal) main purposes are jet identification measuring its energy and direction, and measurement of missing transverse energy E_T^{miss} . [43] For this reason HCal has a full coverage in η and, as shown in Fig. 2.10, it is divided in three distinct components:[33]

- The *Tile Calorimeter* (TileCal)
- The *Hadronic liquid argon End-Cap* (HEC)
- The *Hadronic liquid argon Forward Calorimeter* (FCal)

See Tab. 2.4 for the energy resolution of all the hadronic calorimeter subdetectors.

The *Tile Calorimeter*, placed in the barrel region outside the electromagnetic calorimeter, has cylindrical shape with an inner radius of 2.28 m and an outer radius of 4.25 m. The TileCal covers, in the barrel region,



(a) ATLAS Tile calorimeter

(b) ATLAS HEC calorimeter

Figure 2.12: The ATLAS hadronic calorimeter. Fig. 2.12a shows a view of the Tile calorimeter constituted by triangular-shape modules arranged in ring. Fig. 2.12b shows the assembly of LAr hadronic End-Cap calorimeter.

the pseudorapidity range $|\eta| < 1.0$ and in the extended barrel region the range $0.8 < |\eta| < 1.7$. [44] It is a sampling calorimeter which alternates steel plates used as “passive” material, with scintillating tiles used as “active” material. The two side of the scintillating tiles are readout through two separate photomultiplier tubers.

As shown in Fig. 2.12, the TileCal is divided in 64 module in ϕ -direction and it is segmented in depth in three layers with a thickness of 1.5, 4.1, 1.8 λ for the barrel and 1.5, 2.6, 3.3 λ for the extended barrel. The granularity $\Delta\eta \times \Delta\phi$ is 0.1×0.1 for the first and second layer, and 0.2×0.1 for the third layer.

The *Hadronic liquid argon End-Cap* covers the pseudorapidity region $1.5 < |\eta| < 3.2$ and consists of two independent wheels per end-cap which share the cryostat with the EMEC calorimeter. As shown in Fig. 2.12, each of the four HEC wheels is divided in two layers in depth, and it consists by 32 wedge-shaped modules. Moreover, each wheel is formed interleaving copper plates (used as absorbing material) to 8.5 mm of LAr gaps (used as active medium). The copper plates have an inner radius of 0.48 m and an outer radius of 2 m, moreover the copper plates used in the innermost wheel are

25 mm thick, while that ones used in the outermost wheel are 50 mm thick.

The *Hadronic liquid argon Forward Calorimeter* is integrated into the end-cap cryostat and covers the very high η region corresponding to $3.1 < |\eta| < 4.9$. The FCal is the only ATLAS detector which covers this η region and it is useful to reduce the radiation background in the muon spectrometer. In each EC part, the FCal consists of three longitudinal layers in which LAr is the active medium. The innermost layer is optimized for electromagnetic measurements in fact it consists of copper as absorbing material. The other two layers are optimized for hadronic interaction, therefore the tungsten is used as absorber.

2.3.5 The Muon Spectrometer

The Muon Spectrometer (MS) is the outermost detector of ATLAS and it is designed to detect charged particles exit from the calorimeters.¹¹ The peculiarity of MS consists to provide an accurate and independent measurement of muons momentum reconstructing their tracks (in the pseudorapidity range $|\eta| < 2.7$), and also to provide a muon independent trigger (in the range $|\eta| < 2.4$). Therefore the MS is able to detect stand-alone muons and this feature allows to study BSM theories, see Chap. 4, in which neutral long-lived particle decaying into muons beyond the ID.

To obtain an accurate momentum measurement independently from the ID, the MS takes advantage of the magnetic field produced by the air-core barrel toroid and the two air-core end-cap toroids, see Sec. 2.3.2. The barrel toroid covers the pseudorapidity range $|\eta| < 1.4$, the end-cap toroids cover the range $1.6 < |\eta| < 2.7$, while the range $1.4 < |\eta| < 1.6$, usually called *transition region*, is covered by a combination of barrel and end-cap fields.[45]

As shown in Fig. 2.14, the Muon Spectrometer has cylindrical shape with length of 46 m and diameter of 22 m, and it consists of eight octants, each divided in ϕ -direction in *large sector* and *small sector*. In the barrel region

¹¹Since the radiation length X_0 is proportional to the mass square, the X_0 of muons is bigger than the electrons one, therefore in the calorimeters muons lose energy by ionization processes but they don't generate shower, hence muons can reach MS detector.

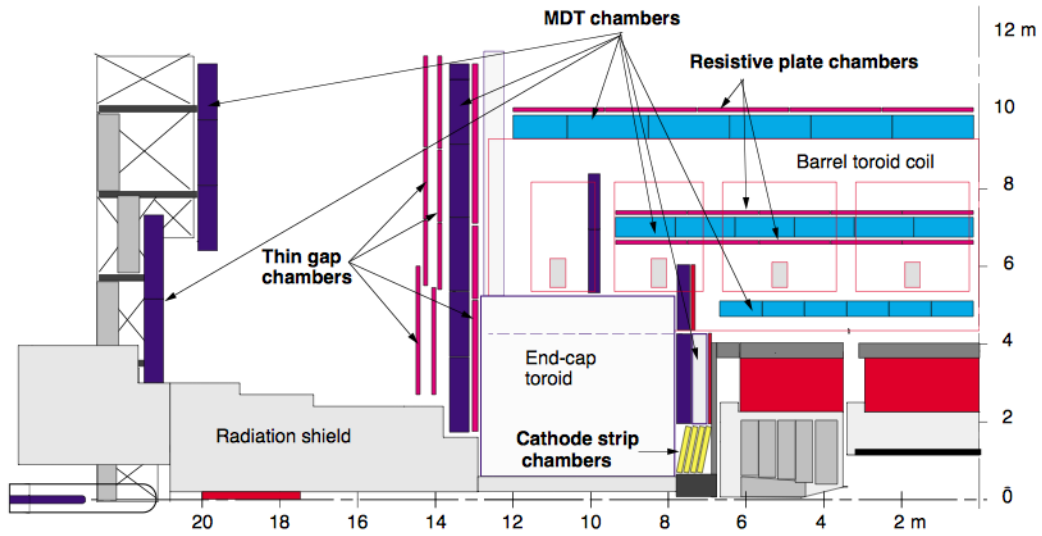


Figure 2.13: Digital representation of Muon Spectrometer cutview. The x and y axis show the detector dimension starting from the interaction point.

the MS subdetectors are arranged in three cylindrical layers around the beam pipe, called *stations* placed between the barrel toroid coils at a radial distance of 5 m, 7.5 m and 10 m, see Fig. 2.13. On the other hand in each end-cap and transition region the chambers are located before and after the end-cap toroid and are installed in three **wheels** orthogonal to the beam pipe at a distance of 7.4 m, 14 m and 21.5 m from the interaction point, see Fig. 2.13. The structure of the inner end-cap wheels will be detailed described in Chap. 3.

The subdetectors of the Muon Spectrometer are divided in **tracking chambers** as:

- *Monitor Drift Tubes* (MDT)
- *Cathode Strip Chambers* (CSC)

and **trigger chambers** as:

- *Resistive Plate Chambers* (RPC)
- *Thin Gap Chambers* (TGC)

2.3. THE ATLAS DETECTOR

The **Monitor Drift Tubes** chambers provide the *precision coordinate* measurement, i.e. the measurement on the bending plane η , allowing the muon momentum measurement in the pseudorapidity range $|\eta| < 2.7$.[\[46\]](#)

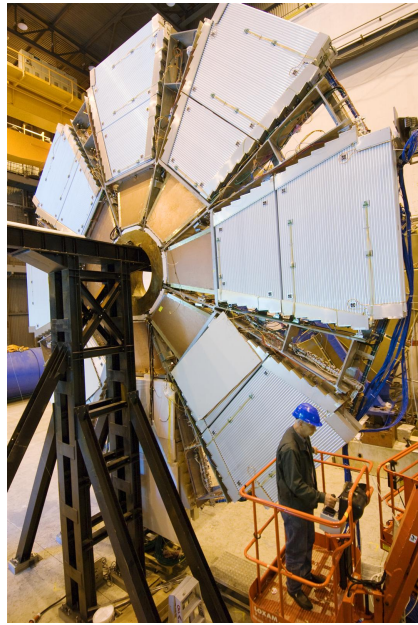
The basic detector element is a cylindrical aluminum drift tube with a diameter of 30 mm, filled with a gas mixture Ar:CO₂ (93:7) at an absolute pressure of 3 bar. The electrons resulting from the ionization process are collected by the central gold-plated tungsten-rhenium wire, with a diameter of 50 μm at voltage of 3080 V. Each drift tube has an average resolution of 80 μm and to improve the detector resolution, each MDT chamber is constituted by 2 layers of groups of tubes called *multilayers*.[\[47\]](#) In the barrel region, each inner station multilayer consists of 4 layers of drift tubes, while each middle and outer station multilayer consists of 3 layers of drift tubes. In each end-cap region, MDT detectors are arranged in three stations. The inner EC station is located at 7.4 m along the z-direction (in the so-called Small Wheel), while the middle and outer ones, respectively at 14 m and 21.5 m. Fig. [2.14](#) shows a picture of an MDT end-cap station.

The **Cathode Strip Chambers** cover the region $2 < |\eta| < 2.7$ and provide precision coordinate measurements with a resolution of 60 μm . Due to their good time resolutions (~ 7 ns), small electron drift time, high granularity and high rate capability the CSC are installed in a pseudorapidity region with an high particle rate (~ 1150 Hz/cm²).

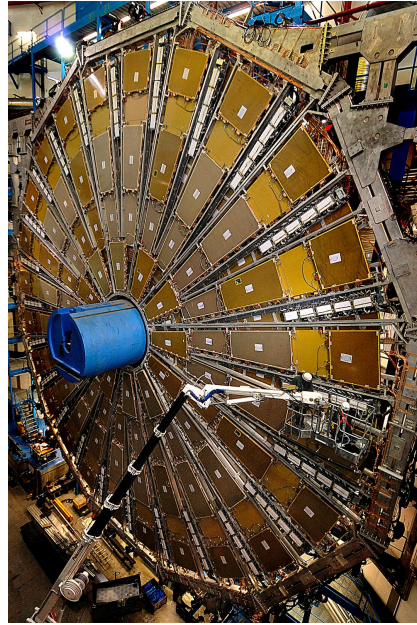
As shown in Fig. [2.13](#) and [2.14](#), in each ATLAS end-cap region there are two CSC disks, each made up of eight CSC chambers. Each chamber is constituted by four CSC planes in order to obtain independent η and ϕ position measurements per track. The CSC detector are multiwire proportional chambers filled with a gas mixture of Ar(30%) CO₂(50%) CF₄(20%). The anode wires are oriented in radial direction while the cathode are segmented: one with the readout strips perpendicular to the wires (in order to provide the precision coordinate measurement on η -direction) and the other with the readout strips parallel to the wires (in order to provide transverse coordinate measurement on ϕ -direction).[\[48\]](#)

The **Resistive Plate Chamber** are installed in the barrel region in three

2.3. THE ATLAS DETECTOR



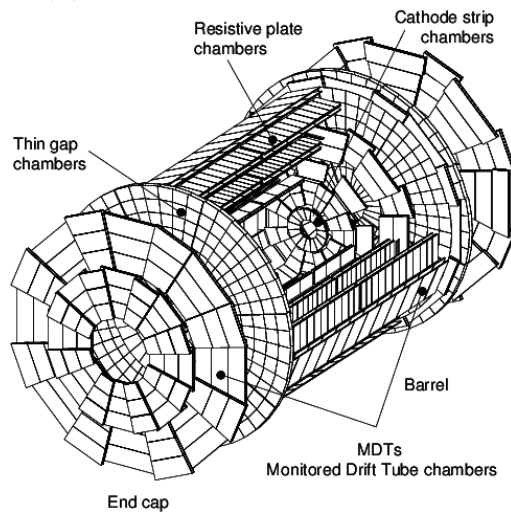
(a) ATLAS CSC detector



(b) ATLAS TGC detector



(c) ATLAS MDT detector



(d) 3D view of muon spectrometer

Figure 2.14: The ATLAS Muon Spectrometer subdetectors: Fig 2.14a, Fig 2.14b, Fig 2.14c show respectively the detectors End-Cap CSC, End-Cap TGC and End-Cap MDT, while Fig 2.14d is a three dimensional sketch of the entire muon spectrometer.[47]

2.3. THE ATLAS DETECTOR

concentric cylindrical station around the beam pipe, covering the pseudorapidity range $|\eta| < 1.05$ and they provide position measurements in η and ϕ coordinates with a spatial resolution of ~ 1 cm.[49] Due to its excellent time resolution the RPC chambers are used as trigger detectors providing bunch-crossing identification. In particular, the digital time resolution is about $\frac{25 \text{ ns}}{8} \frac{1}{\sqrt{12}} \sim 0.9$ ns due to the RPC clock frequency (which is eight times the bunch crossing clock frequency) and to the trigger window (which is 25 ns). Moreover the time fluctuation of the avalanche signal scale proportionally with the gas volume thickness, and for the ATLAS RPC this corresponds to a time resolution of almost 1.2 ns. However, several effects have to be taken into account (like electronic delays, signal delay along the strips), therefore the time resolution for the on-line time alignment is 4.2 ns, while after the off-line calibration it is ~ 2 ns.[50][51]

The RPC are gaseous detectors constituted by two resistive Bakelite plates separated by a 2 mm gap filled with a gas mixture of $\text{C}_2\text{H}_2\text{F}_4$: C_4HO (97:3) in which there is an electric field of 4.9 kV/mm. When a particle passes through the electric field, the ionization electrons are multiplied into avalanches and the signal is collected at the anode and readout by metal strips.

The **Thin Gap Chambers**, see Fig. 2.14, cover the pseudorapidity region $1 < |\eta| < 2.4$. They are multi-wire proportional chamber with good time resolution (~ 15 ns) and provide bunch-crossing identification. The detector is filled with a gas mixture of CO_2 (55%) n-pentane (3%) operating in saturation mode in order to obtain small sensitivity to mechanical deformations and nearly Gaussian pulses with small Landau tails. Although triggering is the main purpose, TGC provide position measurements both in η and ϕ coordinates. In each end-cap region the TGC detectors are installed in two wheels: the outer wheel (or big wheel) consists of 3 stations of doublets and triplets of TGC layers, while the inner wheel (or Small Wheel) consists of doublets of TGC layers.

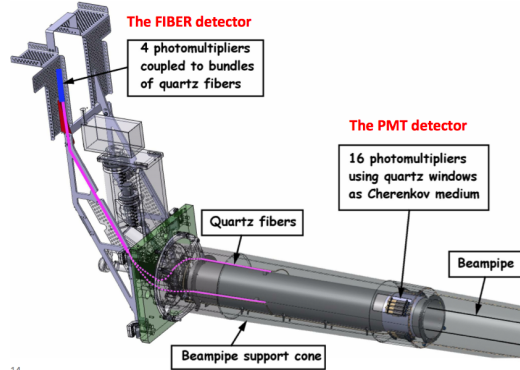


Figure 2.15: Schematic image of one of the two LUCID detectors which surround the beam pipe. The position of the photomultipliers and quartz fibers are displayed.[53]

2.3.6 LUCID

LUCID is a relative luminosity detector, and it is the only ATLAS sub-detector primarily dedicated to monitor the online luminosity and to measure the integrated luminosity.[52] On each of the ATLAS end-cap regions, LUCID consists of two detectors placed around the beam pipe at a distance of ± 17 m from the interaction point.

Each of the two LUCID detectors consists of 16 photomultipliers (PMTs) and 4 quartz fiber bundles. When a particle cross the PMTs quartz window, the Cherenkov light is produced and detected by the PMTs itself. Cerenkov light is produced in the quartz fiber as well, and readout by PMTs protected by a shielding two meters away.[53][54] To increase the detector lifetime, in a given time are used only a subset of PMTs, while the others are available as spares. As readout electronics to digitilize the PMTs signals, VME boards are used.

2.3.7 The Trigger System

As said in Sec. 2.1, during the Run-2 the LHC bunch spacing is 25 ns, which leads to a crossing rate of 40 MHz. Moreover at the Run-2 instantaneous luminosity of $\mathcal{L} \simeq 10^{34} \text{ cm}^{-2} \text{ s}^{-1}$ the mean number of interactions per bunch-crossing is almost 32, therefore the number of interaction per second

2.3. THE ATLAS DETECTOR

is $\sim 10^9$. Due to the very high number of interactions occurred it is impossible to store all events. Therefore the trigger is fundamental for the ATLAS experiment, because it is responsible for deciding whether or not to keep a given collision event for later study.[55][56]

As shown in the flow chart of Fig. 2.16, the event selection provided by the Trigger and Data Acquisition system (TDAQ) consists of three levels:[33]

- *Level-1* (L1) which is based on a dedicated hardware,
- *Level-2* (L2) which is a software trigger based both on L1 and on a fraction of data from precision detectors,
- *Event Filter* (EF) which is a software trigger and the last TDAQ level.

Moreover the two software trigger levels L2 and EF collectively constitute the **High Level Trigger** (HLT).

The **L1 trigger** makes use of analog sums of calorimeter and muon trigger chambers signals. In particular, the L1 selection takes advantage of custom-made electronics based on the two variables: the muon transverse momentum (provided by RPC and TGC chambers) and the transverse energy of objects like photons, jets, hadrons (provided by ECal and HCal). As shown in Fig. 2.16 in the meantime that L1 trigger makes a decision on the current event, usually defined as *latency*, the informations of all the subdetectors are stored in *pipeline memories*. The latency of L1 is 2.5 μ s and this value includes the transit times of signals between detectors and trigger system and the time required for sending the trigger accepts to the detector readout electronics.

For all the accepted events, which correspond at a rate of 100 kHz in the Run-2, the L1 trigger defines one or more *Region of Interest* (RoI). A RoI is a specific detector region defined by η and ϕ coordinates, in which the selection process has identified interesting features, e.g a particle which passes a transverse momentum threshold. Moreover for all the events accepted by L1 trigger, the informations coming from all subdetectors are pre-processed and stored in *Readout Buffers* (ROBs), see Fig. 2.16.

The two **HLT triggers** use the full granularity and precision data both

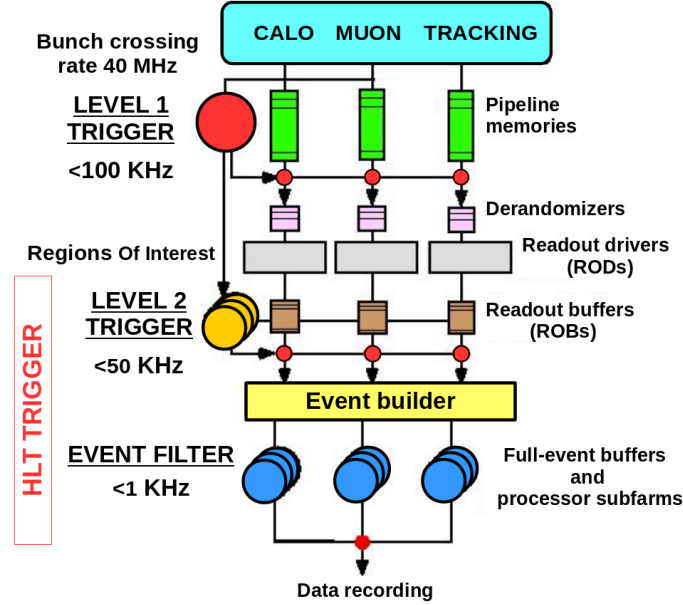


Figure 2.16: Flow chart of the ATLAS three level triggers.[56]

of calorimeters and muon chambers, and also they use data provided by the inner detector to improve the trigger selection obtaining an accept rate of 1 kHz within a processing time of about 200 ms.

In particular, the **L2 trigger** uses data provided by all the subdetectors for one or more RoI identified by L1 trigger, moreover it uses data stored in ROBs.

The **EF trigger**, which is the final event selection, uses all data provided from the ATLAS subdetectors, including offline reconstruction informations like track reconstruction, vertex finding etc. . . In addition to the selection, the EF trigger classifies the selected events according to a specific set of event *stream*.

Regarding the ATLAS Muon Spectrometer, see Sec. 2.3.5, the trigger system consists of RPC and TGC chambers, respectively covering the pseudorapidity regions $|\eta| < 1$ and $1 < |\eta| < 2.4$. They provide L1 trigger informations with a RoI spatial resolution $\Delta\eta \times \Delta\phi$ of 0.2×0.2 for the barrel region, and 0.1×0.1 for the end-cap one. The L1 trigger is provided using **coincidence windows** based on p_T thresholds:

- low p_T threshold ($6 \text{ GeV} \leq p_T \leq 20 \text{ GeV}$): in the barrel region are required at least 3 coincidences in the inner and middle RPC stations, while in the end-cap region are required at least 3 coincidences in the middle and outer big wheel TGC stations.
- high p_T threshold ($p_T \geq 20 \text{ GeV}$): in the barrel region are required at least 3 coincidences in the inner and middle RPC stations and 1 coincidence in the outer RPC station, while in the end-cap region are required at least 3 coincidences in the middle and outer big wheel TGC stations and 2 coincidences in the inner big wheel TGC station.

Finally, for the muon momentum reconstruction at HLT, the precision chamber informations are used.

2.4 The Phase-I ATLAS Upgrade

During the next data taking Run-3, scheduled for 2021 – 2023 as shown in Fig. 2.17, LHC will reach the center of mass energy of $\sqrt{s} = 14 \text{ TeV}$ with an instantaneous luminosity of $2 - 3 \times 10^{34} \text{ cm}^{-2}\text{s}^{-1}$. In order to consolidate and improve the physics capabilities of the detector, the ATLAS Collaboration planned an upgrade program during the next LHC long shutdown LS2: the **Phase-I Upgrade**.^[57] LS2 is the second LHC long shutdown: it will take place on 2019 – 2020 and it is finalized to the integration of Linac4 into the injector complex, and to the upgrade of the LHC collimation system. In the same period, will take place the ATLAS Phase-I upgrade, which is primarily finalized to the upgrade of the TDAQ system in order to obtain, also in presence of high luminosity conditions, an acceptable trigger rate keeping the current p_T thresholds. To achieve this aim the Phase-I upgrade will involve different ATLAS subdetectors with the following projects:

- The *Phase-I hardware track finder* (FTK) that will provide fast tracking informations as input to the HLT, using a copy of data from ID to perform its fast reconstruction;^[58]

- The *New Small Wheels* (NSW) which plans to replace the existing Small Wheels in the end-cap region of the Muon Spectrometer with the NSW.[59]
- The *ATLAS Forward Proton* (AFP) detector will provide measurements of the momentum and emission angle of very forward protons, allowing measurement of processes where one or both protons remain intact. Such processes are associated with elastic and diffractive scattering.[60]
- The *LAr Phase-I upgrade* is aimed to improve the Level-I calorimeter trigger. It will allow finer granularity data from the LAr Calorimeter in order to improve electron, photon, tau and jet selection.[61]
- The *Phase-I TDAQ upgrades* are focused primarily on the Level-I calorimeter triggers. More sophisticated algorithms will be implemented for electron, photons and jets reconstruction.[62]

In Chap. 3 is detailed described the **New Small Wheel project**. The current *Small Wheels*, located in the inner layer of the forward muon spectrometer, will be replaced by new tracking and triggering detectors. This upgrade will allow both to improve the tracking performance and to reduce the trigger rate including the NSW in the Level-1 trigger.

The installation of the New Small Wheel is particularly important for searches of processes beyond the Standard Model, in fact, it will be included in the Level-0 trigger system of the Phase-II upgrade in 2024 – 2027.[63] This Phase-II upgrade plans to improve both trigger and reconstruction efficiencies of the ATLAS detector for exotic models. In fact, these models usually predict the existence of long lived particles, which signature is characterized by displaced vertices non pointing back to the interaction points, and by particles in the final states with very small angles. Currently ATLAS is not designed for these searches, but the Phase-II will enable a wide range of precision measurements and searches within or beyond the Standard Model.

2.4. THE PHASE-I ATLAS UPGRADE

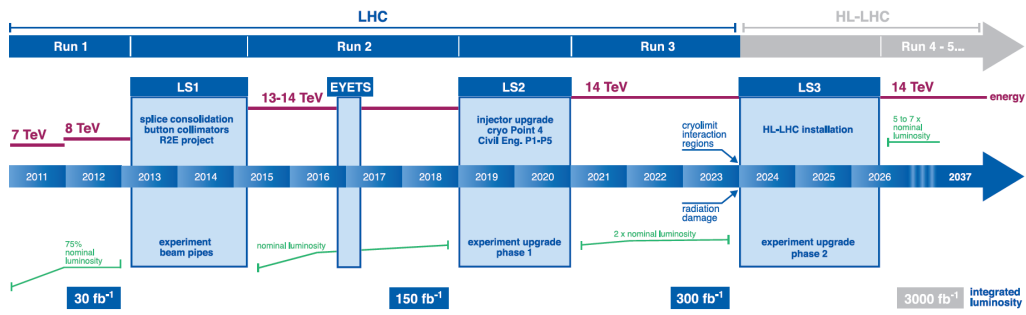


Figure 2.17: Picture showing the LHC long term operation schedule. The data taking runs with the related expected integrated luminosity, and the long shutdown periods are reported.

CHAPTER 3

The Atlas New Small Wheels

3.1 Motivation of the Small Wheel Upgrade

During the next data taking Run-3 (2021 – 2023), LHC will reach the center of mass energy $\sqrt{s} = 14$ TeV with an instantaneous luminosity of $2 - 3 \times 10^{34} \text{cm}^{-2}\text{s}^{-1}$. In this conditions, the number of inelastic interactions per bunch-crossing (pile-up) will be almost 70, and the number of tracks and background level will increase proportionally to the luminosity, especially in the forward regions. In particular, for the innermost end-cap region of the ATLAS muon spectrometer, so-called Small Wheel (SW), the expected rate at $\mathcal{L} = 3 \times 10^{34} \text{cm}^{-2} \text{s}^{-1}$ is $\sim 15 \text{kHz/cm}^2$.[\[64\]](#)[\[65\]](#)

The two ATLAS Small Wheels are located between the end-cap calorimeter and the end-cap toroid, and cover the pseudorapidity region $1.3 \leq |\eta| \leq 2.7$. Each Small Wheel, see [Fig. 3.1](#), is 10 m high and consists of a combination of MDT, TGC and CSC detectors. They are not designed to operate at instantaneous luminosity higher than the nominal one. An extrapolation from the observed rates in dedicated test beams to high instantaneous luminosity indicates a degradation of SW tracking performance, both in terms of efficiency and resolution, due to the dead time from background hits, see [Fig. 3.2](#).[\[59\]](#)

Moreover, currently the SW is only devoted to the precision physics mea-

3.1. MOTIVATION OF THE SMALL WHEEL UPGRADE



Figure 3.1: Picture showing the lowering of the ATLAS Small Wheel. On the front side are visible the 8 MDT chambers placed on a ring structure, while in the inner part of the ring the 8 TGC chambers are partially visible. Moreover 8 CSC chambers are installed in the Small Wheel but not visible.

surements, and the L1 muon trigger in the end-cap region is based on the TGC chambers of the middle muon station, so-called Big Wheel (BW), located after the end-cap toroid magnet. The result is that a significant part of the end-cap muon trigger rate is background. In fact, as shown in Fig. 3.3, low energy particles (mainly protons) generated in the material located between the SW and the BW, hit the BW TGC chambers at an angle similar to that of real high p_T muons producing *fake triggers*. As a consequence, the rate of the L1 muon trigger in the end-cap is eight to nine times higher than that in the barrel region, and most of the triggered objects are not reconstructible offline (see Fig. 3.4). Therefore, in presence of higher luminosity, the *L1 muon trigger rate* will exceed the available bandwidth (~ 20 kHz).

Certainly, a rate reduction can be obtained increasing the p_T threshold, but this would produce a loss of efficiency for physics events.[66] Therefore, in order to solve both reconstruction and trigger issues, the Small Wheels will be replaced with the New Small Wheels (NSW), and the installation will be performed during the ATLAS Phase-I upgrade in 2019 – 2020. The NSW[59], as will be described in Sec. 3.2, is a set of precision tracking and trigger detectors able to work at high rates. Due to the excellent real-time spatial and time resolution, the NSW will allow to reduce the L1 fake muon trigger rate in the end-cap region.

3.1. MOTIVATION OF THE SMALL WHEEL UPGRADE

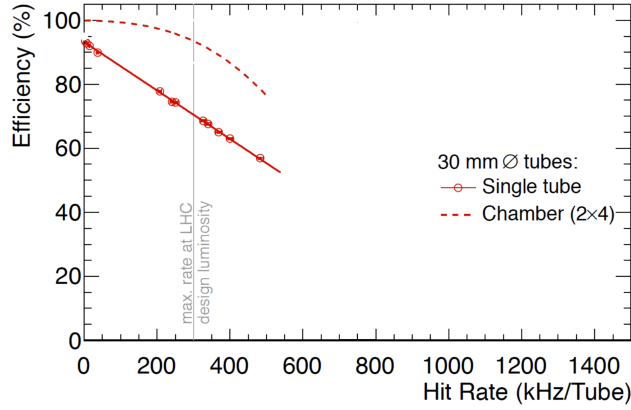


Figure 3.2: Efficiency of single MDT tube (solid line), and of a 2×4 MDT chamber (dashed line), as a function of the hit rate. The tracking efficiency decreases with increasing hit rate.[59]

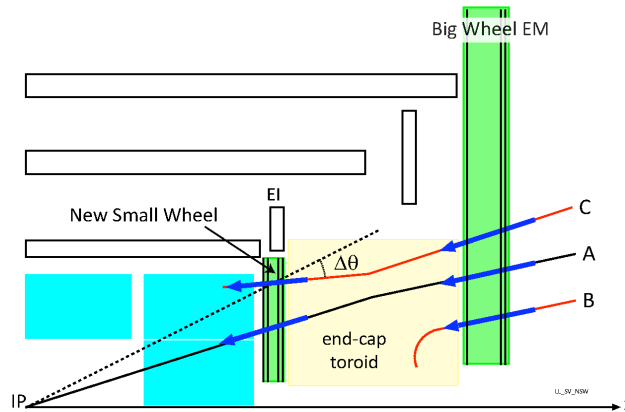


Figure 3.3: Schematic drawing of the ATLAS detector showing three examples of events with muon triggered by the Big Wheel. As it may be seen, only track A points towards to the interaction point, while the other two events correspond to fake triggers. With the NSW will be possible to distinguish the acceptable muons using the NSW trigger chambers.[59]

3.1. MOTIVATION OF THE SMALL WHEEL UPGRADE

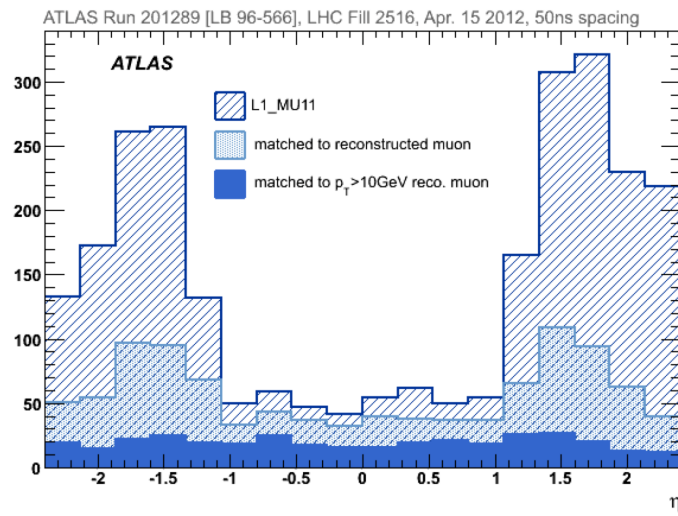


Figure 3.4: The η distribution of candidates selected by the ATLAS L1 trigger as muons with at least 10 GeV. The data are collected during the Run-2 and the following trigger rates are displayed: (i) L1 muon signal (oblique dashed distribution), (ii) L1 muon signal matched to an offline well reconstructed muon (dotted distribution), (iii) L1 muon signal matched to an offline well reconstructed muon of $p_T > 10$ GeV (solid blue distribution). As shown, the rate in the endcap region ($|\eta| > 1$) is dominated by fake triggers.[67][59]

3.2 The ATLAS New Small Wheel

Each New Small Wheel is 10 m high, with an inclination from the vertical plane of $\sim 0.708^\circ$. Moreover, it covers the pseudorapidity region $1.3 \leq |\eta| \leq 2.7$, with an active area of about 1280 m² and 2 M electronic channels. The NSW take advantage of two detection technologies: the *small strip Thin Gas Chambers* (sTGC), and the *Micro-MEsh Gaseous Structure* (MicroMegas, MM) detectors. Although sTGC are primarily dedicated to trigger, while MicroMegas to tracking, in order to obtain a redundant detector system, both detectors are used for trigger and precision tracking measurements.

As shown in Fig. 3.5, each NSW consists of 16 **sectors**: 8 large sectors alternating with 8 small ones, numbered consecutively starting from the large sector at $\phi = 0$ rad and positive x -coordinate. Each sector consists of a combination of four trapezoidal-shape **quadruplets** detector, arranged (in the z -coordinate) in the order sTGC–MM–MM–sTGC, with a central skeleton (placed between the two MM detectors) so-called *spacer frame*¹, for a total thickness of 360 mm. Since each of the MM and sTGC quadruplets consists of 4 active layers, a particle passing through the NSW², will produce 16 hits.

Radially, each sTGC is segmented into three modules while MicroMegas into two: SM1–SM2 for small sectors, and LM1–LM2 for the large ones. The construction of the 4 MicroMegas quadruplet types is distributed over several countries: France (LM1), Russia and Greece (LM2), Italy (SM1) and Germany (SM2). For each MicroMegas type, 34 quadruplets will be constructed in the period 2017 – 2019, following a strict procedure necessary to achieve the NSW requirements like the 15% p_T resolution for 1 TeV muons, and the segment online resolution of 1 mrad.

¹The spacer frame consist of a 50 mm thick, rigid aluminum structure used to fix the NSW sectors. As detailed reported in [59], it is designed to avoid deformations.

²Considering the position of the NSW, a particle coming from the proton-proton interaction point, will pass through the MicroMegas detector with an inclination between 8° and 32° with respect to the detector plane.

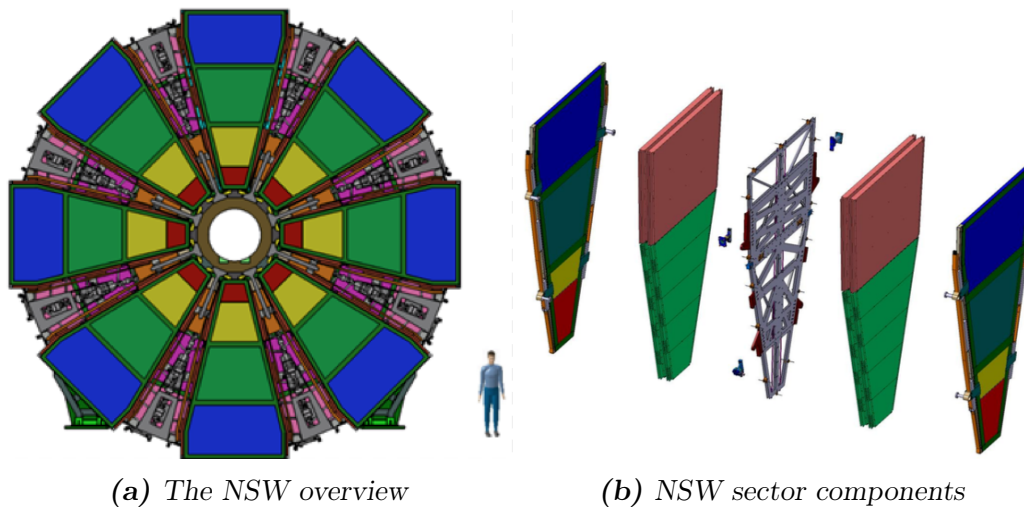


Figure 3.5: The New Small Wheel: Fig. 3.5a is a schematic picture of each end-cap wheel showing the large and small sectors. On the other hand, the Fig. 3.5b is an exploded view of a single NSW sector.

3.3 The MicroMegas detectors

The first micro-structure gas chambers is the **Micro-Strip Gas Chamber** (MSGC). Invented in 1988, it consists of a set of tiny parallel metal strips laid on a thin resistive support, alternatively connected as anodes and cathodes. Due to the small distance between anode and cathode ($\sim 100 \mu\text{m}$), the fast collection of positive ions reduces space charge build-up, and provides a greatly increased rate capability. However, the fragile electrode structure can be easily destroyed by discharges induced by heavily ionizing particles.[68]

The necessity of improving reliability and radiation hardness, leads to the construction of MicroMegas detector, invented in 1996 by Giomataris and Charpak[69]. In the *original configuration*, the Micromegas detector is a thin parallel-plate avalanche counter, and consists of a drift region of $\sim 3 \text{ mm}$ thickness, a thin metal grid (so-called micromesh or simply “mesh”) at $\sim 100 \mu\text{m}$ distance from the readout electrode plane (gold-coated copper strips of $5 \mu\text{m}$ thick and $200 \mu\text{m}$ pitch, printed on an insulator board), creating a narrow multiplication gap.

3.3. THE MICROMEGAS DETECTORS

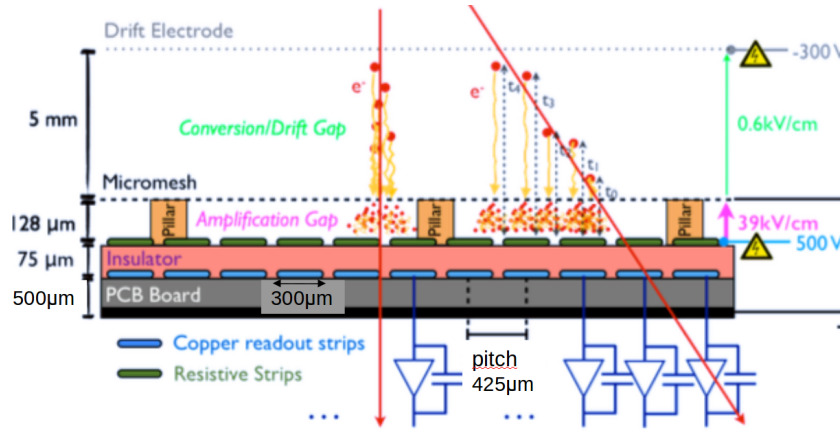


Figure 3.6: Sketch showing how a charged particle is detected using a resistive Micromegas: a muon cross through the detector ionizes the gas mixture and the electrons produced drift to the mesh causing avalanches. Finally the charge is collected by readout strips placed under the anode strips.[70]

The electric field in the drift region is about 1 kV/cm and it is obtained applying an electric potential difference between the drift electrode plane and the micromesh (both at negative high voltage HV), while in the amplification region the electric field is about 50 kV/cm, and it is obtained grounding the anode strips. Finally, the gas mixture used is Ar:CH₄ (90:10) at atmospheric pressure.

As shown in Fig. 3.6³, when a charged particle passes through the drift region, electrons from the primary ionization are produced.⁴ The primary electrons drift through the holes of the mesh into the narrow multiplication gap, where they are amplified and the resulting charge is collected by the anode strips. On the contrary, the positive ions drift backwards to the mesh. Due to the small amplification gap the electrons produce a narrow avalanche, giving excellent spatial resolution.[68][71] Moreover, the detector efficiency is about 80% and, due to the very short distance between mesh and anode strips, the positive ions are fast evacuated resulting in low dead time (\sim

³Actually the drawing refers to the New Small Wheel SM1 resistive MicroMegs detector. Except few technical differences, the operating principle of the NSW Micromegas is the same of the original one.

⁴See Appendix I for the interaction of charged particles with the matter.

3.3. THE MICROMEAS DETECTORS

100 ns). Although these advantages, the original MicroMegas detector is vulnerable to sparking, which occur when the total number of electrons in the avalanche reaches a few 10^7 .

For this reason, the **NSW MicroMegas detectors** have a spark protection system: a layer of *resistive strips* (resistivity of a about 10-20 M Ω /cm) on top of a thin insulator (75 μm) directly above the readout strips (see Fig. 3.6). In this way, the readout electrode is not directly exposed to the charge. On the contrary, it is induced on the resistive strips which are capacitively coupled to the readout strips. Although using a continuous resistive layer is simpler from the construction point of view, and effective in sparks protecting, the NSW MicroMegas takes advantage of resistive strips to avoid charge spreading on a large area.

As shown in Fig. 3.6, a single NSW MicroMegas detector consists of a drift region with an electric field of ~ 0.6 kV/cm, created by a cathode drift plane (-300 V), at 5 mm distance from a mesh, which has a pitch of 80 μm and a wire of 30 μm diameter. The amplification region instead, is 128 μm high with an electric field of 40 kV/cm. Since the electric field in the amplification region is much stronger than that in the drift region, the mesh is transparent to more than 95% of the electrons. [59]

Beside the introduction of resistive strips, there are other important differences between the NSW MicroMegas detector and the original one:

- the presence of a *floating mesh*,
- a new HV scheme.

The mesh is considered “floating” because it is not glued on the pillars but only laid on them. When the voltage is applied to the resistive strips, the electrostatic force between mesh and resistive strips ensures good contact between mesh and pillars, creating an amplification gap with homogeneous height. The main advantage of using a floating mesh is that in case of operating problems, the mesh can be easily removed without destroying the detector.

3.3. THE MICROME GAS DETECTORS

Parameter	Value
Space resolution in η -coordinate	$\sim 100 \mu\text{m}$
Space resolution in ϕ -coordinate	$\sim 2 - 3 \mu\text{m}$
Track separation	$\sim 0.4 \text{ mm}$
Rate capability	$\sim 0.4 \text{ mm}$
Efficiency	$> 98\%$

Table 3.1: NSW MicroMegas performance parameters. They are necessary to achieve the 15% p_T resolution for 1 TeV muons, and the segment online resolution of 1 mrad.

Regarding the HV scheme, instead to apply negative HV on the mesh keeping the resistive strips at ground potential (as in the original MicroMegas), positive HV ($\sim 500 \text{ V}$) is applied to the resistive strips while the mesh is connected to ground. In this way the spark-induced current can be evacuated very quickly to ground through the mesh without modifying the mesh electric potential, moreover, the electric field lines results to be better focused between the mesh and the resistive strips, see Fig. 3.7.[59]

Besides these, other performance features are necessary to achieve the NSW requirements on p_T resolution and online segments accuracy (see Sec. 3.2). A summary of all the NSW MicroMegas performance parameters is reported in Tab. 3.1.

In order to full explain the operating of the NSW MicroMegas, it is important to describe the electric and magnetic field within the detector and the clustering algorithm used. Considering the NSW position and orientation in the ATLAS experiment, the electric field in the MicroMegas detector is along the z -direction. On the contrary, the magnetic field (mainly due to the EC toroid magnet) has different orientations with a sizeble component orthogonal to the electric field. Therefore, electrons from ionization processes drift with a Lorentz angle⁵, and may spread across several strips. From simulations, it is verified that the NSW MicroMegas detectors will be exposed

⁵See Appendix I for more details.

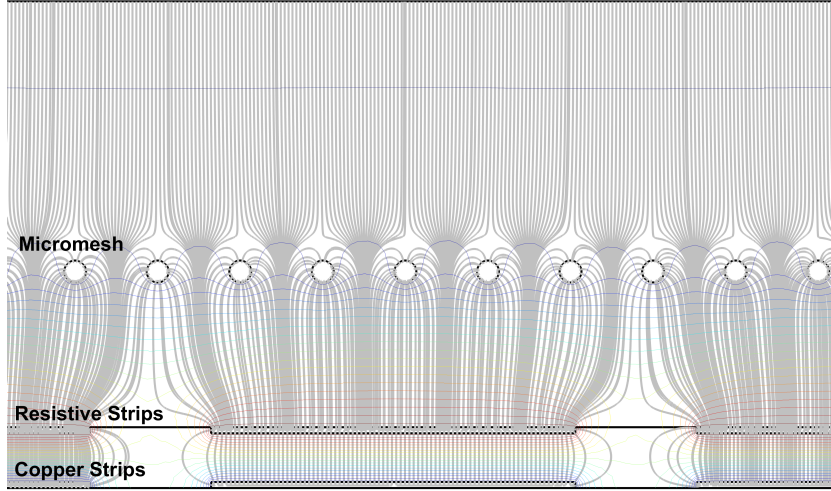


Figure 3.7: Electric field (in gray) and equipotential lines (coloured) within a MicroMegas detector. Both in the drift and amplification regions, the electric field is homogeneous.[64]

to a magnetic field of ~ 0.4 T, causing a Lorentz angle of $\sim 3^\circ$, which is a negligible effect using a combination of appropriate track reconstruction methods.[59] In particular, for the NSW MicroMegas, a combination of the following clustering algorithms is used:[66]

- The *centroid method*, where the hit position is calculated as the average position of strips in a cluster (x_i), weighted by their charge (q_i): $x = \frac{\sum_i x_i q_i}{\sum_i q_i}$. This method provides a good result for tracks perpendicular to the MicroMegas plane, but provides degraded resolution as the incident track angle increases.
- The μ TPC *method*, in which the hit position is defined as the x -coordinate of the reconstructed track at half gap. This method is based on measuring the drift time of the electrons with respect to an external reference time. As the incident angle of the particle increases, the μ TPC method provides better position resolution. Since the expected incident angle in the NSW MicroMegas is in the range 8° to 32° , the μ TPC method is usually preferred as reconstruction algorithm.

3.4. THE MICROME GAS SM1 QUADRUPLETS

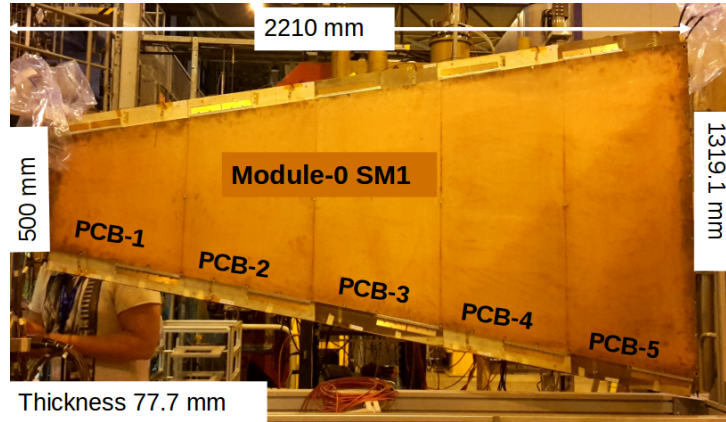


Figure 3.8: Picture of the SM1 Module-0 quadruplet during the test beam at CERN. Built in 2016, it is the first prototype of a SM1 MicroMegas quadruplet. The corresponding dimensions are reported on.[72]

3.4 The MicroMegas SM1 quadruplets

The previous section described the structure and the operating principle of a single NSW MicroMegas detector layer, but each NSW sector contains two MicroMegas quadruplets. As shown in Fig. 3.9, a SM1 MicroMegas quadruplet (or multilayer) consists of three drift panels, two readout panels and four micromeshes. Both the drift and readout panels have trapezoidal shape with a surface of about 2 m², and they are segmented in 5 PCBs (see Fig. 3.8) with an internal structure of aluminum internal-frames and honeycomb sheets used as reinforce.

A quadruplets consists of three drift panels (2 externals and 1 central), for a total of four MicroMegas detector layers. In particular, only one side of the external drift panels corresponds to a MicroMegas layer, while for the central drift panel both sides are used. The drift panels, made of FR4, integrate the copper cathode plane, the gas distribution system (by means of apposite gas distribution pipes) and the mesh-frames which support the micromesh. Each of the four drift plane is separated from one readout plane by a set of gas gap-frames placed around the detector perimeter, and forming a gas-gap filled with Ar:CO₂ (93:7) at an overpressure of 2 mbar. As shown in Fig.

3.4. THE MICROMEGAS SM1 QUADRUPLETS

3.9, the gas-gap tightness is ensured by an O-Ring which groove is delimited by the gas gap-frames and mesh-frames. Both the gas-gap frames and mesh-frames are aluminum bars precisely machined in height. The mesh frames have grooves on the surface where the mesh is glued. In this way the excess of glue can be collect in the grooves ensuring the mechanical contact between mesh and mesh-frames. Moreover in order to guarantee the correct distance between the mesh and the drift plane, the mesh-frames have a groove on the surface in contact with the drift panel.

Due to the overpressure of each gas-gap, the MicroMegas detector blows up during the operation. To avoid the blow up, and minimize the deformation of the whole MicroMegas quadruplets, four interconnections are used to keep the quadruplets thickness constant.[67]

To separate the drift region from the amplification one, a stainless steel floating mesh is contained in each gas gap. The mesh, stretched at a tension of $7 - 10$ N/cm, consists of $30 \mu\text{m}$ wires arranged with a pitch of $80 \mu\text{m}$, and it is glued on the drift panel mesh-frames.

Each readout panel consists of two readout boards disposed in a “back-to-back” configuration. One readout panel, so-called **η -panel**, is designed to measure the η -coordinate, and it is equipped with strips parallel to the bases of the MicroMegas trapezoid. The other readout panel, so-called **stereo panel**, is designed to measure the ϕ -coordinate, and it is equipped with strips with an inclination of $\pm 1.5^\circ$. In order to precisely align the readout panels during the quadruplet assembly, two alignment pins are perpendicularly glued on the η -panel, while alignment inserts are embedded in the stereo panel.

The INFN Collaboration is in charge to assembly 34 SM1 MicroMegas quadruplets⁶ in the period 2017 – 2019. The mass production is already started and it is carried out by the following INFN institutions: Cosenza, Lecce, LNF, Napoli, Pavia, Roma1 and Roma3. The first SM1 MicroMegas quadruplets prototype, so-called SM1 Module-0 (see Fig. 3.8), was completed

⁶About 32 quadruplets will be installed in the NSW, and 2 are built as spares.

3.5. MAIN ASPECTS OF THE CONSTRUCTION PROCEDURE

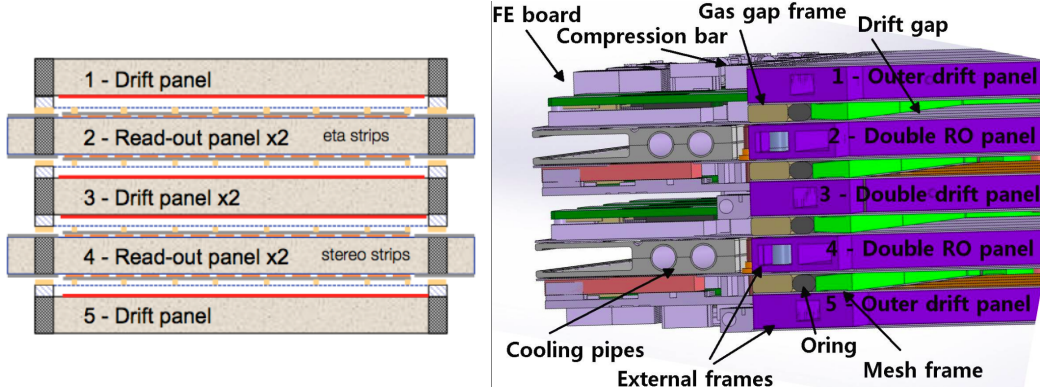


Figure 3.9: Quadruplet structure: on the left is shown a sketch of the structure of a MicroMegas quadruplets highlighting the back-to-back configuration of the readout boards, while on the right a more detailed cross section view is shown.

in May 2016 and tested at CERN with high 180 GeV/c pion beam at a rate from 1 kHz to 0.5 MHz. Spatial resolution results on η -coordinate and ϕ -coordinate, calculated for perpendicular tracks, are reported in Fig. 3.10. The spatial resolution for the precision coordinate is obtained by subtracting the positions reconstructed by the two active layers of the η -panel. For the second coordinate, the spatial resolution is obtained by the combination of the positions reconstructed on the two stereo layers. The spatial resolutions obtained are within the requirements, see 3.2[73]

3.5 Main aspects of the construction procedure

This section briefly describes the construction of a SM1 MicroMegas quadruplet by the INFN Collaboration, highlighting the main aspects of the assembly. The construction is a challenging not only for the large area of each quadruplet, but also because, in order to achieve the 15% p_T resolution for 1 TeV muons, high mechanical precision is required for each panels of the MicroMegas quadruplets. In particular, the required precision on the strips alignment is 30 μm for the η readout panels (dedicated to the precision coordinate measurement), and 80 μm for the stereo readout panels (dedicated to the second coordinate measurement). A summary of the main **construction**

3.5. MAIN ASPECTS OF THE CONSTRUCTION PROCEDURE

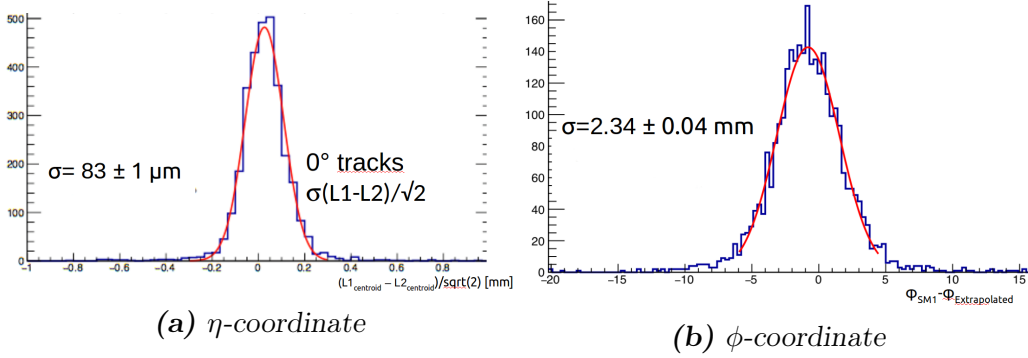


Figure 3.10: SM1 MicroMegas Module-0 space resolution measured in a test beam at CERN. Fig. 3.10a and Fig. 3.10b show the η -coordinate and ϕ -coordinate positions, respectively. The spatial resolutions, given by the width of the distributions, are within the ATLAS requirements.[73][72]

Parameter	Requirement
Panel planarity	RMS: 37 μm Max. deviation: 110 μm
Strips position	Max. deviation: 40 μm
Strips alignment on single RO layer	RMS on η coordinate: 30 μm RMS on z coordinate: 80 μm
Strips alignment on more RO layers	Max. deviation: 60 μm

Table 3.2: Summary of MicroMegas construction requirements. The first section refers to the requirements on the planarity of each MicroMegas panel; the second one to that on the readout strip position; the third one to that on the strips alignment on a single active layer; the last one to that on the strips relative alignment on two or more active layers. The maximum deviation is calculated with respect to the nominal value.

requirements is reported in Tab. 3.2.

As shown in Fig. 3.11, the drift panels are built at *Roma1* using a vacuum bag tool; the readout panels are built in *Pavia* taking advantage of the stiffback technique; the mesh stretching operation is done at *Roma3*; while the drift panel finalization⁷ is carried out at Frascati Laboratori (LNF) by *Cosenza*, *Lecce* and *Napoli* and *Roma3*; finally the vertically quadruplet assembly is done at LNF. The Cosenza, Lecce and Napoli groups also contribute to the MicroMegas construction through the realization of hardware and software tools and the Quality Assurance and Quality control (QA/QC) tests.

3.5.1 Construction of readout panels

Built by the INFN Group of Pavia, the SM1 readout panels construction[74] is based on the *stiffback technique*, see Fig. 3.12. This method allows to build a readout panel with the nominal thickness, compensating for all the possible imperfections in the thicknesses of the panel components.

The readout panel construction starts with the **QA/QC of all the components**⁸. The frames and the cooling bars thickness is checked with pass/fail limbo tool, and about a 10% of frames are measured with a Mitutoyo linear height every 10 cm on each side, in order to have a more accurate measurement. During this phase, all PCBs are brushed in a tub with warm water (30°C) and NGL detergent with a concentration of 10 g/l, and then the PCBs are washed with high pressure demineralized water. After the PCB cleaning and a visual examination to check the presence of all the pillars, the QA/QC operations allow to verify: (i) the isolation between resistive and copper strips,(ii) the isolation of the silver line, (iii) the HV connection to the resistive strips, (iv) and the resistance of the resistive strips. Moreover, with an accuracy of 3 μm , it is measured the thickness of each PCB board (almost 270 measurements per PCB sheet) using the CMM (Coordinate Measuring Machine).

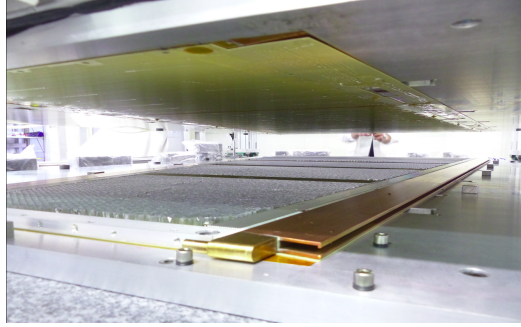
⁷Detailed described in Sec. 3.6

⁸Regarding the PCBs, the main QA/QC is performed by a dedicated group at CERN, which is also in charge of minor repairs that may be needed.

3.5. MAIN ASPECTS OF THE CONSTRUCTION PROCEDURE



(a) MM SM1 drift panel



(b) MM SM1 readout panel



(c) Table for mesh stretching



(d) Quadruplet assembly

Figure 3.11: Picture showing the main components of a MicroMegas quadruplets: the Fig. 3.11a shows a drift panel built at Roma1, Fig. 3.11b shows a readout panel built in Pavia, Fig. 3.11c shows the table used for stretching the mesh (the transfer frame structure is on the table). Finally Fig. 3.11d shows the vertical assembly at LNF. All the pictures refer to the construction of the MicroMegas SM1 Module-0.

The readout panel construction continues with the **dry run**. This phase consists of a repetition of the assembly without using glue, and it allows to verify the compatibility among the panel components.

The next step is the **panel assembly** (see Fig. 3.12). This phase is carried out on a single day using a granite table (certified to have a maximum deviation of $8 \mu\text{m}$), and a stiffback with the same dimension of the granite table. The stiffback can be moved horizontally, vertically and can be rotated. Both on the granite table and on the stiffback, 5 reference plates are fixed,

3.5. MAIN ASPECTS OF THE CONSTRUCTION PROCEDURE

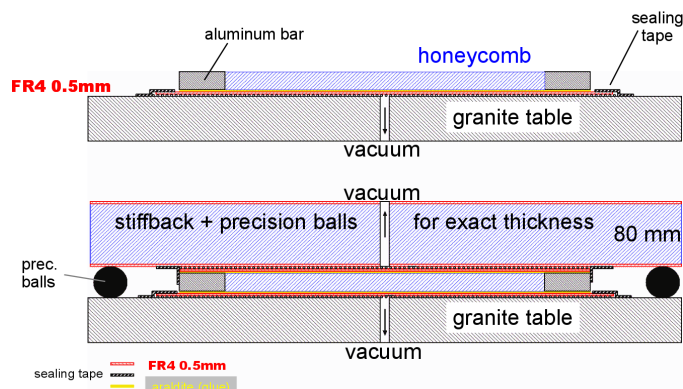


Figure 3.12: Schematic view showing the construction technique of SMI MicroMegas drift panel (up) and readout panel (down). The drift panels are assembled using the vacuum bag tool, while the readout panels are built using the stiffback technique.

see Fig. 3.13a. Each reference plates, with a dimension of $145 \cdot 49 \cdot 2 \text{ cm}^3$ and a planarity of $20 \mu\text{m}$, has pass-through holes in order to allow the vacuum sucking during the panel gluing.

The assembly starts with the positioning of 5 PCB sheets both on the granite table and on the stiffback, in correspondence of the position of the 5 reference plates. The PCBs are fixed on the reference plates by vacuum sucking, but they are mechanically positioned using Teflon precision pins (achieving a tolerance of $30 \mu\text{m}$). Moreover, the PCBs positioning is checked using RASNIK[75] (Red Alignment System of NIKhef) sensors which read the corresponding masks printed on the PCB boards, see Fig. 3.13b.

After the PCBs positioning on the granite table and on the stiffback, they are covered with glue (Araldite 2011), which is deposited according to a predetermined pattern using a dispenser remotely controlled.

All the other panel components are placed above the 5 PCBs on the granite table. In this phase 20 ground “spider” connectors are inserted in order to guarantee the electrical grounding of the honeycomb sheets, internal and external frames. The assembly phase continues with the positioning of the stiffback on the granite table, and the closing of the readout panel. After the glue curing, the last step of the assembly is to insert of 2 *alignment pins* of 6 mm of diameter, on the stereo readout panel, and to embed 2 *alignment*

3.5. MAIN ASPECTS OF THE CONSTRUCTION PROCEDURE



(a) Reference plates

(b) cCCD camera

Figure 3.13: Pictures showing the tools used for the readout panel construction in Pavia. Fig. 3.13a shows the 5 reference plates laid on the granite table. Fig. 3.13b shows a contact-CCD camera placed on a reference plates. It is used to read the RASNIK masks printed on the PCBs, in order to guarantee the correct PCB positioning during the assembly.[74]

inserts on the η -panels. Both alignment pins and inserts have a relative clearance of $25 \mu\text{m}$ at the maximum. As will be described in Sec. 3.5.4, pins and inserts are used for the alignment system during the MicroMegas quadruplet assembly at LNF.

Finally, a set of **QA/QC tests on the readout panel** are performed. The electrical tests are identical to the ones performed at the beginning to a single PCB, in order to determine a possible PCBs quality deterioration during the construction. Also a visual examination is performed in order to detect potential detached cabling or cold soldering. In this phase is also performed a gas tightness test on the readout panel using an apposite experimental setup⁹.

3.5.2 Construction of drift panels

Built by the INFN Group at Roma1, the SM1 drift panels construction takes advantage of the *vacuum bag technique*, see Fig. 3.12.[76] This method relies on the flatness of the granite table and allows to obtain good planarity results. The construction procedure is performed in “one-step gluing” for

⁹Since the gas tightness test is performed in the same way on the drift panel during the finalization procedure, it will be described in Sec. 3.6.8 and in Appendix II

3.5. MAIN ASPECTS OF THE CONSTRUCTION PROCEDURE

external drift panels, and “two-step gluing” for central drift panels. The preliminary QA/QC test of the honeycomb sheets, internal aluminum frames and PCB sheets are similar to that described for the readout panels.

For the external drift panel the one-step technique can be summarized as follow: The 5 PCB-sheets forming a drift-plane are positioned on the planar reference table by use of exact distance pieces aligned against an external frame. Using glue dispenser remotely controlled, the Araldite 2011 is uniformly distributed (following a specific path) on the PCBs, and the panel internal components (aluminum internal bars and aluminum honeycomb sheets) are placed on top of the PCBs. The ground “spider” connectors are screwed in order to ensure the electrical connection among all the metallic parts. The 5 outer PCBs are then placed on top of all to form the entire panel and the vacuum bag turned on with an underpressure of about 100 mbar.

For the central drift panel construction, the 5 PCB-sheets and the internal panel components are glued first and the vacuum bag turned on. After glue curing the first PCB layer is removed and the second set of PCBs-sheets are positioned on the granite table. The glueing procedure with the vacuum bag is repeated once again.

As shown in Fig. 3.14, as QA/QC test, a limbo test is performed on the drift panels in order to verify that the construction requirements are respected.

3.5.3 Mesh stretching

The stretching of the micromesh is carried out by the INFN Group of Roma3, using tools and tables specially designed. Here a summary of the stretching procedure:

1. The “transfer frame” is positioned on the mesh-stretching-table, see Fig. 3.11c.
2. The micromesh is positioned on the table above the transfer frame and all the clamps of the table are connected to pre-calibrated load cells.

3.5. MAIN ASPECTS OF THE CONSTRUCTION PROCEDURE

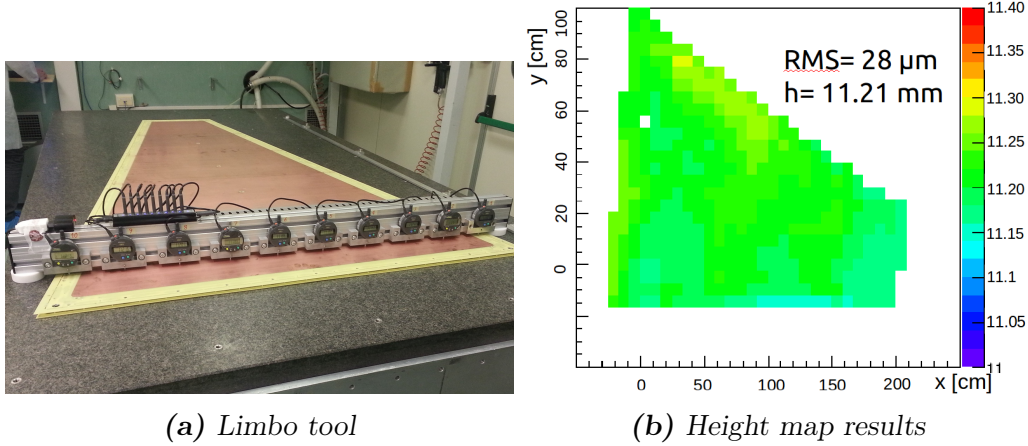


Figure 3.14: Limbo test performed to verify the planarity of drift panels at Roma1: Fig. 3.14a displays the limbo tool with 10 Mitutoyo micrometers, while Fig. 3.14b shows the map of the height distribution of a drift panel.

3. Using an Arduino based data acquisition program, it is possible an on-line monitoring of the tension applied on each clamp. Clamps are pulled until each of them reaches the tension $\sim 162\text{N}/18\text{cm}$, corresponding to $\sim 9\text{N}/\text{cm}$.
4. A tensiometer is used to measure the tension of the mesh in different positions, see Fig. 3.15.
5. When the mesh is well stretched, it must be glued on the transfer frame in order to be transported to LNF. Therefore, the transfer frame is lifted to the mesh, and a fast-curing glue ($\sim 4 - 5$ hours) is distributed all over its perimeter. The glue is also distributed on the external side of the transfer frame in order to avoid fraying when the mesh is cut to be separated from the table. Experimentally, it is observed a drop of tension of about $2 \text{ N}/\text{cm}$ after the gluing of the mesh on the transfer frame.
6. Interconnection holes must be created on the stretched mesh. This operation is carried out on a specific table containing positioning supports to fix the transfer frame, and supports to individuate the exact positions in which the holes must be created. An apposite drilling machine

3.5. MAIN ASPECTS OF THE CONSTRUCTION PROCEDURE



Figure 3.15: Measurement of the tension of a mesh in different position using a tensiometer.

is used to perform interconnection holes without mesh frying.

3.5.4 Quadruplet assembly

Once the five panels are constructed and the four meshes are stretched, all these items are transferred to LNF where the quadruplets assembly is carried out. As shown in Fig. 3.11d the SM1 MicroMegas quadruplet assembly is performed using a vertical mounting structure. To avoid dust particles that can produce current bridge over the $128 \mu\text{m}$ between the mesh and the readout structure, the assembly takes place in a clean room, controlling temperature and humidity.[59] The assembly process starts inserting, in the vertical mounting structure, one of the two external drift panels. As shown in Fig. 3.11d, in order to avoid the bending of the panel under the torque due to the stretched mesh, the external drift panel is mounted on stiffening frames. The other panels are then guided by a linear bearing system for alignment on z and x -axis, while during the y -alignment load cells and micrometric screws are used.

During the assembly process, the precise alignment between the five MicroMegas panels is ensured by 2 alignment pins mounted perpendicularly on the η -panel and by 2 alignment insert embedded on the stereo panel. The precision pins and inserts must have a relative clearance of $25 \mu\text{m}$ at the

maximum. Each time a drift and a readout panel are combined, a HV test will be performed in order to detect problems due to remaining dust particles that have to be removed before final assembly. When all panels are put together with precise alignment, the quadruplet is fixed with screws and the external stiffening frames are removed.[67]

3.6 Drift panel finalization

As described in the previous section, the drift panels are constructed at Roma1 as “bare panels”. Therefore, before assembling a SM1 MicroMegas quadruplets, the following elements need to be added: mesh-frames, O-Ring, gas-gap frames and micromesh. Fig. 3.16 shows an exploded view of a “complete” drift panel ready for the mesh gluing. The complete set of operations needed to be performed on the drift panel is called “drift panel finalization”, and it is carried out at LNF with the collaboration of technicians and physicists of Cosenza, Lecce and Napoli. Moreover, before the quadruplet assembly, at LNF are also performed a set of QA/QC tests on the drift panels in order to verify that all the construction requirements, reported in Tab. 3.2, are satisfied.

Here a short summary of the finalization procedure:

1. A visual examination of the bare drift panel is performed in order to detect potential defects like holes filled with glue. In this case it has to be removed.
2. The PCB-PCB junctions are sealed with epoxy glue, while the interconnection drift spacers and the HV connectors glued on the drift panel.
3. The local gas tightness test is performed on all the drift panel holes, as well as on the PCB-PCB sealed junctions in the region of the O-Ring groove.
4. The height of all the interconnection drift spacers mounted in 2 is measured.

3.6. DRIFT PANEL FINALIZATION

5. The five PCB cathodes are electrically connected together and the electrical continuity among them is tested.
6. The mesh-frames, mesh-corners, gas-gap frames and gas pipes are glued on the drift panel. Electrical test are performed to verify the mesh-frame continuity with the panel ground and the isolation between cathode and ground.
7. The drift panel gas tightness test is performed. The test takes few hours and the leak rate must be less than the ATLAS specifications. Only if the drift panel has passed all the QA/QC tests, it is ready to the mesh gluing.
8. The mesh is carefully washed within a dedicate washing cabin. After one day of drying, the mesh is glued on the drift panel. The process is carried out in a clean room in order to avoid dust particles on the mesh. The mechanical tension is measured after glue curing when the mesh is separated by the transfer frame.
9. Finally, the HV test is performed. An HV of 500 V is applied on the cathode plane of the drift panel, while the mesh is grounded, and the current is monitored for about half an hour. The QA/QC test is successfully passed if the current is under 5 nA.

This section describes in detail the main phases of the SM1 drift panel finalization, showing also the QA/AQ controls and the tools or infrastructures used.

3.6.1 Finalization-tables

A set of four multi-purpose “finalization-tables”, with same shape and dimensions of the SM1 drift panels, were designed to carry out all the operations for finalizing the drift panels (both central and external): cleaning, sealing, gluing and testing. In particular, one table is used only for cleaning and sealing, another one is used also to perform the gas tightness test, and the last two are used only for the mesh gluing. Moreover, as shown in Fig.

3.6. DRIFT PANEL FINALIZATION

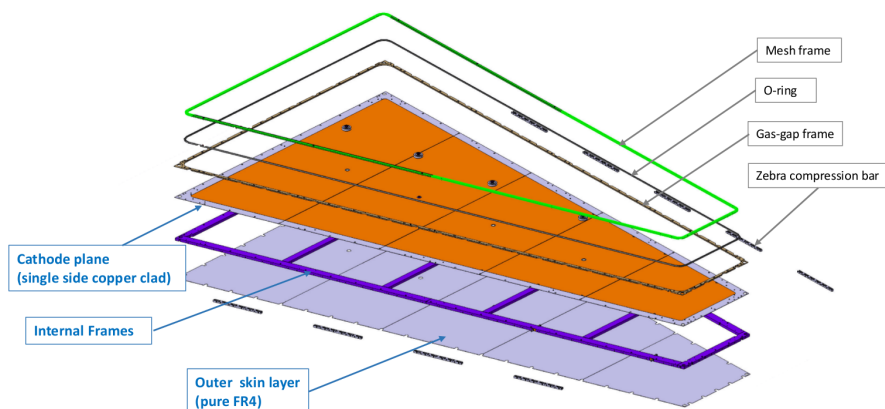


Figure 3.16: Exploded view of a SM1 drift panel, showing all its component. The bare drift panel is constructed at Roma1, while the mesh-frame, gas-gap frame and O-ring are inserted during the finalization procedure at LNF.

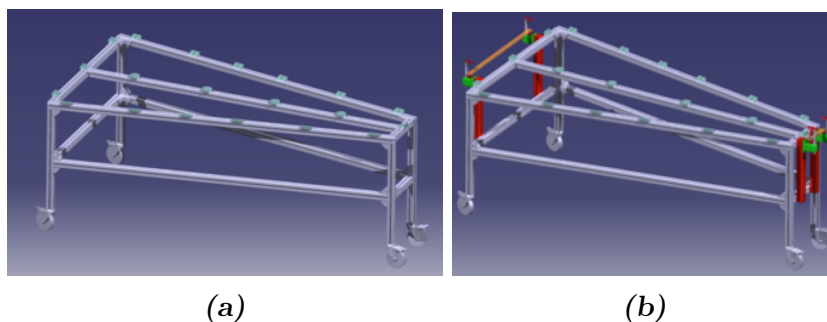


Figure 3.17: Fig. 3.17a shows the structure of the finalization-table with the panel supports (green), while Fig. 3.17b shows the transfer frame support (aluminum bars in orange) and the four clamps (threaded brass rods) mounted on the two bases. Lateral clamps are missing in this drawing. Technical designed by Roscilli Lorenzo.

3.6. DRIFT PANEL FINALIZATION

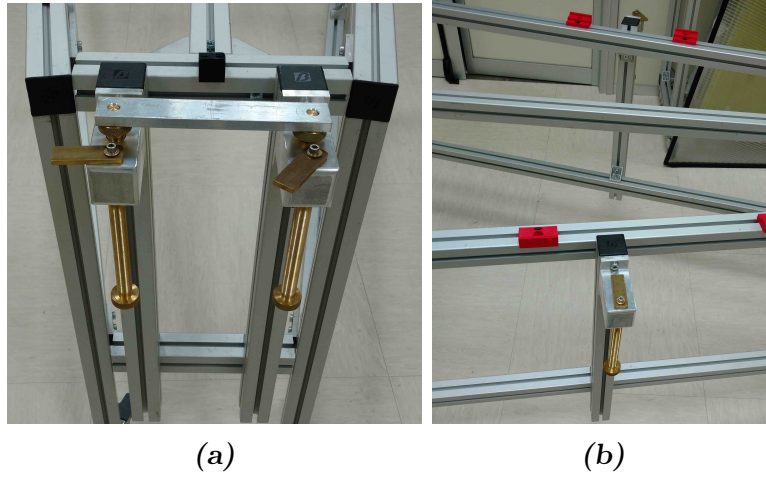


Figure 3.18: Fig. 3.18a shows the small base of the finalization-table with its clamps (brass threaded rods) and the support of the transfer frame (aluminum bar). Fig. 3.18b shows the transfer frame clamp on the lateral side of the finalization-table.

3.17a, the finalization-table sustains the panel only in few points: along its perimeter and at the interconnection positions.

A special set of tools can be added to allow the precision positioning and clamping of the transfer frame during the mesh gluing on the drift panel (see Fig. 3.17b). In particular, Fig. 3.18a and Fig. 3.18b show the clamps along the small base and the lateral sides of the finalization-table, respectively.

The finalization-table used for gas tightness test is equipped with reinforces under the support at the interconnection position (see Fig. 3.19a). As will be described in Sec. 3.6.8 and Appendix ??, to perform the gas tightness test, the selected drift panel is enclosed into a couple of aluminum gas-tight panels (so-called vessel), and placed on the proper finalization-table. To avoid the utilization of the interconnections, an exoskeleton is placed on top of the vessel in order to prevent possible deformations (see Fig. 3.19b).

3.6.2 Sealing procedure of PCB-PCB junction

The four PCB-PCB junctions on drift panels are sealed with a continuous filament of glue Araldite 2011 for the whole length of the junction along a

3.6. DRIFT PANEL FINALIZATION



Figure 3.19: Finalization-table for the gas tightness test with all its elements: aluminum structure with the reinforce bars at the interconnection position (3.19a), vessel and exoskeleton (3.19b).

PCB side. The reason for extending the sealing along the whole junction is to avoid the risk of gas leaks due to imperfect bonding of the Kapton tape between two adjacent PCB on the internal side of PCB. To better size the amount of glue to distribute along the junction, a strip of adhesive tape (0.05 mm width) is placed at 0.5 mm from the edge of each PCB. The continuous filament of glue fills the gap between the two adhesive tapes.

After 30 minutes, the polymerization of the two components of glue is well started, and its viscosity has reached the minimum value. With the aid of a *spatula*, the glue is pushed into the junction and the excesses of glue are removed using the edge of a plastic parallelepiped forcefully creased along the two strips of adhesive tape. Then the two strips of adhesive tape are removed and the panel untouched until the glue is cured.

When the glue is completely cured, a step of few tenths of microns is present along the whole PCB-PCB junction, therefore, it is necessary to remove it in the region of the O-Ring groove, and in the region in which mesh-frame and gas-gap frame will be mounted. The smoothing of the area is done with 1000/2000 abrasive paper in alcohol and finished with abrasive paste. Finally, a local gas tightness test (described in Sec. 3.6.4) is performed on the sealed junction in correspondence of the O-Ring groove.

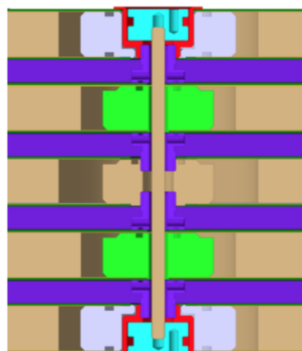


Figure 3.20: The interconnection system is formed by 14 elements: 4 drift spacers (in purple), 2 end-plugs (in light blue), 2 internal disks glued inside the outer drift panels (in light violet), 2 internal disks glued inside the readout panels (in green), 1 internal disk glued inside the central drift panel (in light brown), 1 treaded road (in brown) and 2 holders for the end-plugs (in red).[59]

3.6.3 Positioning of the interconnection drift spacers

As it may be seen in the drawing of the interconnection system, see Fig. 3.20, five pieces are glued inside the panels during the construction, instead six are glued during the panel finalization: two holders (in red) and 4 “drift spacers” (in light purple). The interconnection drift spacers defines the height of the drift gap, therefore, they must be positioned and glued on the drift panel defining precisely the height.

In order to glue the interconnection drift spacers obtaining with a tolerance of $25\ \mu\text{m}$, a special tool has been developed (see Fig. 3.21a). It consists of a precision disk in stainless steel and of a brass three-arms-holder. The dimensions of the precision disk have been decided after tests performed on a drift panel prototype, and they are: 5.100 mm of height and 50 mm of external diameter. Three steps are necessary to glue the interconnection drift spacers to the panel:

1. the disk is placed on the drift panel in correspondence of one interconnection hole,
2. the spacer is screwed into the holder (see Fig. 3.21b) and a small amount of glue Araldite 2011 is distributed on the spacer screw by means of a

3.6. DRIFT PANEL FINALIZATION

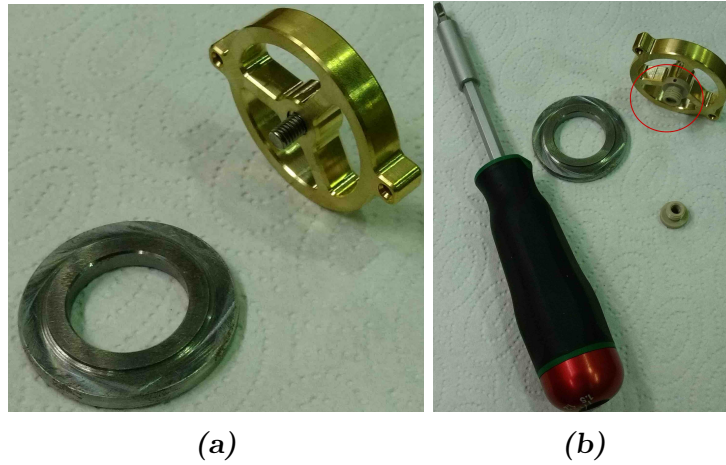


Figure 3.21: Fig. 3.21a shows the tools used to position precisely in height the interconnection drift spacer: a precision stainless steel disk and a three-arms-holder. Fig. 3.21b shows the spacer screwed to the holder (red circle) and the dynamometric key used to screw the holder into the internal interconnection disk.

syringe,

3. the holder is screwed to the internal interconnection disk by means of a dynamometric key.

After glue curing the three-arms-holder is unscrewed and the height of the interconnection drift spacer with respect to the cathode surface is measured by means of a micrometer¹⁰. Although, screwing the three-arms-holder on the internal interconnection disk with a certain torque may deforms locally the panel, when the torque is removed the panel comes back to its equilibrium position and the height of the spacers with respect to the cathode surface agrees with the technical specifications.

3.6.4 Local gas tightness test

In order to test the gas tightness of all the drift panel holes, and of all the PCB-PCB junctions (already sealed), a set of testers head are employed. Fig. 3.22a shows the three types of testers head designed for a proper utilization:

¹⁰The height measurements will be described in Sec. 3.6.7

3.6. DRIFT PANEL FINALIZATION

- the tester head with the smallest O-Ring is used to test the holes in which the mesh-frame will be screwed, the gas inlet/outlet holes, and the PCB-PCB sealing in the O-Ring groove.
- The tester head with the biggest O-Ring is used to check the tightness of interconnections.
- The last tester head is used to test the tightness of the HV holes.

The local gas tightness test is performed positioning the tester head, on a selected region. A weight is placed over the tester head, causing a compression both of the O-Ring and of the air contained in the tester head. Therefore, the pressure inside the tester head increases slowly till the O-Ring reaches the equilibrium under the weight and the overpressure is maximum. The pressure is then monitored for 10 s and the leak rate measured.

If the tested region (hole or PCB-PCB sealing) is gas leaking, the pressure inside the tester head decreases with a loss-dependent velocity. In this case, the region must be better sealed with glue Araldite 2011, and the test must be repeated after the glue cured. On the contrary, the local gas tightness test is successfully passed if the leak rate is 10^{-8} bar l/s.

Because the tester head volume is small (from 0.2 to 1 ml, depending on the selected head) and the pressure sensor sensitivity is 3.125 mbar/V, the resolution of the local gas tightness test is about 10^{-9} bar l/s.

When the local gas tightness test is performed on the interconnection of the central panel, a special end-cap (see Fig. 3.22b) is screwed onto the interconnection drift spacer on the other side of the central drift panel.

3.6.5 Positioning of mesh-frames

As already seen, mesh-frames and mesh-corners consist of aluminum frames, placed along the drift panel perimeter, and used to attach the floating micromesh to the drift panel. They are glued with Araldite 2011 directly on the drift panel, and screwed to its internal frames. The screws serve both to ground the mesh-frame to the internal frames, and to fix the mesh-frames to the panel. First of all, the Araldite 2011 is distributed in the apposite

3.6. DRIFT PANEL FINALIZATION

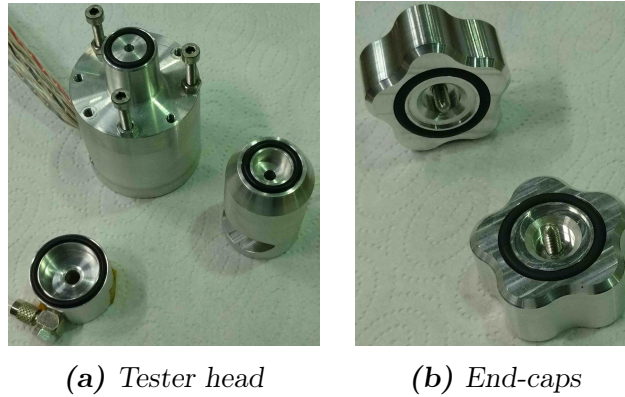


Figure 3.22: Fig. 3.22a shows the 3 types of tester head used for the local gas tightness test, while Fig. 3.22b shows the end-caps used in the gas tightness test of the interconnections of the central drift panel. The end-cap is screwed on opposite side of a selected interconnection, while the tester head is placed on the interconnection itself.

groove of each mesh-frame on the side that will be in contact with the drift panel. For this operation an appropriate tool is used¹¹. Then, the mesh-frame is carefully placed on the drift panel aligning the mesh-frame holes with the corresponding holes on the panel. In order to guide the positioning of the mesh-frames, and ensure the alignment of the holes, a set of plastic positioners (made with a 3-D printer) is used.

As shown in Fig. 3.23a, there are three types of positioners corresponding to different positions on the drift panel: major base, minor base and sides. As shown in Fig. 3.23b, on the bottom side of each positioners, there are 2 alignment pins used both as reference for the positioning and to block the mesh-frames in the correct position. While the mesh-frames are blocked, they are screwed to the panel. The positioners are then removed, and the same gluing operation is repeated for the mesh-corners. During the glue curing, an homogeneous weight is applied on the mesh-frames, using a heavy trapezoidal-shape frame (see Fig. 3.24).

¹¹Detailed described in Sec. 3.6.6

3.6. DRIFT PANEL FINALIZATION

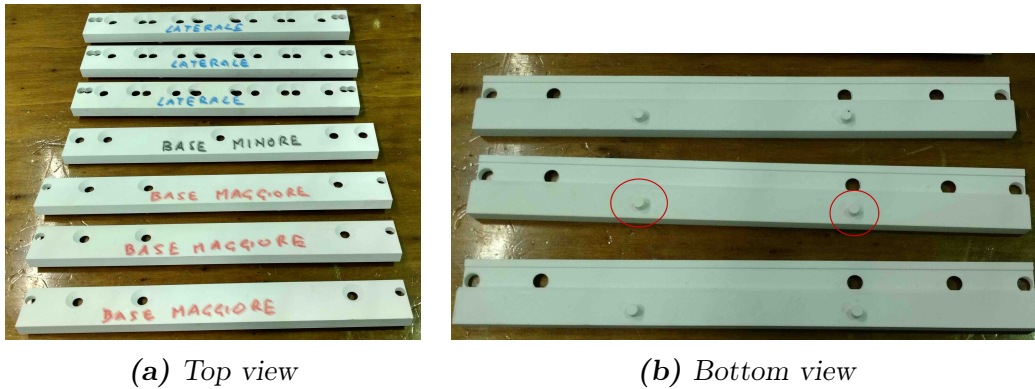


Figure 3.23: Positioners using during the mesh-frames gluing: Fig. 3.23a and Fig. 3.23b show the top view and bottom view of mesh-frame positioners, respectively. The alignment pins (red circle) are visible on the bottom view.



Figure 3.24: Frame used to press mesh-frames and mesh-corners on the drift panel during the glue curing.

3.6. DRIFT PANEL FINALIZATION

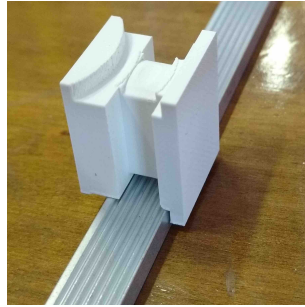


Figure 3.25: *Glue dispenser tool used both for gluing mesh-frames on drift panel, and for gluing the mesh on mesh-frames. A small amount of glue is distributed within the mesh-frames groove, then the dispenser is crawled along the mesh-frame to spread the glue inside the glue slots avoiding soiling the edges of the mesh-frame.*

3.6.6 Glue dispenser tool

It is very important to distribute the correct amount of glue both between mesh-frames and drift panel, and between mesh-frames and mesh. In fact, the correct distance between the micromesh and the cathode surface must be guaranteed avoiding glue excess, and ensuring the mechanical contact between the elements.

The mesh-frames has grooves both on its bottom (side in contact with the drift panel) and on its top (side in contact with the mesh) to collect glue excesses respectively during the gluing of mesh-frames on drift panel, and during the gluing of mesh on the mesh-frames. A glue dispenser, specifically designed to distribute the correct amount of glue is used for both the gluing processes, see Fig. 3.25. The gluing starts with the distribution of a filament of Araldite 2011 in the apposite mesh-frame groove, then the glue dispenser tool is drag on the mesh-frame to completely fill the groove. Two or three applications are sufficient to fill completely and uniformly the glue slots.



Figure 3.26: The micrometer on its holder during three different measurement: Fig. 3.26a shows the zeroing on the brass disk; Fig. 3.26b shows the height measurement of a interconnection drift spacer; Fig. 3.26c shows the measurement of the mesh-frame height.

3.6.7 Measurement of interconnection drift spacer and mesh-frame height

The height of the interconnection drift spacer and mesh-frame have stringent tolerances ($25 \mu\text{m}$) because they define the mesh distance from the cathode. Therefore, after each gluing¹² the height of these parts are measured using a micrometer mounted on a special holder (see Fig. 3.26). As shown in Fig. 3.26a, to measure the interconnection drift spacer height the micrometer is zeroed very close to it on a small brass disk of 3 mm thickness. Then, as shown in Fig. 3.26b, the small disk is placed on top of the interconnection drift spacer and the tip of the micrometer put in contact with the disk measuring the height of the spacer along the maximum circumference in four points.

On the other hand, as shown in Fig. 3.26c, to measure the mesh-frame height the micrometer is zeroed on a cathode surface, very close to the mesh frame. The mesh-frame height is then measured along all the perimeter every 20 cm. See Fig. 3.27 for the distribution of the heights.

Fig. 3.28 show the distributions of the height measurements of the in-

¹²See Sec. 3.6.3 and Sec. 3.6.5 for the interconnection drift spacer gluing and mesh-frames gluing, respectively.

3.6. DRIFT PANEL FINALIZATION

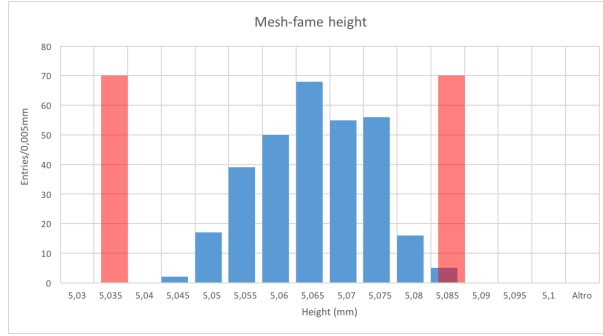


Figure 3.27: Distribution of measurements of the height of mesh frames glued on drift panels.

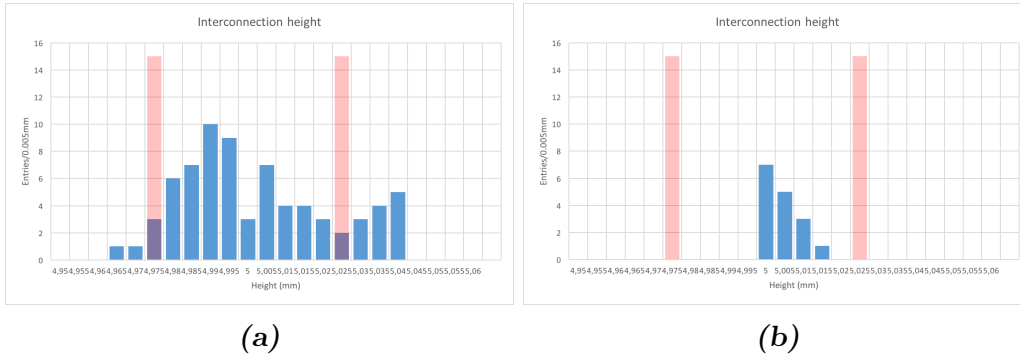


Figure 3.28: The height of the interconnection drift spacers glued on the drift panels. Fig. 3.28a refers to the interconnection drift spacer glued using a plastic precision positioning tool (obsolete), Fig. 3.28b refers to the interconnection drift spacers glued using the metallic precision positioning tool described in Sec. 3.6.3. The red vertical bars represent the limits reported into the NSW specifications.

interconnection drift spacers glued on the drift panels. In particular, at the beginning of the mass production, for the positioning of the interconnection drift spacer, was used a plastic precision tool but the results of the height measurements are not good (see Fig. 3.28a). On the contrary, the measurements of the height of the interconnection drift spacers glued using the procedure and the precision tool (described in 3.6.3), respects the ATLAS NSW requirements and they are shown in Fig. 3.28b.

3.6.8 Measurement of panel gas tightness

After the drift panel has been sealed, the local gas tightness tests performed and the mesh-frame and the gas distribution pipes mounted and glued it is need to certify the gas tightness of the whole drift panel. For this purpose a couple of gas-tight aluminum dummy panels (so-called vessel panels) with same dimension and shape of the SM1 drift panels were built. They serve as vessel in which the drift panel to test is enclosed, and measure of the leak rate is performed after filling the gas-gap created between the vessel panel and the drift panel with air. The central drift panel is coupled with both vessel panels, while the outer one is coupled only with one dummy panel. The O-Ring is mounted onto the drift panel where the gas-gap-frame is screwed in the final position to form the O-Ring groove. Fig. 3.29 show the sequence for coupling a outer drift panel with a vessel panel: mount the gas-gap-frame on the drift panel, insert the O-Ring into the drift panel groove, put the dummy panel on top of the drift panel, put the exoskeleton on top of the dummy panel, clamp the two panels together and plug the electronics and the PC. About 100 ml of air is inserted by means of a syringe into the gas gap and the leak rate deduced by the pressure drop. The differential pressure of the gas-gap is monitored for at least 2 hours (see Appendix II for a detailed description of the gas tightness test). If the air leak rate exceeds the maximum allowed limit, the cause is carefully investigated and solved.

3.6.9 Cold vulcanization of O-Ring and its test

The NSW MicroMegas quadruplets employ a custom soft O-ring constituted by an EPDM elastomer of 7 mm of thickness and Shore 20. The two ends of the elastomer rope are joined using a specific technique, so-called “cold vulcanization”:

1. Both the end on the elastomer rope are precisely and orthogonally cut with a specific tool (see Fig. 3.30a). Then, a thin layer of rubber fast-curing glue (ContiSecur BFA from Continental) is distributed on them, in order to obtain a flat surface.

3.6. DRIFT PANEL FINALIZATION

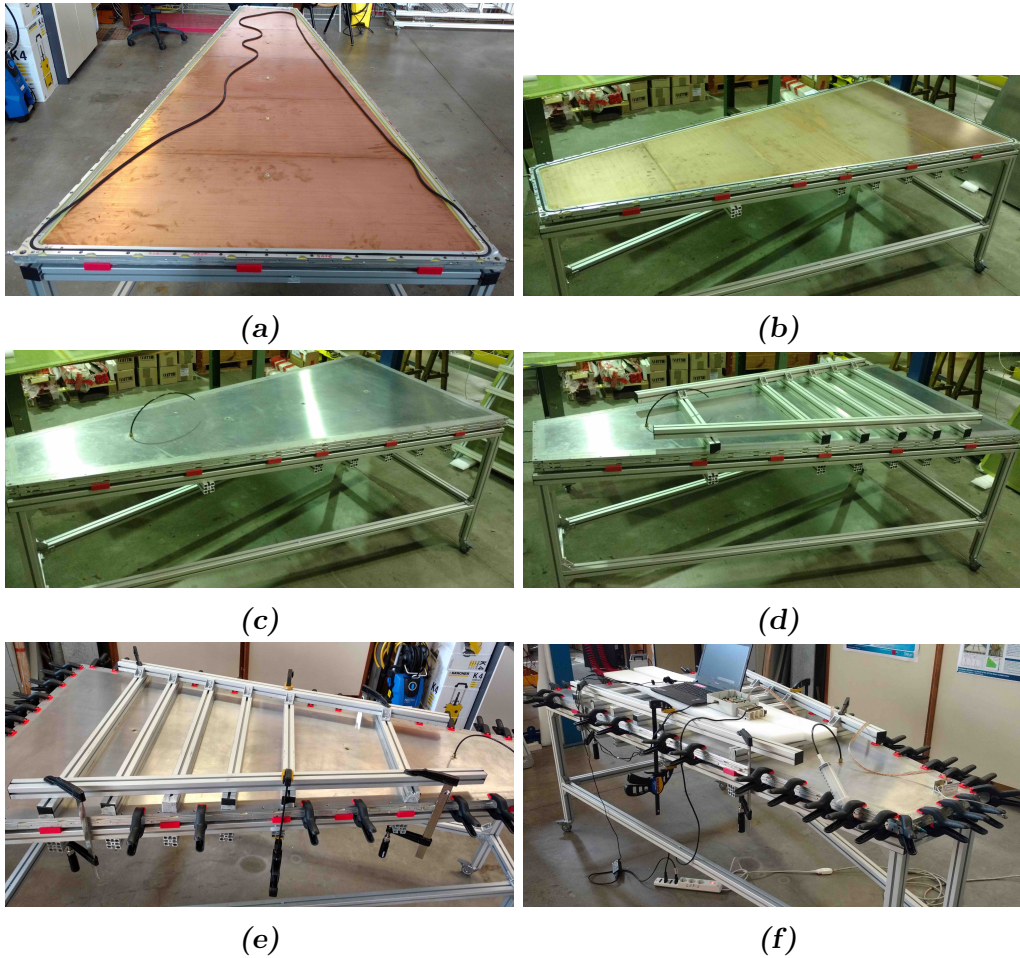


Figure 3.29: Picture showing the procedure to measure the panel gas tightness. Fig. 3.29a shows an outer drift panel is placed on the test-table with the O-Ring partially inserted into its groove; Fig. 3.29b shows the drift panel with the O-Ring; Fig. 3.29c shows the drift panel coupled with an aluminum dummy panel which serve as vessel; Fig. 3.29d shows the exoskeleton on top of vessel to avoid deformation; Fig. 3.29e shows the clamps used to tight the vessel; finally Fig. 3.29f shows the electronics and the air inserting system complete the setup.

3.6. DRIFT PANEL FINALIZATION

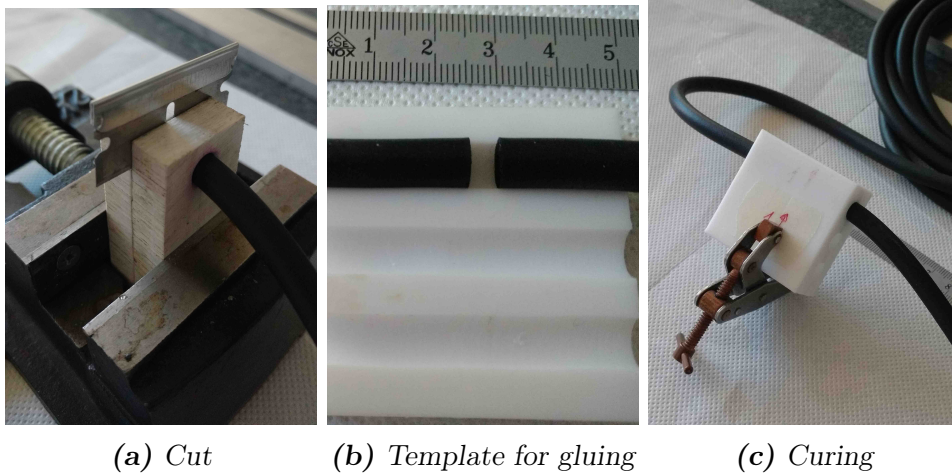


Figure 3.30: Procedure to obtain the O-Ring for each MicroMegas detector layer: the elastomer is cut orthogonally (Fig. 3.30a), then a layer of rubber is distributed on both edges. The two edges are aligned into a template and pushed one against the other (Fig. 3.30b), and left inside it till the rubber is cured (3.30c).

2. After the curing (1 hour) a second layer of rubber glue is distributed on both the ends of the rope, and the two ends are joined using a template in order to obtain a perfect alignment (see Fig. 3.30b).
3. Finally, the template is closed for the rubber glue curing (see Fig. 3.30c).

The rubber is completely cured after 24 hours, then the O-Ring rope is inserted into an apposite table-test to check its gas tightness. The table-test is capable to contain the entire length of the O-Ring but with a path designed to enclose an air volume of 100 ml. The enclosed volume is filled with 2 ml of air and the pressure drop is recorded for 10 min. The maximum air leak of the O-Ring should be 0.04 ml/min.

3.6.10 Mesh washing: procedure and tools

Before gluing mesh on the drift panel, it has to be carefully cleaned. A special tool so-called “washine-cabin” is used at LNF, see Fig. 3.31. The transfer frame on which the mesh is attached, is placed on a cart and pushed

3.6. DRIFT PANEL FINALIZATION



Figure 3.31: The washing cabin operation: the mesh is placed inside the cart and pushed inside the cabin. The cabin door is then closed and the washing start usign high pressure washer. Finally, the mesh is moved in the clean room through a door directly connected to the clean room. Designed by Alessandro Miccoli.

into the washing cabin. A mixture of detergent and warm water (40 °C) is distributed on both side of the mesh using a pressure washer. After 10 minute, the mesh is carefully rinsed with high pressure water at 40 °C. The final rinsing is done with demineralized water. After few minutes, the transfer frame is moved into the clean room through a connecting door, where the mesh will dry for 24 hours on a dedicate support.

3.6.11 Mesh gluing and tension measurement

After the washing and drying, the stretched mesh is ready to be glued on the drift panel. The process can be summarized as follow:

1. the drift panel is placed on the apposite finalization-table, and a correct amount of glue Araldite 2011 is distributed along the mesh-frames by means of the glue dispenser tool described in Sec. 3.6.6.
2. Both the cathode surface and the mesh are cleaned with an antistatic

3.6. DRIFT PANEL FINALIZATION

particle cleaning roller.

3. The transfer frame is placed on the transfer-frame-support of the finalization-table (as already seen in Fig. 3.17b) aligning the mesh with the drift panel. This alignment is reached aligning the interconnection with the corresponding holes on the mesh.
4. The mesh is slowly lowered to the panel until the mesh touches the mesh frame (see Fig. 3.32). The two transfer-frame-supports are then lowered and the six clamps are used to pull down the transfer frame to well fit the mesh to the mesh-frame.
5. The glue is also distributed on the external side of the mesh-frames in order to avoid fraying during the cut of the mesh.
6. The transfer frame is left on the finalization-table for glue curing (1 day).

After the glue curing, the tension of the mesh is measured in different position with a tensiometer (as already seen Fig. 3.15). Then, the mesh is separated from the transfer-frame with a cut closest as possible to the mesh-frames. During the mesh cut a vacuum cleaner is used to remove potential metal dust that can be created. After the cut the measurement of the mesh tension is repeated, see Fig. 3.33 for the tension measurements before and after the mesh cut.

3.6.12 High voltage test

The high voltage test is essential for the good operation of the MicroMegas detector. All metallic parts (except the cathodes) must be properly grounded, and a good electrical continuity must be ensured among them. These parts are: the honeycomb sheets inside the panels (to be grounded in the gluing phase adding ground spiders), the gas distribution pipes, all aluminum frames and all corners. When a drift panel is completely finalized, the test is performed applying an HV of 500 V on the cathode plane of the drift panel,

3.6. DRIFT PANEL FINALIZATION

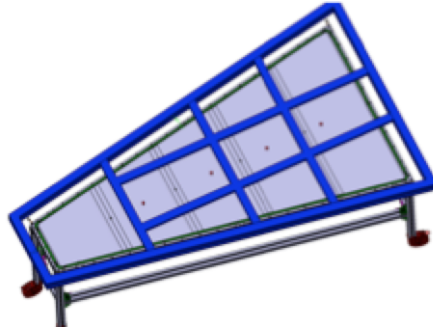


Figure 3.32: Drawing of the mesh gluing on drift panel: the transfer frame is placed on top of the finalization-table aligning the mesh with the drift panel. Technical designed by Antonio Zullo.

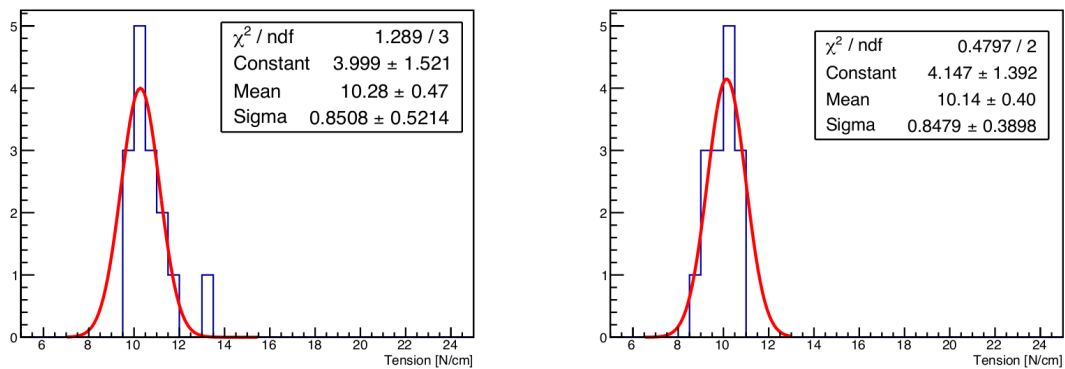


Figure 3.33: Tension of mesh glued on a drift panel, before (left) and after (right) the cut from the transfer frame. The tension measurement is done with an apposito tensiometer.

3.6. DRIFT PANEL FINALIZATION

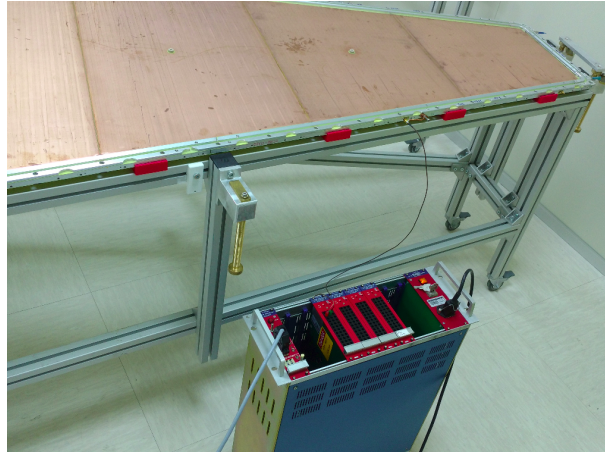


Figure 3.34: High voltage test on a drift panel.

while the mesh is grounded and the current is monitored for about 30 minutes (see Fig. 3.34). The QA/QC test is successfully passed if the current is under 5 nA.

3.6.13 Drift panel finalization work flow

The drift panel finalization procedure has been optimized to complete 2 external and 1 central drift panels per week, working in parallel on two distinct sets: the bare panels and panel ready for the mesh gluing. The highlights of the work flow, for the two distinct set of drift panels, are reported here:

First day: bare drift panels An external drift panel and a central one are disposed on two distinct finalization-tables. They are cleaned from the glue residuals and the FR4 borders chamfered, then the both sides of panels are accurately cleaned with propanol and the holes corresponding to the positions of the mesh-frames, gas distribution pipes and interconnection drift spacers are tested for gas tightness. The leaking holes must be recovered using Araldite 2011. After this inspection, the interconnection drift spacers and HV connectors are glued on the drift panels. Moreover, the PCB-PCB junctions are sealed with Araldite 2011. In this section, to better explain the work-flow, the side of the

3.6. DRIFT PANEL FINALIZATION

central panel in which all the operations have been performed is called “side-A”.

First day: ready drift panels Two meshes are washed in the washing cabin and transferred into the clean room for drying.

Second day: bare drift panels The glue used for PCB-PCB sealing in the region of O-Ring groove and mesh-frame is smoothed using abrasive paper in alcohol, then the sealing tested with the local gas tightness, the interconnection drift spacers height is measured as well as their gas tightness and the five cathodes electrically connected one to each other. Then the external drift panel is parked momentarily on the transport cart and the other external panels placed on the finalization-table. The central one is turned upside down and placed on the same table. On the new outer drift panel starts the same operations performed the first day on the first external panel. Instead for the central one side-B start only the operations of gluing and sealing.

Second day: ready drift panels The washed meshes are glued on an external drift panel and on the side A of a central “ready” panel. The other two meshes are washed in the washing cabin and soon after transferred into the clean room for drying.

Third day: bare drift panels The glue used for PCB-PCB sealing in the region of O-Ring groove and mesh-frame is smoothed using abrasive paper in alcohol, then the sealing tested for gas tightness, the interconnection drift spacers height measured as well as their gas tightness and the five cathodes electrically connected one to each other. At this stage the three panels are ready for mesh-frame and gas pipe gluing. This gluing starts on the two panel sited on the finalization-tables.

Third day: ready drift panels The glued meshes are separated from the transfer frame, cleaned and the HV test performed. At the end of the HV test the outer panel is stuffed and put on a transport cart. The free table is occupied with the other outer panel and the central one turned

3.7. PRODUCTION STATUS

upside down and placed on the same table. The two panels cleaned and the two meshes glued.

Fourth day: bare drift panels The mesh-frame height is measured and the panels are cleaned before starting the gluing of the mesh-frames on the second pair of cathodes (one external and the other side of the central).

Fourth day: ready drift panels The glued meshes are separated from the transfer frame, cleaned and the HV test performed. The external and central drift panels are put on a transport cart, to be transferred in the other clean room for the quadruplet assembly.

Fifth day: bare drift panels The mesh-frame height is measured and the panels cleaned again. The gas tightness test of the three panels starts. In the same day the electrical tests are performed.

3.7 Production status

The mass production of the NSW MicroMegas quadruplets have started in June 2017. Here a short summary of the production status at November 2017:

- 2 *eta* and 1 stereo readout panels have been constructed in Pavia. The number of completed panels is small because, due to problems on the quality of the first readout-boards delivery, the construction of readout panels is started only recently.
- At Roma1 a total of 21 bare drift panels have been constructed: 7 central panels and 14 external panels, corresponding to 7 quadruplets.
- At Roma3 23 meshes have been stretched.
- At LNF a total of 14 drift panels have been finalized and ready for the assembly: 4 central and 10 external drift panels. The finalization procedures and quality control tests are quickly reaching the optimum in terms of quality, rapidity, affordability and safety.

3.7. *PRODUCTION STATUS*

- At LNF 1 SM1 MicroMegas doublet has been closed. No quadruplets are assembled.

During each construction phase of the SM1 MicroMegas quadruplets, all the items, the transports and the test results are registred and traceable by apposite online Logistic and QA/QC databases.

CHAPTER 4

Lepton-Jets search

The aim of this thesis is describing an analysis as much as possible model independent, therefore a general structure of Hidden Sector and a generic definition of Lepton-Jets (LJs) are used. In addition, only LJs produced far from the primary interaction vertex are considered.[77][78]

This situation represents a challenge both to reconstruction and trigger ATLAS capabilities for two reasons: (i) due to the detector granularity, it is not simple to distinguish collimated particles as LJs, (ii) due to the displaced LJ vertex, it is not possible to use the inner tracking system nor to apply triggers which require tracks pointing back to the interaction point.[79]

4.1 Hidden Sector and Lepton-Jets

As already suggested in chapter 1, several Standard Model extensions predict the existence of a *Hidden Sector* weakly coupled to the Standard Model, in which new heavy particles, or even H, W, Z, t particles, may decay into.[80][81][82][83][80][84]

In this thesis, to trigger non-conventional Higgs decays, it is considered the simplest case in which the Hidden Sector is a non abelian gauge group $U(1)_d$, whose symmetry is broken at the GeV scale, and the associated hidden gauge boson, usually called hidden photon or **dark photon** γ_d , mixes kinetically with the visible one.[13] The most general Lagrangian describing

4.1. HIDDEN SECTOR AND LEPTON-JETS

the *vector*¹ portal between the hidden gauge $U(1)_d$ field and the SM $U(1)$ field is:

$$\mathcal{L} = -\frac{1}{4}F_{\mu\nu}F^{\mu\nu} - \frac{1}{4}b_{\mu\nu}b^{\mu\nu} + \frac{\epsilon}{2}b_{\mu\nu}F^{\mu\nu} + \frac{m_{\gamma_d}^2}{2}b_\mu b^\mu \quad (4.1)$$

where $F_{\mu\nu}$ is the field strength for SM photon, $b_{\mu\nu}$ is the field strength for γ_d and ϵ is the **kinetic mixing** parameter.[85]

Through the vector portal, the γ_d decays into all kinematically allowed SM states with electric charge. Therefore, as shown in the Fig. 4.1, the mass of γ_d is the only parameter controlling which visible particles can be produced: if γ_d mass is in the range of MeV to GeV, it will decay mainly in leptons and light hadrons. In addition, due to its small mass, the γ_d would typically be produced with large boosts at LHC, thus the result of its decay consists of *collimated jet-like structures* containing pairs of electrons, muons or charged pions, called **Lepton-Jets**². [79]

An important role for the Hidden Sector is covered by the kinetic mixing parameter ϵ , which controls the coupling strength of the Hidden Sector and the SM one, and also determines the γ_d lifetime τ ³. An approximate mathematical relationship between ϵ and τ is:[86][87]

$$c\tau \propto \left(\frac{10^{-4}}{\epsilon}\right)^2 \left(\frac{100\text{MeV}}{m_{\gamma_d}}\right)^2 \quad (4.2)$$

Typically the kinetic mixing parameter ϵ is of the size of radiative correction $\sim \mathcal{O}(10^{-5} - 10^{-2})$. In this thesis it is considered the case of $\epsilon \leq 10^{-5}$, which means that the γ_d with mass in the range of MeV to GeV has non-negligible lifetime, and its decay length is comparable with the ATLAS detector dimensions. This turns up in LJs produced far for the interaction point, usually called **displaced Lepton-Jets** (dLJs).[88][70][89]

¹A vector boson has odd intrinsic parity and spin=1, therefore each gauge boson is also a vector boson.

²As clearly reported in [13], the decay branching ratio (BR) of the γ_d into pions depends on the electromagnetic form-factor at $\rho^2 = m_{\gamma_d}^2$, also known as R ratio. If the γ_d mass is very close to the ρ -meson resonance, it decays mostly into pions (see Fig. 4.1), and the term Lepton-Jet is not very suitable. However, generally, a big fraction of BR into leptons is expected and this is the reason of the name.

³From now on, in this thesis the γ_d lifetime τ will be expressed as τ times the speed of light c , i.e. $c\tau$.

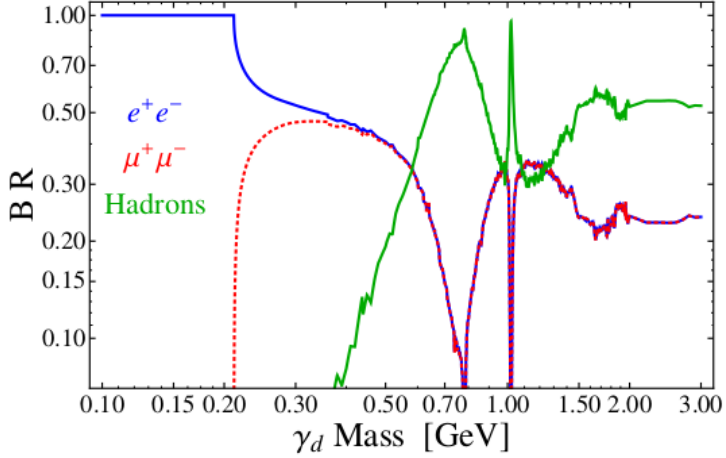


Figure 4.1: γ_d particle branching ratio as a function of its mass. For $m_{\gamma_d} \sim 0.4$ GeV the $BR(\gamma_d \rightarrow e^+e^-)$ and $BR(\gamma_d \rightarrow \mu^+\mu^-)$ are 45%, while $BR(\gamma_d \rightarrow \pi^+\pi^-)$ is 10%.^[83]

Therefore, experimentally the LJs are characterized by the high energetic particles (e , μ , π) highly collimated ($\Delta R \leq 0.1$) created far away from the interaction point, from the decay of one or two dark photons, as displayed in Fig. 4.2.

The introduction of the Hidden Sector can solve some SM limitations described in chapter 1.^[90] For example, assuming that Dark Matter (DM) is charged under the Hidden Sector ($U(1)_d \equiv G_d$), the astrophysical anomalies observed by FERMI and PAMELA telescopes (i.e. the excess of positron flux but not of antiproton flux) are explained by the fact that, for kinematic reasons, dark photons decay into leptons. Also the high cross section observed can be explained taking into account the Sommerfeld enhancement of the annihilation rate. In addition, the existence of a Hidden Sector provides a solution to the muon anomalous magnetic moment by the introduction of a correction term due to a virtual dark photon.^{[91][92]}

4.2 The FRVZ benchmark models

This thesis only considers non-conventional Higgs decays, which correspond to the branching ratio $BR(H \rightarrow LJs) = 10\%$. The Higgs boson is

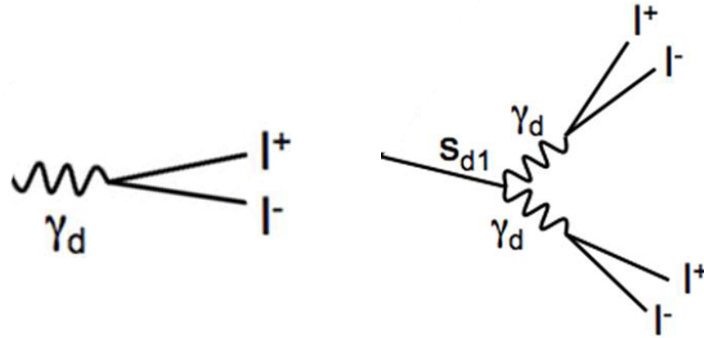


Figure 4.2: Picture showing two generic LJs: on the left a LJ is produced by the decay of one γ_d , while on the right is produced by the decay of one hidden scalar s_{d1} into two γ_d .[\[77\]](#)

generated through the *gluon-gluon fusion production* mechanism, which has a cross section in proton-proton collisions at $\sqrt{s} = 13$ TeV, of $\sigma = 44.13$ pb for $H = 125.09$ GeV.[\[93\]](#)

In order to use a generic definition of dLJ, this analysis uses as *benchmark models*, two simplified Falkowsky-Ruderman-Volansky-Zupan (FRVZ) models.[\[77\]](#) As shown in Fig. 4.3, both FRVZ models assume that a SM Higgs boson (or even a Higgs-like heavy scalar boson) decays to a pair of **hidden fermions** f_{d2} yielding a decay-chain, which finally produces a pair of dLJs. In the first benchmark model, see Fig. 4.3a, each hidden fermion f_{d2} decays to a γ_d and a **Hidden Lightest Stable Particle** (HLSP), and each γ_d produces a dLJ. In the second benchmark model, see Fig. 4.3b, each f_{d2} decays to a HLSP and a **hidden scalar** s_{d1} which in turn decays to pairs of γ_d , and each pair of γ_d yields a dLJ.

In both the FRVZ models, the two dLJs produced from the γ_d decays, are approximately back-to-back and consist of collimated particles ($\Delta R < 0.1$). The dark photon mass is chosen 0.4 GeV, therefore as shown in Fig. 4.1, both $\text{BR}(\gamma_d \rightarrow e^+e^-)$ and $\text{BR}(\gamma_d \rightarrow \mu^+\mu^-)$ are 45%, while $\text{BR}(\gamma_d \rightarrow \pi^+\pi^-)$ is 10%. Finally, the mean lifetime $c\tau$ of the γ_d is a free parameter of the benchmark models.

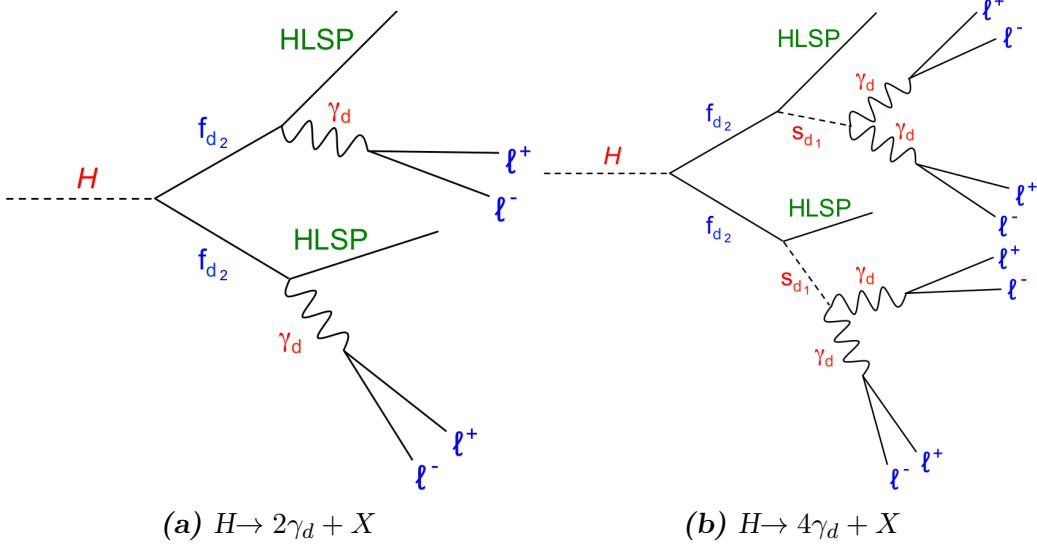


Figure 4.3: The FRVZ benchmark models: the diagrams show the production of hidden fermions and their decay-chain in the hidden sector yielding two dLJs. H is the Higgs boson or a Higgs-like heavy scalar boson produced via gluon-gluon fusion.[70]

4.3 Monte Carlo and data samples

This section briefly describes the samples of events used in this analysis. For a complete list of all Monte Carlo and data samples see [94].

4.3.1 Collision data sample

The analysis presented in this thesis employs the full dataset collected by ATLAS during the 2015 data taking⁴ at $\sqrt{s} = 13$ TeV, corresponding to an integrated luminosity of 3.5 fb^{-1} . Although the integrated luminosity of 2015 is relatively low, the sensitivity to displaced LJ signatures is sizeable due the high cross-section for Higgs production at $\sqrt{s} = 13$ TeV, and also

⁴As recommended by the ATLAS Data Quality group, only runs contained in the Good Run List (GRL) are used. The GRL consists of all the physics runs which satisfy a set of data quality criteria, and for which all the ATLAS subdetectors runned at the nominal conditions. In this analysis the GRL data15 13TeV.periodAllYear HEAD DQDefects-00-01-02 PHYS StandardGRL All Good 25ns tolerable IBLSTANDBY-DISABLE.xml is used.

4.3. MONTE CARLO AND DATA SAMPLES

FRVZ model	m_H [GeV]	m_{fd_2} [GeV]	m_{HLSP} [GeV]	m_{sd_1} [GeV]	m_{γ_d} [GeV]	$c\tau_{\gamma_d}$ [mm]
$H \rightarrow 2\gamma_d + X$	125	5.0	2.0		0.4	47.0
$H \rightarrow 4\gamma_d + X$	125	5.0	2.0	2.0	0.4	82.40
$H \rightarrow 2\gamma_d + X$	800	5.0	2.0		0.4	11.76
$H \rightarrow 4\gamma_d + X$	800	5.0	2.0	2.0	0.4	21.04

Table 4.1: Parameters used for Monte Carlo simulation of the two benchmark models. As reported, the first and third rows refer to the first FRVZ model with SM Higgs boson and heavy Higgs-like boson respectively. The second and fourth rows refer to the second FRVZ model using SM Higgs and heavy Higgs-like boson respectively. For all Monte Carlo simulations $BR(\gamma_d \rightarrow e^+e^-) = BR(\gamma_d \rightarrow \mu^+\mu^-) = 45\%$, and $BR(\gamma_d \rightarrow \pi^+\pi^-) = 10\%$.

to improvements both in trigger and reconstruction efficiency for close-by muons.

4.3.2 Monte Carlo signal sample

As said in Sec. 4.2, the Higgs boson seeding the Hidden Sector chain-decay, is generated through the gluon–gluon fusion production mechanism. The PYTHIA8 generator⁵ v8.186 is used, linked together with a custom model in MadGraph 5⁶ v2.2.3, for gluon-gluon fusion production of the Higgs boson and the subsequent decay to Hidden Sector particles. The generated Monte Carlo (MC) events are processed through the full ATLAS simulation chain based on GEANT4⁷ and then reconstructed using the same software release used for collision data.[77]

⁵PYTHIA8 is a computer simulator program for the generation of high-energy collisions, written in C++. It contains a set of physics models for the evolution from a few-body hard process to a complex multihadronic final state.[95]

⁶MadGraph 5 is a matrix element generator written in the Phyton programming language. It can generate the matrix element at the tree-level for any Lagrangian based model (renormalizable or effective). The results can be output as a set of C++ classes and linked to PYTHIA8.[96]

⁷GEANT4 is a toolkit for the simulation of the passage of particles through matter and for full MC simulation of detectors in High Energy Physics. It is also designed to take into account the requirements of space and cosmic ray applications, nuclear, heavy ions and radiation computations, and medical applications.[97]

4.3. MONTE CARLO AND DATA SAMPLES

For each benchmark model, two sets of MC events have been simulated. Both have the same decay chain, but the first MC set uses the 125 GeV Higgs boson, while the second one uses an 800 GeV Higgs-like scalar boson. The γ_d mean lifetime $c\tau$ is a free parameter of FRVZ models. Therefore, in the generated MC signal samples, $c\tau$ is chosen so that a large amount of decays occurs inside the sensitive ATLAS detector volume, i.e. before the first muon trigger chamber (up to 7 m in radius and 13 m along the z -axis). As will be discussed in Sec. 6.2, it is possible to calculate the γ_d detection efficiency for a wide range of $c\tau$, through reweighting of the decay position in the generated samples. A detailed view of all the parameters used in the generated MC signal samples is reported in Tab. 4.1.

In order to compare the MC to data results, the number of MC events is normalized to that expected at the integrated luminosity of 2015 data (3.5 fb^{-1}). Hence, the total number of MC events is rescaled to the production cross-section of the sample processed multiplied by the integrated luminosity.

In particular, for the 125 GeV Higgs boson the cross section is 44.13 pb (which is the SM gluon fusion Higgs production cross section), while for the 800 GeV Higgs-like boson the cross section is fixed to the conventional value of 1.0 pb (to easy rescale to any other cross sections).

4.3.3 Empty data samples

In order to study the non-collision background from cosmic-rays and Beam-Induced Background, it is used a sample of events collected in the empty bunch-crossings⁸ with the same triggers applied on data, but with an high prescale factor ($\simeq 50$). The average ratio between filled and empty bunch crossings is almost 2 to 1.

4.3.4 Monte Carlo background samples

In order to study the SM background produced by proton-proton collisions, this analysis uses official ATLAS MC samples corresponding to the fol-

⁸Empty bunch-crossings contain no protons.

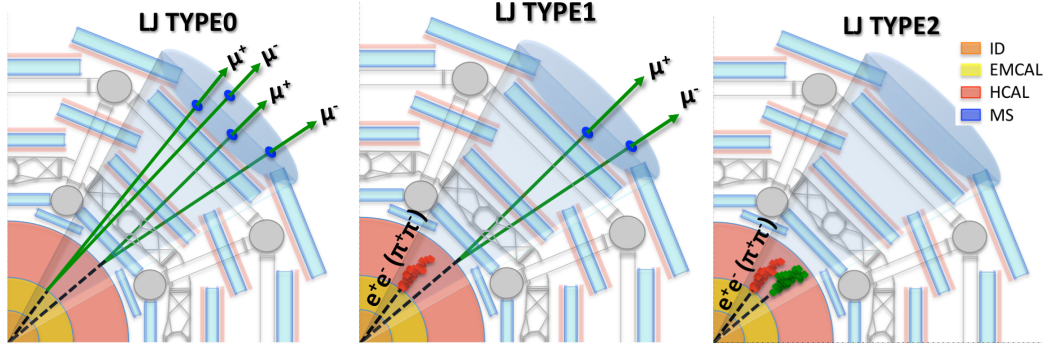


Figure 4.4: Classification of dLJs based on particle species content.[78]

lowing processes: $t\bar{t}$, single-top, di-photon, photon+jets, Drell-Yan $e^+e^- (\mu^+\mu^-)$, Z +jets, W +jets, ZZ , WW , WZ .

As for the MC signal sample, also the MC background events are processed through the full ATLAS simulation and reconstruction chain. Moreover, also for the MC background samples, the total number of events is rescaled to the production cross-section of the sample processed multiplied by the total integrated luminosity in the 2015 data sample.

4.4 LJ reconstruction

As shown in Fig. 4.4, this analysis classifies LJs according to the final state particles content, which depends on the γ_d decay chain:

- **LJ Type0:** a cluster of at least two muons identified into the Muon Spectrometer, with a veto on jets in a cone of radius $\Delta R = 0.5$. It corresponds to the signature of a LJ with at least one $\gamma_d \rightarrow \mu^+\mu^-$.
- **LJ Type1:** a cluster of at least one jet with low electromagnetic (EM) fraction⁹, and two muons in a cone of radius $\Delta R = 0.5$. It corresponds to the signature of a LJ with two γ_d : one $\gamma_d \rightarrow \mu^+\mu^-$ and the other $\gamma_d \rightarrow \pi^+\pi^- (e^+e^-)$.

⁹As will be explained later, the EM fraction is defined as the ratio of the energy deposited in the ECal, with respect to the total jet energy.

4.4. LJ RECONSTRUCTION

- **LJ Type2:** a jet with low EM fraction and no muons in a cone of radius $\Delta R = 0.5$. It corresponds to the signature of a LJ with at least one $\gamma_d \rightarrow \pi^+\pi^-(e^+e^-)$.

For all LJ topologies this work only considers γ_d *displaced decays*. In this way it is possible to reduce the SM background rejecting particles coming from the main proton-proton interaction vertex.

For muonic LJs, this requirement means that only dark photons decay beyond the last Pixel detector layer ($\simeq 12$ cm along x-y plane, $\simeq 50$ cm along z-direction) are considered. Since the ID reconstruction algorithm requires at least one hit in Pixel detector, muons constituting dLJs are reconstructed only by MS and they are not lined up to any ID tracks. Therefore, at detector level, the muonic dLJs consists of **non-combined** (non-CB) muons, which are defined as an *ExtrapolatedMuonTrackParticle* objects (i.e. MS tracks with a loose constraint on the main vertex position) not matched to any combined muons (which are muons with a MS track lined up to an ID track).

The non-CB muons are selected applying the following requirements, suggested by the Muon Performance Group:

- In the barrel region are accepted non-CB tracks with hits in at least two¹⁰ MDT stations (total number of hits ≥ 10), and at least 1 RPC ϕ -hit.
- In the EC region are accepted non-CB tracks with at least 1 hit in the TGC stations, and at least one of the following cases:
 - number of hits ≥ 10 in the MDT stations
 - number of hits ≥ 3 both in CSC chambers and in the middle+outer MDT stations.

In addition to the listed requirements, the search is limited to the pseudorapidity interval $|\eta| < 2.4$, which corresponds to the ID and MS trigger

¹⁰Actually, the Muon Performance Group requires three MDT stations. In this work the minimum number of MDT stations is reduced in order to accept γ_d decays occurred between the first MDT layer and the first trigger chamber, corresponding to the range of radius $\simeq 5 - 7$ m

4.4. LJ RECONSTRUCTION

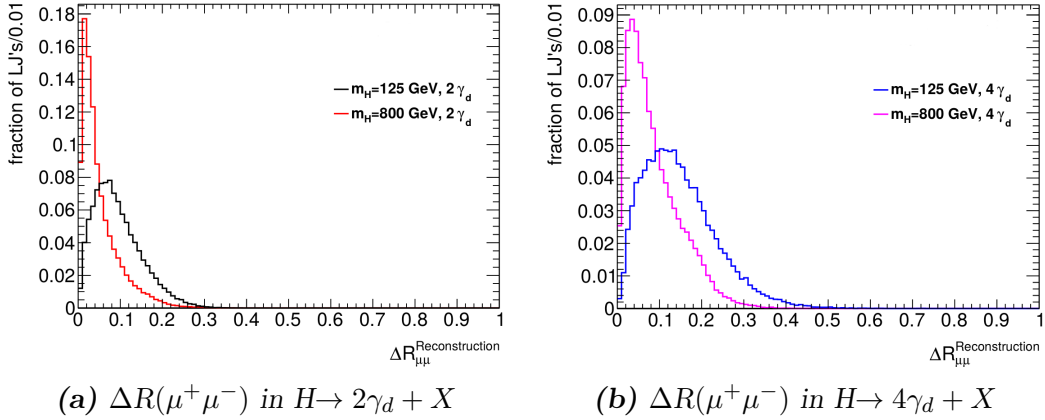


Figure 4.5: Angular opening of γ_d decay products for muonic LJs. Fig. 4.5a shows the ΔR distribution between muons of a single LJ for the FRVZ model $H \rightarrow 2\gamma_d + X$, while Fig. 4.5b shows the same distribution for the FRVZ model $H \rightarrow 4\gamma_d + X$. Both 125 GeV Higgs boson and 800 GeV Higgs-like heavy scalar boson are considered.[94]

coverage. Moreover, in order to avoid the MS transition region where the magnetic field is not uniform, tracks in the range $1.0 < |\eta| < 1.1$ are rejected. For muonic LJs, the algorithm reconstruction is seeded by the highest p_T non-CB muon, and searches for non-CB muons in a cone of fixed opening angular ΔR . If at least 2 muons and no jets are found, the LJ is accepted and classified as LJ Type0. As reported in Fig. 4.5, a cone of $\Delta R = 0.5$ is adequate to contain all the dark photons decay products for both the FRVZ models, with 125 GeV Higgs boson and 800 GeV Higgs-like heavy scalar boson.[94]

In the case in which the γ_d decay products are electrons or pions pairs, the algorithm used for jet clusterization is the “anti- k_t algorithm”, with a radius parameter of 0.4.¹¹

¹¹The anti- k_t algorithm consists of iterative process that combines pairs of i,j clusters, contained in a fixed radius R , in order to minimize the quantity:

$$d_{ij} = \min(p_{T,i}^{2n}, p_{T,j}^{2n}) \frac{\Delta R_{ij}^2}{R^2}$$

where R and n are free parameters, which are chosen for the anti- k_t algorithm as $n = 1$ and $R = 0.4$. The advantage of the anti- k_t algorithm is that it leads to the reconstruction of jets with shapes not influenced by soft or strong perpendicular radiation. Other jet

4.4. LJ RECONSTRUCTION

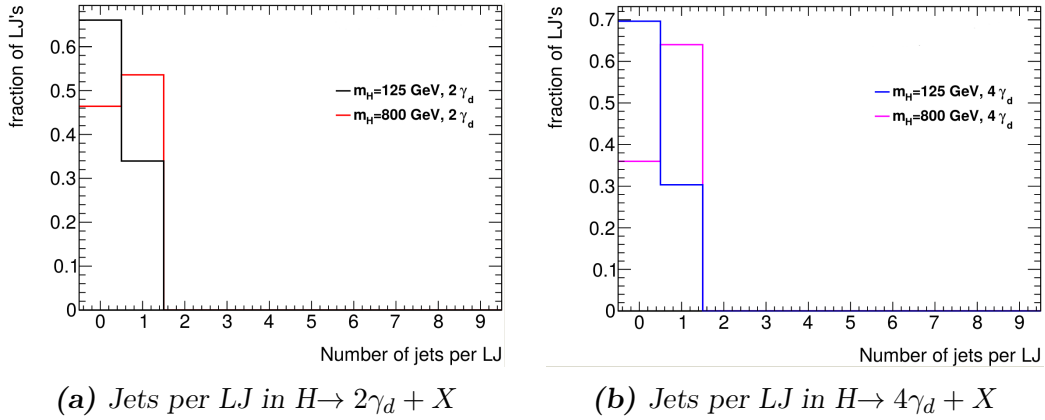


Figure 4.6: Fraction of reconstructed jets contained in a LJ for the two FRVZ models. In particular, Fig. 4.6a corresponds to the model $H \rightarrow 2\gamma_d + X$ in which each LJ is generated by one dark photon decay, while Fig. 4.6b corresponds to the model $H \rightarrow 4\gamma_d + X$ in which each LJ is generated by two dark photons decay. Both distributions are evaluated using 125 GeV Higgs boson and 800 GeV Higgs-like heavy scalar boson.[94]

This analysis only considers jets with $p_T \geq 20 \text{ GeV}$ and $|\eta| \leq 2.4$. In addition, jets must satisfy the standard ATLAS quality criteria reported in [98], while for calibration are used the recommended recipe for Moriond 2016 (JetCalibTools-00-04-61) and the energy scale correction described in [99]. The only standard ATLAS selection criteria not applied is the requirement on the electromagnetic fraction, which is defined as the ratio of the energy deposited in the ECal with respect to the total jet energy. In this way, γ_d displaced decays in the HCal are allowed in the search. In fact as will be described in Sec. 4.7 and 4.8, in order to reduce the background for electrons or pions LJ, only dark photons decay in HCal, or at the end of ECal, are selected.

As shown in Fig. 4.6, for the two FRVZ models, each LJ constituted by electrons or pions is mostly reconstructed as a single jet, regardless of whether it is generated by one or two dark photons decay. This is due to the large γ_d boost which leads to very collimated particles.

clustering algorithm are “k_t”, and “Cambridge/Aachen” algorithm which use a different value of free parameter n .

4.5 Triggers for LJ selection

Since many standard ATLAS triggers are strictly linked to the primary IP, in order to select γ_d displaced decays it is necessary to use specifically designed triggers, which are not linked to the primary vertex.[100]

In particular, this analysis takes advantage of a logical OR of the following triggers:

- The **Narrow-Scan** “HLT-mu20-msonly-mu6noL1-msonly-nscan05”, is designed to select events with two muons in a very narrow cone, avoiding the loss of efficiency due to the limited granularity of RoI at L1 trigger (see Sec. 2.3.7). In fact, the Narrow-Scan trigger requires at least one L1 trigger muon with $p_T \geq 20$ GeV (which is fully matched with a HLT muon object). Then, around this “leading muon”, the trigger performs a scan in a cone of $\Delta R = 0.5$, searching for a “sub-leading muon”. The sub-leading muon is a HLT muon with $p_T \geq 6$ GeV, which has no requirements on matching a L1 muon object. It is important underline that the Narrow-Scan does not require an ID track either for leading muon or for sub-leading one.
- The **Tri-muon MS-only** “HLT-3mu6-MSonly”, selects events with at least three MS-only muons with $p_T \geq 6$ GeV.[101] It is seeded at L1 trigger by a cluster of three muon ROIs in a cone of $\Delta R = 0.4$. Moreover it requires to have no reconstructed jets in a cone of $\Delta R = 0.5$.
- The **CalRatio** “HLT-j30-jes-PS-llp-L1-TAU60” selects events with an isolated jet of low EM fraction.[101] Since the γ_d decay in the HCal produces narrow jets, the CalRatio trigger is seeded by a L1 τ -lepton trigger with $p_T \geq 60$ GeV, which uses a narrower calorimeter region than the L1 jet trigger. The CalRatio requires jets with $E_T \geq 30$ GeV and $|\eta| \leq 2.4$ (which is the pseudorapidity ID coverage, useful to reject jets lined up with ID tracks). Moreover, regarding the calorimeter energy ratio it is required that $\log\left(\frac{E_{HCal}}{E_{ECal}}\right) \geq 1.2$. Finally, in order to reject fake jets from beam-halo muons, the CalRatio performs ID

4.6. FRVZ LJ RECONSTRUCTION EFFICIENCY

FRVZ model	Trigger	Efficiency (%)	Efficiency (%)
		$m_H = 125$ GeV	$m_H = 800$ GeV
$H \rightarrow 2\gamma_d + X$	Narrow-Scan	10.6	23.0
	Tri-muon MS-only	2.0	2.4
	CalRatio	0.3	9.7
	OR of all triggers	11.9	32.0
$H \rightarrow 2\gamma_d + X$	Narrow-Scan	8.3	38.4
	Tri-muon MS-only	4.9	7.8
	CalRatio	0.1	7.4
	OR of all triggers	11.8	44.8

Table 4.2: Trigger acceptance times efficiency (in %) calculated using the generated FRVZ MC samples. Both FRVZ models with 125 GeV Higgs boson and 800 GeV Higgs-like scalar boson are used.[77][102]

track isolation selection around the jet axis (no track with $p_T \geq 2$ GeV within $\Delta R \leq 0.2$ from the jet axis) and Beam Induced Background tagging (see Sec. 4.8 for further informations).

Tab. 4.2 shows for each trigger, the acceptance times efficiency¹² evaluated for the two FRVZ benchmark models $H \rightarrow 2\gamma_d + X$ and $H \rightarrow 4\gamma_d + X$. It is defined as the ratio between the number of triggered events and the total number of FRVZ MC generated ones.

4.6 FRVZ LJ reconstruction efficiency

The reconstruction efficiency¹³ is evaluated for LJ Type0 and LJ Type2 using the FRVZ MC signal samples of the benchmark model $H \rightarrow 2\gamma_d + X$ with 125 GeV and 800 GeV Higgs boson. The corresponding detection efficiency for the LJ Type1 can be evaluated simply multiplying the LJ Type0 detection efficiency and the standard jet one.[78]

¹²Note that in HEP, the acceptance refers to purely geometric detector fiduciality, while the efficiency refers to purely detector effectiveness in finding objects which pass through the detector. Usually, the quantity acceptance times efficiency is simply indicated as “efficiency”.

¹³As before, “efficiency” is understood to mean acceptance times efficiency.

4.6. FRVZ LJ RECONSTRUCTION EFFICIENCY

For both LJ Type0 and LJ Type2, the dark photon reconstruction efficiency is evaluated separately for the Barrel and the EC regions, and it is given as a function of p_T and decay distance of γ_d . In particular, in the Barrel region it is used the transverse decay distance L_{xy} , while in the EC region the longitudinal decay distance L_z . [103][24]

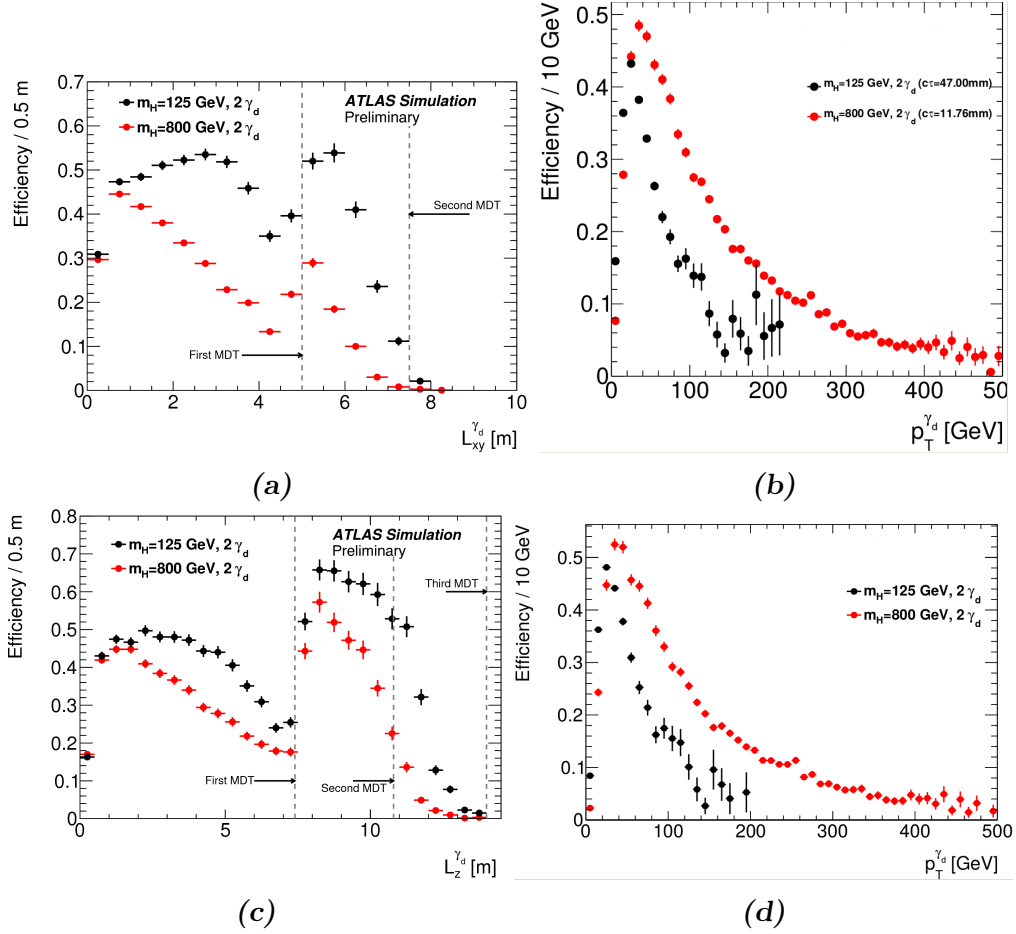


Figure 4.7: Reconstruction efficiency for LJ Type0 from $\gamma_d \rightarrow \mu^+ \mu^-$ evaluated with MS samples of model $H \rightarrow 2\gamma_d + X$. Both 125 GeV and 800 GeV Higgs bosons are used. First row shows the reconstruction efficiency evaluated in the Barrel region, while the second one the corresponding value for the End-Cap region: Fig. 4.7a displays the efficiency as a function of the γ_d transverse decay distance L_{xy} , Fig. 4.7b as a function of the γ_d p_T , Fig. 4.7c as a function of the γ_d longitudinal decay distance L_z , and finally, Fig. 4.7d as a function of p_T . [102][94]

4.6. FRVZ LJ RECONSTRUCTION EFFICIENCY

For LJ Type0, the γ_d reconstruction efficiency as a function of a given variable, it is defined as the ratio (for each variable's bin) between the number of $\gamma_d \rightarrow \mu^+\mu^-$ reconstructed as LJs, and the total generated $\gamma_d \rightarrow \mu^+\mu^-$, without applying trigger cuts. As shown in Fig. 4.7, both for the Barrel ($|\eta| \leq 0.9$) and the EC regions ($|\eta| \geq 1.1$), the reconstruction efficiency decreases with increasing the γ_d decay distance from the interaction point. This is due to the decrease in separation between the two muons in the inner MDT station (since they are produced farther from the IP, they are more collimated producing an overlap in the track reconstruction). Moreover, there is an increase in reconstruction efficiency as a function of the decay distance, after the innermost chambers ($L_{xy} \simeq 4.5$ m, $L_z \simeq 7.5$ m in the EC) due to the separation of the two muons under the influence of the MS magnetic field (see Fig. 4.7). Finally, as expected, the reconstruction efficiency drops to zero respectively after the second MDT station in the Barrel, and after the third MDT station in the EC.

Fig. 4.7 also shows that the $\gamma_d \rightarrow \mu^+\mu^-$ reconstruction efficiency for the 800 GeV Higgs boson sample, is lower than the one evaluated with the 125 GeV Higgs boson. This is due to the higher boost of γ_d produced from 800 GeV Higgs-like heavy scalar boson, which induce a decrease of muons track separation.

The same procedure used for LJ Type0, it is repeated for LJ Type2 in which the $\gamma_d \rightarrow e^+e^-(\pi^+\pi^-)$ is reconstructed as jet. In fact, also in this case, the γ_d reconstruction efficiency as a function of a given variable, is defined as the ratio between the number of $\gamma_d \rightarrow e^+e^-(\pi^+\pi^-)$ reconstructed as LJs and the total number of $\gamma_d \rightarrow e^+e^-(\pi^+\pi^-)$. This ratio is evaluated for each variable's bin, separately for the Barrel ($|\eta| \leq 1.1$) and End-Cap ($|\eta| \geq 1.1$) regions, without applying any trigger cuts. However, in order to select LJs Type2 produced in HCal (or late in ECal) a cut on the electromagnetic fraction and on the jet width are applied.¹⁴ For this reason, as shown in Fig. 4.8, the reconstruction efficiency becomes significantly different from zero at

¹⁴In particular, it is required that the EM fraction ≤ 0.1 and the jet width $W \leq 0.058$. Sec. 4.8 extensively explains the definition of mentioned cuts.

the end of the ECal ($L_{xy} \simeq 2$ m, $L_z \sim 4$ m) and drops to zero at the end of HCal ($L_{xy} \simeq 3.7$ m, $L_z \simeq 6$ m).

Contrary to the LJ Type0 case, the reconstruction efficiency of $\gamma_d \rightarrow e^+e^-(\pi^+\pi^-)$ evaluated using the 800 GeV Higgs boson is higher than the corresponding one evaluated using the 125 GeV Higgs boson. This is due to the fact that the LJs produced from 800 GeV Higgs boson have higher p_T and hence are more easily reconstructed in ATLAS as a jets.

4.7 Main source of background

The main sources of background for the LJ signal are:

- Quantum ChromoDinamics (QCD) multijet production,
- Beam-Induced Background (BIB),
- cosmic-ray muons.

The **Quantum ChromoDinamics multijet** production consists of SM high-energy jets produced by the proton-proton interaction. The multijet production constitutes the main background to the LJ Type2 signal. Although the multijet production is the main SM background component, **other standard processes** due to proton-proton collision can be background sources for the LJs search. For example the SM processes which lead to prompt muons and muons plus jet in the final state, like: single-top, $t\bar{t}$, di-photon, photon+jet, Drell-Yan $e^+e^-(\mu^+\mu^-)$, Z+jets, W+jets, ZZ, WW, WZ. In these cases, as will be discussed in next section, the selection of γ_d displaced decays provides a good SM jets rejection.

Moreover, another source of background comes from SM processes with high production rate of secondary muons not matched to the primary vertex. For example the decays in flight of K/π and heavy flavour decays in multi-jet processes.

The **Beam-Induced Background** is produced mostly by interaction of protons with residual gas or machine elements.[104][105] In fact, the main BIB sources are:

4.7. MAIN SOURCE OF BACKGROUND

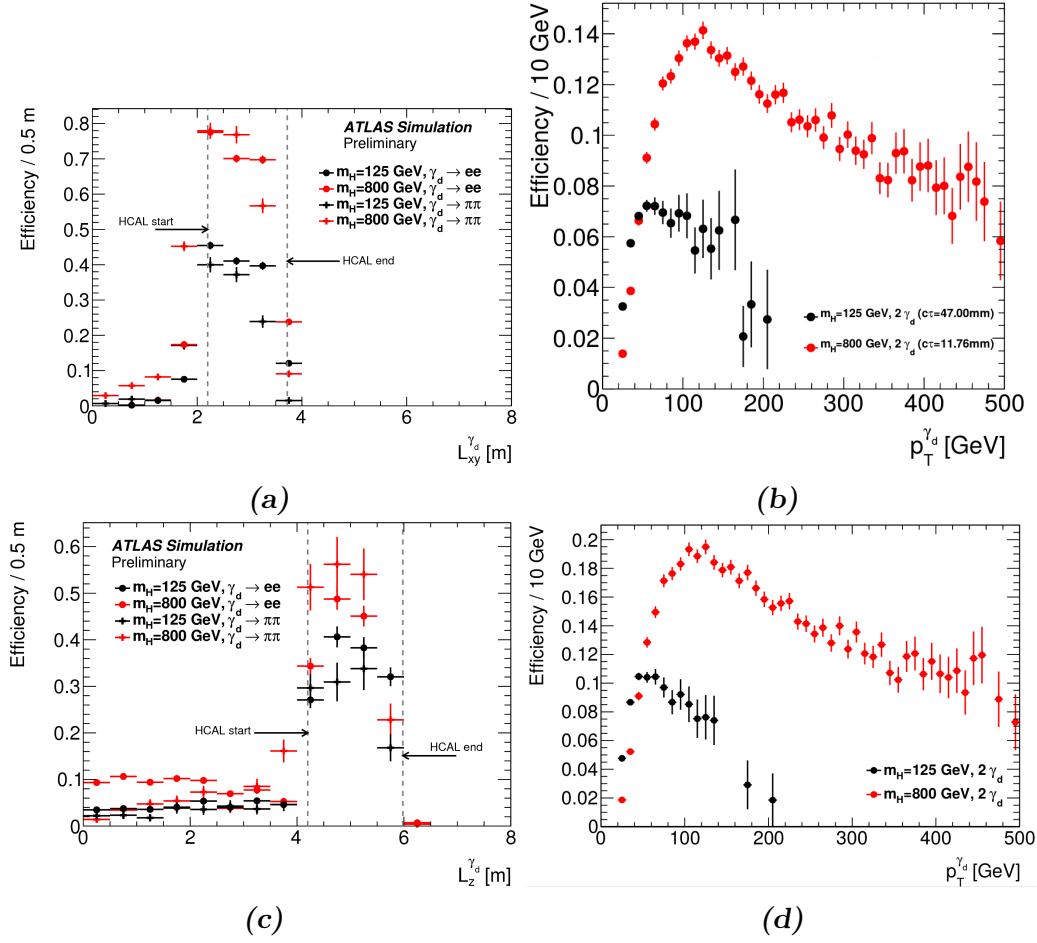


Figure 4.8: Reconstruction efficiency for LJ Type2 from $\gamma_d \rightarrow e^+e^-(\pi^+\pi^+)$ evaluated with MC samples of model $H \rightarrow 2\gamma_d + X$. Both 125 GeV and 800 GeV Higgs bosons are used. First row refers to the reconstruction efficiency evaluated in the Barrel region, while the second one to the corresponding value for the End-Cap region: Fig. 4.8a displays the efficiency as a function of the γ_d transverse decay distance L_{xy} , Fig. 4.8b as a function of the γ_d p_T , Fig. 4.7c as a function of the γ_d longitudinal decay distance L_z , and finally, Fig. 4.8d as a function of p_T . [102][94]

- beam losses on limiting apertures, in particular on the tertiary collimators situated at almost 150 m from the IP,
- elastic beam-gas scattering (occured in the LHC ring) yielding small angle deflection of protons, which add to the loss rate due to the tertiary collimators.

- inelastic beam-gas scattering (occurred in the LHC ring) which results in shower of secondary particles. Most of these have only fairly local effects, but high-energy muons produced in such events can travel large distance and reach the detector. Simulations indicates that contributions from 500 m from IP can be seen by the detector. Usually the high-energy muon component of BIB is indicated as **beam-halo** muons, see Fig. 4.9. Due to the bending in the dipole magnet of LHC, these high-energy muons cross the detector almost horizontally, releasing radiative energy reconstructed as jet in HCal. Therefore, the beam-halo muons contribute to the background of LJ Type2.

The **cosmic-ray background**, see Fig. 4.9, is entirely due to high-energy muons that cross the detector in time coincidence with a bunch-crossing interaction. These muons mostly come from above penetrating the 60 m thick soil, and they are mainly concentrated in the barrel detector region. Just like the BIB muons, the cosmic-ray muons can give hard bremsstrahlung in the HCal producing fake jets.[104] Therefore, the cosmic-ray muons contribute at background of all LJ topologies: Type0, Type1 and Type2. Although the rate of the BIB and cosmic-ray background processes is low, they form a non-negligible background in search for rare physics processes like the LJs search.

4.8 Selection requirements on single LJ

In both the benchmark models, each event consists of two LJs. This section describes the selection requirements applied to select each LJ of the event, rejecting the background. In particular, in order to study the non-collision background (constituted by cosmic-ray and BIB background), this analysis uses samples of events collected in the empty bunch crossings with the same triggers applied on data. On the other hand, in order to optimize the selection cuts to reject the QCD multijet background, it is used a dijet control sample from data, collected during 2015, and corresponding to an integrated luminosity of 1.0 fb^{-1} .

4.8. SELECTION REQUIREMENTS ON SINGLE LJ

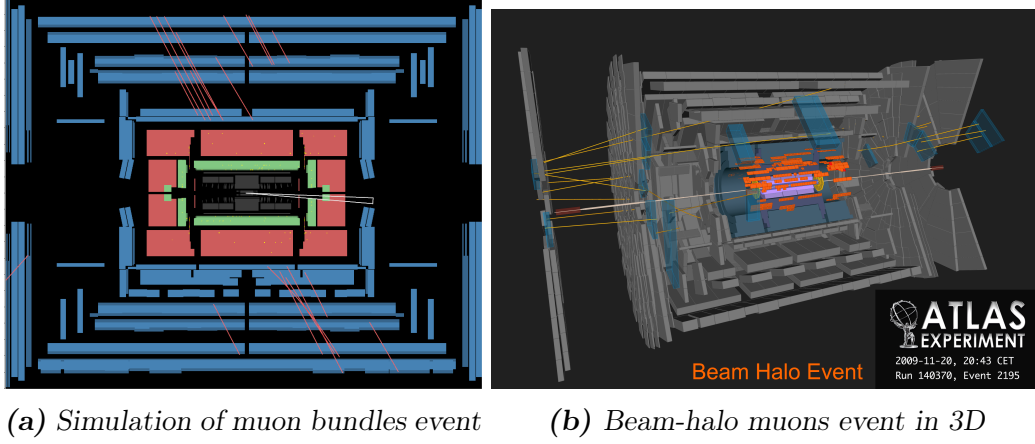


Figure 4.9: Picture showing two example of source of background in dLJs search: Fig. 4.9a shows high-energy cosmic ray muons which cross the detector in time coincidence with the bunch-crossing interaction. On the other side, Fig. 4.9b shows a BIB event constituting by high-energy muons, which are generated by inelastic beam-gas scattering inside the LHC ring.[106]

To optimize the signal LJ significance respect to the background, cuts on various variables are applied.

In order to *reduce the QCD multijet background for LJ Type2*, in addition to the requirements on jet transverse momentum ($p_T \geq 20$ GeV) and jet pseudorapidity ($|\eta| \leq 2.4$), this analysis only considers jets produced by dark photons decayed in HCal (or late in ECal). Hence, as shown in Fig. 4.10, a selection criterion to distinguish jet of LJs Type2 from QCD background is the **jet EM fraction**.

Another variable used to reject QCD multijets background is the **jet width**, see Fig. 4.11. It is a dimensionless quantity, defined as the average distance of all i -th jet constituents¹⁵ with respect to the jet direction, weighted with the energy of each i -th jet constituents:

$$W = \frac{\sum_i \Delta R^i \cdot p_T^i}{\sum_i p_T^i} \quad (4.3)$$

¹⁵The jet constituents are calorimeter clusters.

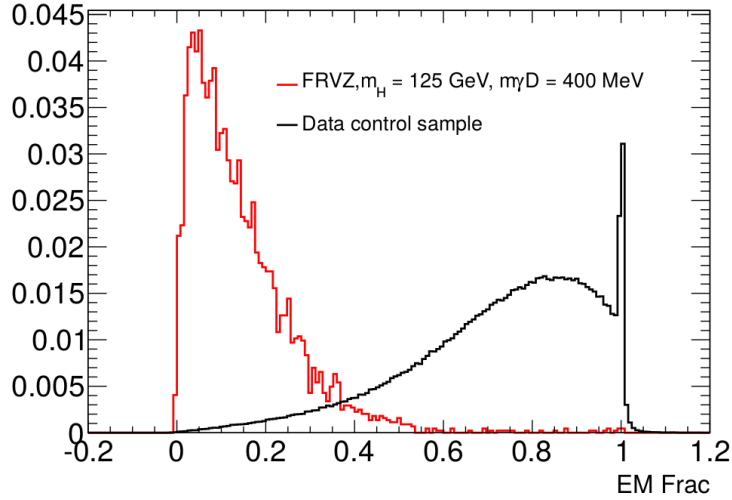


Figure 4.10: In red is shown the distribution of the EM fraction for LJ generated by a single $\gamma_d \rightarrow e^+e^-(\pi^+\pi^-)$, with γ_d decayed in HCal. In black is shown the corresponding distribution for a QCD dijet control sample from data. The cut EM fraction < 0.1 optimizes the signal significance.[94]

Where $\Delta R^i = \sqrt{(\Delta\eta_i)^2 + (\Delta\phi_i)^2}$ is the radial distance between the i -th jet constituent and the jet axis, while p_T^i is the transverse momentum of the i -th jet constituent with respect to the beam axis.

Finally, a third discriminating variable used to reject QCD multijets background from LJ Type2 signals, is the **jet vertex tagger** (JVT).[107] It is based on the sum of the p_T of tracks associated with jets from the primary interaction. In fact, the JVT is originally designed to reject jets from pile-up, keeping jets from the primary IP. Since this analysis only select LJs Type2 from γ_d displaced decays, LJs are not associated with the primary interaction, therefore in this thesis the JTV selection is applied oppositely to its typical usage.

In order to optimize the selection cuts for LJ Type2, using the three variables described above, it is applied the Tag and Probe method both on MC and dijet control data sample. For each event, the “tag” is the leading jet (i.e. the jet with higher p_T), while the “probe” is the sub-leading jet. Both tag and probe jets must have $E_T \geq 20$ GeV and $|\eta| \leq 2.4$. Moreover, in order to select back-to-back jets (expected not only in MC signal but also

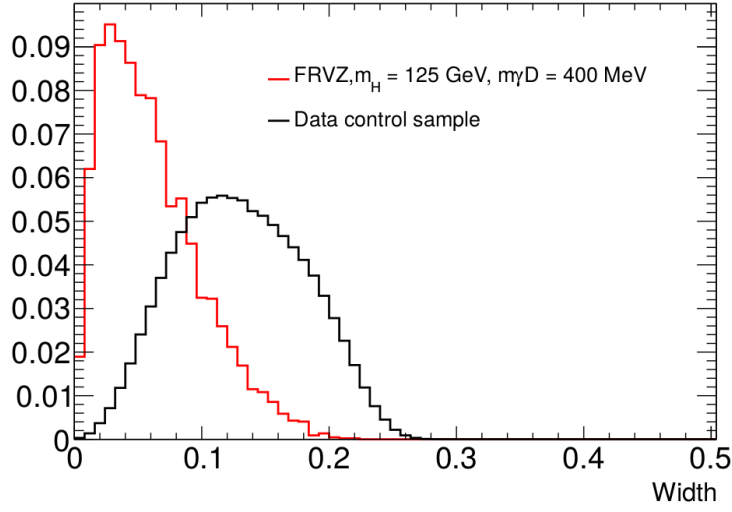


Figure 4.11: Jet width distribution for LJ generated by a single $\gamma_d \rightarrow e^+e^-(\pi^+\pi^-)$, with γ_d decayed in HCal (in red), and the corresponding distribution for a QCD dijet control sample from data (in black). The cut $W < 0.058$ optimizes the signal significance.[94]

in QCD dijet production), it is required that $\Delta\phi$ between the tag and probe jets is $\Delta\phi \geq 2.5$. To optimize the cut value, the discriminating variables are ordered accordingly to their *separation power* (SP), defined as:[108]

$$(SP)^2 = \frac{1}{2} \int \frac{(p_S(x) - p_B(x))^2}{p_S(x) + p_B(x)} dx \quad (4.4)$$

where $p_S(x)$ and $p_B(x)$ respectively are the signal and background probability density functions of a discriminating variable x . Therefore, SP is zero for identical signal and background shapes, and it is one for shapes with no overlap.¹⁶

The cut on the first variable is chosen *maximizing the signal significance*, defined as:[94]

$$\sqrt{2} \cdot \sqrt{(N_S + N_B) \cdot \log \left(1 + \frac{N_S}{N_B} \right) - N_S} \quad (4.5)$$

¹⁶In this thesis, the discriminating variables to reduce the QCD background on LJs Type2, can be ordered according their SP, as follow: *EM fraction, jet width, JVT*.

4.8. SELECTION REQUIREMENTS ON SINGLE LJ

where N_S and N_B respectively are the number of signal and background jets, with the application of a given cut on the first discriminating variable. When the signal significance is maximized, the cut on the first variable is fixed. The distributions of the other variables are re-derived applying the cut on the first variable, and the procedure starts again, until the cuts for all variables are obtained.

As shown in Fig. 4.10 and 4.11, the optimization procedure yields to the following selection cuts:¹⁷

- EM fraction < 0.1 ,
- Jet width < 0.058 ,
- JVT < 0.56 ,

In order to *reduce the BIB background for LJs Type*, it is used the ‘Two-Sided No-Time Method to tag the BIB jets as fake LJs Type2. Developed by the Non-Collision Backgrounds group, the method identifies a BIB fake jet looking for a muon segment parallel to the beam pipe, which is matched with the jet in ϕ . In particular, since the jets contained in LJ Type2 are HCal jets, the method looks for a muon tracks in both forward EC MDT detectors, matched the jet within 4° in ϕ .

Regarding the LJs Type2, another source of *background comes from the jets reconstructed in the transition region* between the barrel and end-cap cryostat, corresponding to the crack of the calorimeters. Jets in this condition have an artificially low EM fraction, therefore, to reject this background, this analysis requires that jets in the region $1.0 < |\eta| < 1.6$ (where HCal consists of Tile-Gap scintillators) have an HCal fraction of energy < 0.1 . Fig. 4.12 shows the distribution of jets as a function of η , highlighting the effect of the application of this selection requirement.

¹⁷As extensively described in [94], to validate the cut values chosen by the optimization procedure, the Rectangular Cut Optimization method can be used, obtaining similar results.

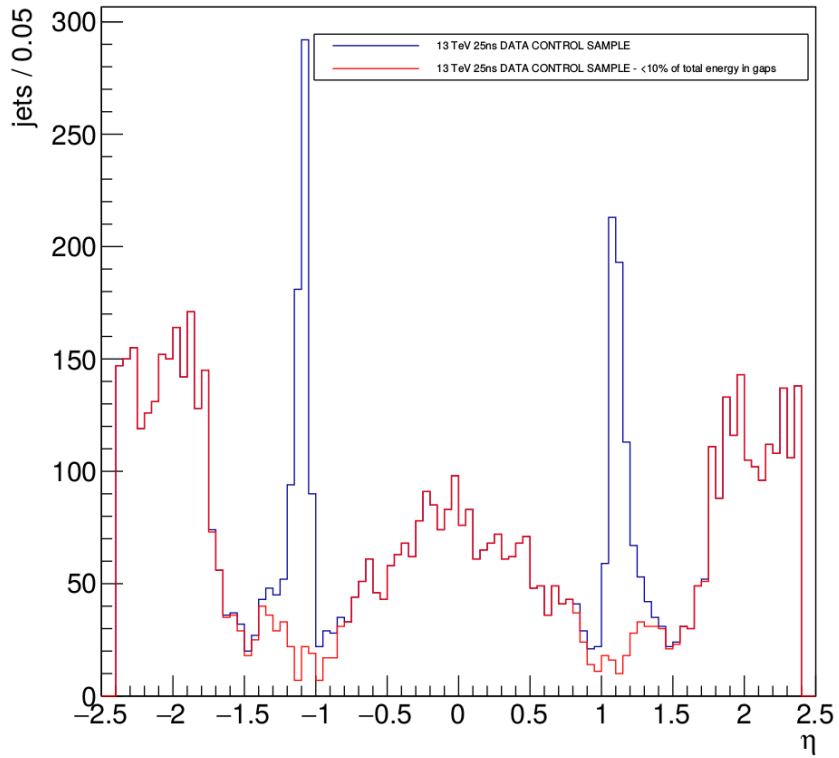


Figure 4.12: The η distribution of jets having EM fraction < 0.2 , without (blue) and with (red) requiring an energy fraction released in the Tile-Gap cells < 0.1 .[\[94\]](#)

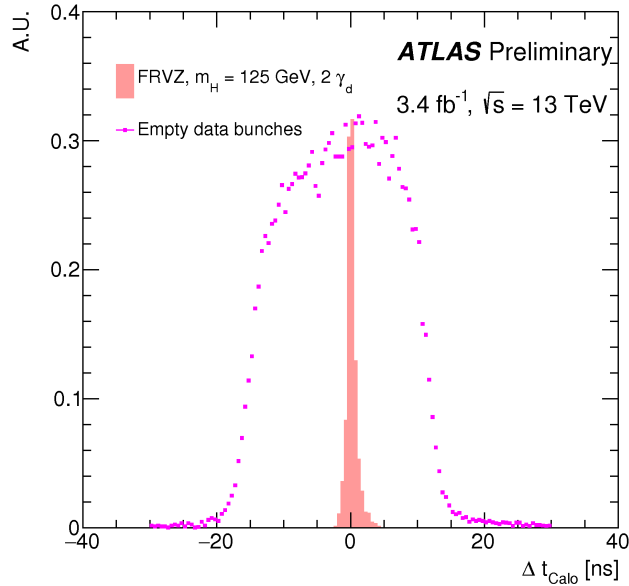


Figure 4.13: Jet timing of jets from non-collision data events (magenta squares), and the corresponding distribution for jets from Type2 LJs evaluated with MC samples (pink solid blocks).[77]

In order to *reduce the cosmic-ray background for LJs Type2 and LJs Type1*, as discriminating variable it is used the **jet timing** Δt_{Cal} . It is defined as the energy-weighted mean time difference between the bunch-crossing time ($t = 0$) and the time of energy deposition in the calorimeter. As shown in Fig. 4.13, the jet timing distribution generated by cosmic-ray muons is wide and symmetric around $t = 0$, while the timing distribution of jets generated by γ_d decays is narrow and peaked at $t = 0$. Therefore, this analysis only considers jets with $-4\text{ns} < \Delta t_{Cal} < 4\text{ns}$, and this choice allows to retain $\simeq 95\%$ of signal.

In order to *reduce the cosmic-ray background for LJs Type0* (but also for the muon contained in LJ Type1), as discriminating variable, the longitudinal muon track **impact parameter** is used. Indicated with $|z_0|$, it is defined as the minimum distance in the z -coordinate of the non-CB muon track to the *primary interaction vertex*.¹⁸

Fig. 4.14 shows that the $|z_0|$ distribution for muonic LJ constituents from

¹⁸It is the vertex whose constituent tracks have the largest $\sum p_T^2$.

4.8. SELECTION REQUIREMENTS ON SINGLE LJ

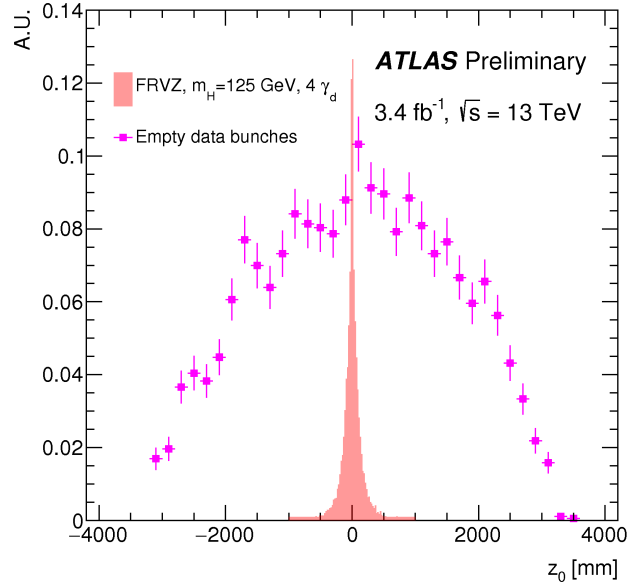


Figure 4.14: Muon impact parameter for muonic LJ constituents in empty bunch-crossings data events (magenta squares), and the corresponding distribution for muonic LJ evaluated with MC sample of $H \rightarrow 4\gamma_d + X$ with $H = 125$ GeV (pink solid blocks).^[77]

empty bunch-crossing data events is wide. On the other hand, the corresponding distribution for LJ constituents from MC sample of the FRVZ model $H \rightarrow 4\gamma_d + X$ with $H = 125$ GeV¹⁹, is narrow and peaked at $z_0 = 0$ mm. This analysis fixes as selection requirement $|z_0| \leq 280$ mm for LJ muons, allowing to reject the 96% of cosmic-ray background, with a loss signal of 5%.

The list of all the selection criteria applied on single LJ, is summarized in Tab. 4.3. The requirements are listed according to the order in which they are applied.

¹⁹It is used the MC sample of the benchmark model $H \rightarrow 4\gamma_d + X$ with $H = 125$ GeV, because in this case, the LJ constituents have a lower boost with respect the other FRVZ models. Therefore, its $|z_0|$ distribution will be wider than the others.^[77]

4.8. SELECTION REQUIREMENTS ON SINGLE LJ

Selection requirement	LJ Type
Preselection: muons with $ \eta \leq 1.0$ or $1.1 \geq \eta \leq 2.4$, in a cone of $\Delta R = 0.5$	Type0 (Type1)
Preselection: jets with $p_T \geq 20$ GeV and $ \eta \leq 2.4$, in a cone of $\Delta R = 0.5$	Type2 (Type1)
Muons have impact parameter $ z_0 < 280$ mm	Type0 (Type1)
Jets have a jet timing $-4\text{ns} < \Delta t_{Cal} < 4\text{ns}$.	Type2 (Type1)
Jet energy released in the Tile-Gap cells is $< 10\%$	Type2
Jets have an EM fraction < 0.1	Type2
Jets have a width < 0.058	Type2
Jets have a JVT < 0.56	Type2
Two-Sided No-Time Method used to reject BIB jets	Type2
Muons are non-combined at ID level	Type0 (Type1)

Table 4.3: Summary of the selection criteria for single LJ selection. The first column briefly describes the requirements, while the second one the corresponding LJ types on which the requirements act. The selection criteria are listed according to the order of application in this analysis.

CHAPTER 5

Event selection and systematics

5.1 Selection requirements at event level

In both the FRVZ benchmark models, an event consists of a pair of LJs. In order to clean the signal and reduce the background, each LJ must satisfy all selection criteria reported in Sec. 4.8. In addition, at the event level, two cuts on the following variables¹ are applied:

- the isolation of LJs ID track,
- the $|\Delta\phi|$ between the LJs.

Regarding the first cut, in both the FRVZ benchmark models, the LJs are expected to be highly isolated in the Inner Detector. Therefore, in order to reduce the QCD multijets background, this analysis requires an **ID track isolation** around the LJ direction.

The track isolation variable $\sum p_T^{ID}$ is defined as the scalar sum of the transverse momentum of the tracks with $p_T > 500$ MeV, reconstructed in the ID and matched to the primary vertex of the event, inside a cone of $\Delta R = 0.5$ around the LJ direction.[77] The requirement of matching the

¹As will be shown in Chap. 6, these two variables are used to perform the data-driven ABCD method, which allows to evaluate the residual QCD multijet, BIB and cosmic background contaminations.

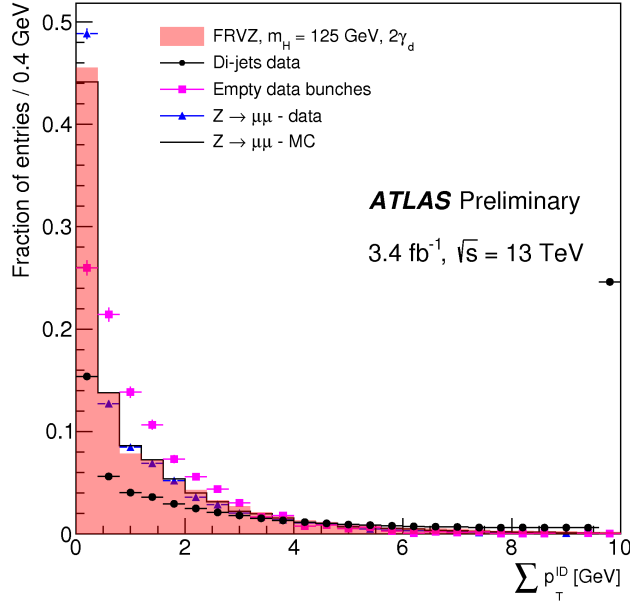


Figure 5.1: Distributions (normalized to the unit area) of the isolation variable $\sum p_T^{ID}$ evaluated for:

- 2015 data samples: dijet control sample (black circles); $Z \rightarrow \mu^+ \mu^-$ sample (blue triangles); empty bunch-crossing sample (magenta squares).
- Monte Carlo samples: FRVZ sample $H \rightarrow 2\gamma_d + X$ with $H = 125$ GeV (pink solid blocks); $Z \rightarrow \mu^+ \mu^-$ sample (black line).

The distribution corresponding to the FRVZ MC sample is very similar to the $Z \rightarrow \mu^+ \mu^-$ ones (both MC and data samples). Therefore the $Z \rightarrow \mu^+ \mu^-$ sample can be used as signal modelling to set the cut on the isolation variable. The last bin of the dijet control sample distribution is high because, only for illustration reasons, the overflow events are filled in.

5.1. SELECTION REQUIREMENTS AT EVENT LEVEL

primary interaction vertex (defined as the vertex whose constituent tracks have the largest $\sum p_T^2$) reduces the dependence on the pile-up events.

In order to set a cut on the isolation variable of ID tracks, the $\sum p_T^{ID}$ distribution of $Z \rightarrow \mu^+ \mu^-$ is used as modelling to study the corresponding $\sum p_T^{ID}$ distribution for the FRVZ models. This can be done because, as shown in Fig. 5.1, the $\sum p_T^{ID}$ distribution around a LJ from the benchmark models, is very similar to that around the muons from $Z \rightarrow \mu^+ \mu^-$ MC sample². This is true for all the LJ types contemplated by the FRVZ models.

Moreover, in order to validate the $\sum p_T^{ID}$ distribution evaluated with $Z \rightarrow \mu^+ \mu^-$ MC sample, the Fig. 5.1 also shows the $\sum p_T^{ID}$ distribution evaluated with $Z \rightarrow \mu^+ \mu^-$ from 2015 data. As it may be seen, there is very good agreement between the two $\sum p_T^{ID}$ distributions, except for the first bin in which there is a small discrepancy due to a possible mis-modelling of pile-up.[77] In addition, the Fig. 5.1 shows the $\sum p_T^{ID}$ distribution for LJs in the dijet data control sample³.

In order to have, for each event, a global variable for LJ selection, the cut is set on $\text{Max}(\sum p_T^{ID})$, which is the highest LJ isolation value obtained in a given event. Therefore, as shown in Fig. 5.1, the selection criterion of $\text{Max}(\sum p_T^{ID}) < 4.5$ GeV highly reduces the multijet background, without significantly affects the signal. The value of this cut is set optimizing the signal significance respect to the background.

Regarding the $|\Delta\phi|$ **between the two LJs** of a given event, as discussed in Chap. 4, they are approximately back-to-back. In fact, as shown in Fig. 5.2, only few FRVZ events have a small value of $|\Delta\phi|$ between the LJs. On the contrary, the $|\Delta\phi|_{LJ}$ distribution evaluated from the background samples (cosmics and BIB from empty bunch-crossing and dijets control sample) is almost flat at small angle. Therefore, the selection requirement $|\Delta\phi|_{LJ} > 0.63$ rad reduces the multijet background, without significantly affecting the signal. As the isolation variable, also this cut is set optimizing the signal

²The $\sum p_T^{ID}$ around the muons from $Z \rightarrow \mu^+ \mu^-$ must not include the ID tracks matched to the muons themselves.

³For illustration reasons, for this sample the overflow events are filled in the last bin of the $\sum p_T^{ID}$ distribution.

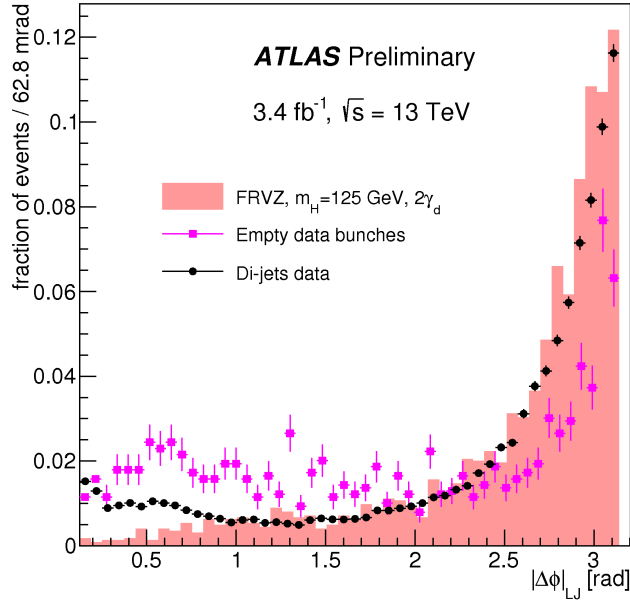


Figure 5.2: Distribution of $|\Delta\phi|$ between the two reconstructed LJs from the:

- benchmark model $H \rightarrow 2\gamma_d + X$ with $H = 125$ GeV (pink solid blocks),
- empty bunch-crossings data (black points),
- dijets control data sample (magenta squares).

significance respect to the background.

5.2 Results of cut-flow

As reported in Sec. 4.3, this analysis uses the data collected by ATLAS during 2015, and corresponding to a total integrated luminosity of 3.57 fb^{-1} . The interesting events are selected by the logical OR of the triggers listed in Sec. 4.5, and finally, a set of selection criteria is applied on each LJ of the event, such as described in Sec. 4.8. These are the key points of the **cut-flow on data**, and the results are reported in Tab. 5.1. For this calculation no selection requirements at event level are applied, i.e., no cuts on ID isolation and $|\Delta\phi|_{LJ}$.

5.2. RESULTS OF CUT-FLOW

LJ-LJ Channel	Number of events
Type0 - Type0	13
Type0 - Type1	1
Type0 - Type2	61
Type1 - Type1	1
Type1 - Type2	8
Type2 - Type2	335

Table 5.1: For each channel, it is reported the number of events after the cut-flow on data from proton-proton collisions collected during 2015. The cut-flow only consists of selection criteria on single LJ, with no selection requirements on LJ ID isolation and $|\Delta\phi|$ between two LJs.

The same cut-flow applied on proton-proton collisions data, it has been applied on on background MC samples of the processes: $t\bar{t}$, single-top, di-photon, photon+jets, Drell-Yan $e^+e^-(\mu^+\mu^-)$, Z+jets, W+jets, ZZ, WW, WZ. In this case no events survive the cut-flow.

For the cosmic, BIB, and QCD background, as will be shown in next chapter, a data-driven ABCD method is used to evaluate the residual background contamination.

Finally, the cut-flow is applied on **FRVZ MC samples** both with 125 GeV and 800 GeV Higgs bosons. Supposing a branching ratio $\text{BR}(125 \text{ GeV } H \rightarrow LJs) = 10\%$, the total number of events expected is 138 ± 3 for the $2\gamma_d$ model, and 117 ± 2 for the $4\gamma_d$ model.

Regarding the 800 GeV Higgs-like heavy scalar boson, assuming a branching ratio $\text{BR}(800 \text{ GeV } H \rightarrow LJs) = 100\%$ and a conventional cross section of 1.0 pb^4 , 70 ± 1 events survive for the $2\gamma_d$ model, while 155 ± 2 events survive for the $4\gamma_d$ model.

⁴This value is chosen only to allow easy rescaling to any other cross sections.

5.3. SYSTEMATICS UNCERTAINTIES

Source of systematic uncertainty	Values (%)
Reconstruction efficiency of single γ_d	15
Narrow-Scan trigger	6
Tri-muon-MS-only trigger	5.8
CalRatio trigger	11
Luminosity	2.1
Pile-up effect on $\sum p_T^{ID}$	5.1
Resolution of p_T of γ_d	10

Table 5.2: Summary list of all systematic uncertainties on the expected number of signal events.

5.3 Systematics uncertainties

This section describes the systematic uncertainties on the expected number of signal events. The results are summarized in Tab. 5.2.

5.3.1 On standalone muon reconstruction efficiency

The systematic uncertainty on single γ_d reconstruction efficiency, which corresponds to the systematic uncertainty on the standalone muon reconstruction efficiency, is estimated by comparing the $J/\psi \rightarrow \mu^+\mu^-$ reconstruction efficiency, as a function of ΔR between muons, for MC and data samples. The difference between the MC and data efficiency in the ΔR interval between 0.02 and 0.06 (where the FRVZ LJs are expected), is taken as systematic uncertainty. For this study we used the $J/\psi \rightarrow \mu^+\mu^-$ events because they have high statistics, and also because muons from very boosted J/ψ are collimated as in the FRVZ LJs.

The method used to evaluate the $J/\psi \rightarrow \mu^+\mu^-$ reconstruction efficiency is the **tag-and-probe** ($T\&P$) method[109], and it is applied on data collected during 2015 at $\sqrt{s} = 13$ TeV and MC samples.

The events are selected using a logical OR of triggers specifically designed

5.3. SYSTEMATICS UNCERTAINTIES

to select J/ψ mesons: HLT_muX_bJpsi_Trkloose (with X= 4, 6, 10, 18). The J/ψ events selection begins looking for the **tag**, which is a combined muon with $p_T > 4$ GeV and $|\eta| < 2.4$, firing one of the triggers⁵. Instead, the **probe** is an ID track, with $p_T > 4$ GeV and $|\eta| < 2.4$, such that the ΔR between tag and trobe is < 0.5 . Moreover, the $T\&P$ pair must be consistent with a J/ψ of $p_T > 16$ GeV and invariant mass in the region $2700 < m_{T\&P} < 3500$ MeV.

To avoid ambiguity, events in which, per each tag there is more than one probe are rejected. Once the $T\&P$ pair is found, in some cases the probe matches also the requirements of the tag. In these cases the event contains two $T\&P$ pairs and both probes have been used to measure the efficiency.

Selected $T\&P$ pairs are arranged in two statistically independent groups:

- the **matched-sample**, which consists of $T\&P$ pairs in which the probe is matched⁶ to a MS track;
- the **unmatched-sample**, which consists of $T\&P$ pairs in which the probe is not matched to a MS track.

The reconstruction efficiency is evaluated by a simultaneous log-likelihood fit of matched and unmatched-sample invariant mass distributions, using the following functions:

$$\begin{aligned} f_{mat}(m) &= H_S \epsilon S(m; \theta_S) + B(m; \theta_{B_{mat}}) \\ f_{unmat}(m) &= H_S (1 - \epsilon) S(m; \theta_S) + B(m; \theta_{B_{unmat}}) \end{aligned} \quad (5.1)$$

where m is the $T\&P$ invariant mass, ϵ is the efficiency, H_S is the signal height, and $S(m; \theta_S)$ and $B(m; \theta_B)$ are the signal and background models. In particular, an exponential function is used as background model, while as signal model it is used a combination of two Gaussian functions with same

⁵The trigger matching is defined by requiring $\Delta R < 0.005$ between the reconstructed muon and the triggered object at HLT.

⁶A probe is matched with a MS track when it exist a muon, whose ID track particle has the same p_T and η of the probe ones.

5.3. SYSTEMATICS UNCERTAINTIES

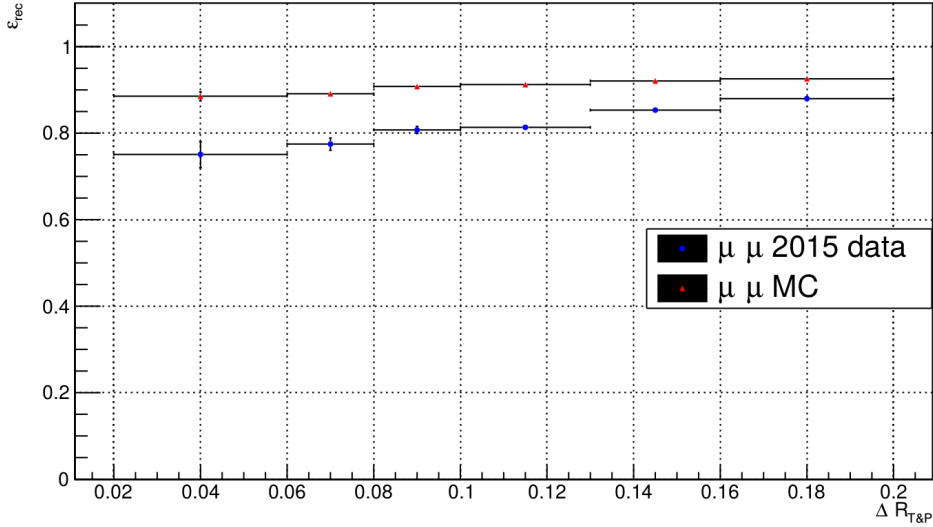


Figure 5.3: The systematics on standalone muon reconstruction efficiency is estimated by the difference between MC and data $J/\psi \rightarrow \mu^+\mu^-$ reconstruction efficiency in $\Delta R = (0.02, 0.06)$. It amounts to 15%. For low ΔR values, the efficiency decreased due to the difficulty for the MS tracking algorithms to reconstruct two tracks with small angular separation.

mean but variance in the proportion of 1/2:

$$S(m; \theta_S) = we^{-\frac{1}{2}\left(\frac{m-\bar{m}}{\sigma}\right)^2} + (1-w)e^{-\frac{1}{2}\left(\frac{m-\bar{m}}{2\sigma}\right)^2} \quad (5.2)$$

with w as weight parameter. For the fitting procedure, the signal parameters θ_S are forced to be the same in matched and unmatched-samples, while the background parameters $\theta_{B_{mat}}$ and $\theta_{B_{unmat}}$ are left to vary independently. Finally, the efficiency ϵ is extracted from the fitting procedure.

The simultaneous fit is performed in various intervals of ΔR between tag and probe⁷. The difference between MC and data $J/\psi \rightarrow \mu^+\mu^-$ reconstruction efficiency in the $\Delta R = (0.02, 0.06)$ -where the FRVZ LJs are expected- is taken as systematic uncertainty. As shown in Fig. 5.3 it amounts to 15%.

⁷The six ΔR ranges are identified by the following array:

$$\Delta R = (0.02, 0.06, 0.08, 0.1, 0.13, 0.16, 0.20)$$

5.3.2 On Narrow-Scan trigger efficiency

As the systematic on standalone muon reconstruction efficiency, also the systematic on Narrow-Scan trigger efficiency, is evaluated using the *tag-and-probe method* on $J/\psi \rightarrow \mu^+\mu^-$ events both from 2015 data and MC samples. The $J/\psi \rightarrow \mu^+\mu^-$ trigger efficiency is given as a function of the angular aperture between the two muons, and the difference between data and MC results in $\Delta R = (0.02, 0.06)$ is taken as systematic uncertainty.

As before, the interesting events are selected with a logical OR of triggers specifically designed to select J/ψ mesons: `HLT_muX_bJpsi_Trkloose` (with $X=4, 6, 10, 18$). The selection of $J/\psi \rightarrow \mu^+\mu^-$ decays begins looking for the **tag**, which is a combined muon with $p_T > 20$ GeV and $|\eta| < 2.4$, firing one of the triggers. The selection continues looking for the **probe**, which is a combined muon, with $p_T > 6$ GeV and $|\eta| < 2.4$, such that the ΔR between tag and probe is < 0.5 . Moreover, the $T\&P$ pairs must be consistent with a J/ψ with an invariant mass $2700 < m_{T\&P} < 3500$ MeV. To avoid ambiguity, only events in which there are two muons with $p_T > 6$ GeV are accepted for this study.

As done with the systematic on standalone muon reconstruction efficiency, the selected tag-and-probe pairs are arranged in two statistically independent groups:

- the **matched-sample**, which consists of $T\&P$ pairs correspondent to events in which the Narrow-Scan trigger is fired;
- the **unmatched-sample**, which consists of $T\&P$ pairs correspondent to events in which the Narrow-Scan trigger is not fired.

Following the same procedure reported for the standalone muon reconstruction efficiency, also the Narrow-Scan trigger efficiency is estimated by a simultaneous log-likelihood fit of matched and unmatched-sample invariant mass distributions, using the functions 5.1. The fits are performed in different ranges of ΔR between tag and probe. The difference between MC and data Narrow-Scan trigger efficiency, in the interval $\Delta R = (0.02, 0.06)$ is the systematic uncertainty, and it is about 0.6%.

5.3.3 Other systematics

Systematic uncertainty on Tri-muon-MS-only trigger

The uncertainty on the Tri-muon-MS-only trigger efficiency is 5.8%. It is considered the same as the Run-1 data, which is reported in [78].

Systematic uncertainty on CalRatio trigger

As before, also the systematic uncertainty on the CalRatio trigger is considered the same as the Run-1 (see [78]), and it is mainly due to the low EM fraction requirement. The value is 11%.

Systematic uncertainty on luminosity

The uncertainty on the integrated luminosity is evaluated from calibration scans of the luminosity scale using xy beam separation. The result of the systematic uncertainty on luminosity is 2.1%.

Systematic uncertainty on jet energy scale

This uncertainty, evaluated for LJ Type1 and Type2, is applied on MC events. For both the FRVZ benchmark models, the systematic uncertainty on jet energy scale is below 1%, therefore it is negligible.

Systematic uncertainty on $\sum p_T^{ID}$ due to pile-up

Pile-up can be a source of systematic uncertainty on the efficiency of the isolation selection requirement ($\sum p_T^{ID}$). This uncertainty is estimated by the comparing of the $\sum p_T^{ID}$ distribution as a function of the number of interaction vertices in the event, for muons of $Z \rightarrow \mu^+ \mu^-$ evaluated both for data and MC events. The maximum variation of $\sum p_T^{ID}$ between data and MC is considered the systematic uncertainty. It amounts to 5.1%.

Systematic uncertainties on γ_d detection efficiency and p_T resolution

The uncertainty on the γ_d detection efficiency, as a function of its decay position is negligible. On the other hand, in the MC samples, the reconstructed p_T of the γ_d differs from the generated one. This is due to the p_T resolution and this effect inducing a 10% uncertainty.

CHAPTER 6

Results and interpretations

6.1 Data-driven background estimation

The residual QCD multijet, cosmic and BIB background contaminations surviving the selection requirements, are estimated using a *data-driven likelihood-based ABCD method*[110], as recommended by the ATLAS Statistics Forum.

The ABCD method is a simplified matrix method, based on the assumption that the background is factorizable in a plane of two uncorrelated variables. An appropriate cut on these two variables, allows to identify four regions “A”, “B”, “C”, “D”, where A is the **signal-region**, while the other three are the **control-regions**. Therefore, the ABCD method allows both to evaluate the background contamination, and to optimize the selection requirements defining the signal region.

Using the ABCD method, the number N_A of background events in the signal region, is estimated using the control regions as:

$$N_A = \frac{N_D N_B}{N_C} \quad (6.1)$$

In this analysis the variables used to identify the signal region are: $\text{Max}(\sum p_T^{ID})$ and $|\Delta\phi|_{LJ}$, which are event-level variables with low correlation factor. After

6.1. DATA-DRIVEN BACKGROUND ESTIMATION

the validation of the ABCD method¹ in the control regions using unoptimized cuts on the two variables, the results of cut optimization identify the signal region: $\text{Max}(\sum p_T^{LD}) \leq 4.5 \text{ GeV}$ and $|\Delta\phi|_{LJ} \geq 0.628 \text{ rad}$, see Fig. 6.1.

These two cuts must be added in the cut-flow process to select the signal, while the formula 6.1 must be used to evaluate the expected background to the signal region.

The Tab. 6.1 shows, for each channel decay, the observed data events highlighting the effects of adding these two event-level requirements to the original cut-flow constituted only by selection criteria on single LJ (as already discussed in the previous chapter in Tab. 5.1). Taking into account the

¹Going into detail, the ABCD method performs a simultaneous fit of the observed events in the four regions. The overall likelihood function is:

$$L(n_A, n_B, n_C, n_D | \mu, \theta_\mu) = \prod_{i=A,B,C,D} \frac{e^{-N_i} N_i^{n_i}}{n_i!} \quad (6.2)$$

where n_i are the four observables describing the number of observed events in the four regions; μ is the parameter of interest defined as the ratio between the observed and expected number of signal events in the region A; θ_μ is the set of nuisance parameters describing the different backgrounds and the systematic uncertainties. All the systematic uncertainties listed in Sec. 5.3 have been taken into account. Moreover, two additional sources of systematic uncertainty must be considered:

- the residual correlation between the variables $\text{Max}(\sum p_T^{LD})$ and $|\Delta\phi|_{LJ}$, which causes a systematic uncertainty of 15%;
- the non-closure of the ABCD method performed on the sum of cosmic-ray, BIB and dijets samples, which causes a systematic uncertainty of 22%.

Therefore, the two contributions give a systematic uncertainty of 27%. The four parameters N_i are defined as:

$$\begin{aligned} N_A &= \mu N_{A,expected}^S + N_A^B \\ N_B &= \mu \epsilon_B + N_B^B \tau_B \\ N_C &= \mu \epsilon_C + N_C^B \tau_B \tau_D \\ N_D &= \mu \epsilon_D + N_D^B \tau_D \end{aligned}$$

where $\epsilon_B, \epsilon_C, \epsilon_D$ are estimated from MC, and describe small leakages of signal into the control regions; τ_B, τ_D are the nuisance parameters describing the ratio between the expected number of background events in the control region and in the signal one (from the ABCD method ansatz: $A = BD/C$). The overall likelihood 6.2 is multiplied with additional Gaussian probability distribution functions to constrain the nuisance parameters. Best estimates of the nuisance parameters and of the parameter of interest are obtained using profile likelihood fits, and p-values and signal limits are derived using the CLs as described in [111].

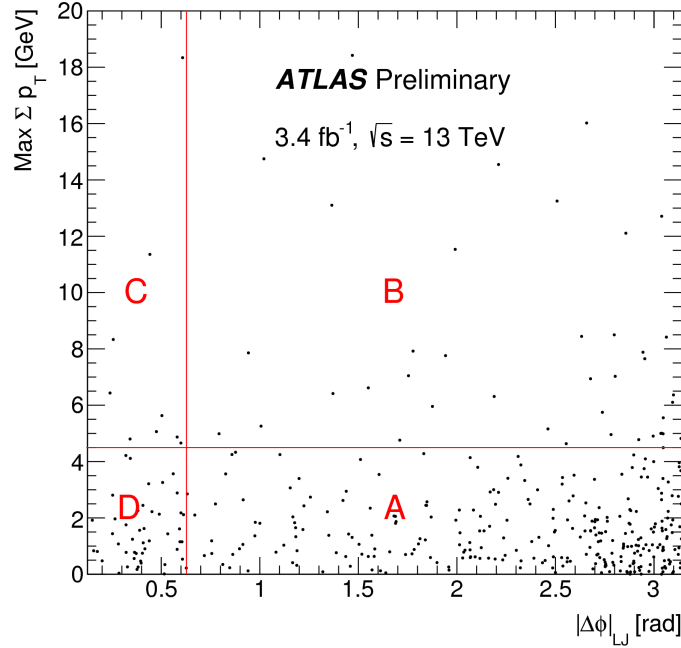


Figure 6.1: Scheme of the ABCD method in the plane $|\Delta\phi|_{LJ}$, $\text{Max}(\sum p_T^{LD})$. According to the FRVZ models, LJs have high $|\Delta\phi|_{LJ}$ and low $\text{Max}(\sum p_T^{LD})$ (because they are highly isolated and produced mostly back-to-back).^[77]

expected high background for the Type2–Type2 events, the ABCD method is performed on three categories: all events, excluding the Type2–Type2 event, and only the Type2–Type2 event. The results of ABCD estimations and **full cut-flow on data** from proton-proton collisions collected during 2015 are shown in Tab. 6.2. As it may be seen, in all categories, no evidence of signal is observed.

Besides the data, the full cut-flow (contained selection requirements on single LJ, on LJ ID isolation and on $|\Delta\phi|_{LJ}$) is **applied on FRVZ MC samples** too. In order to compare data and MC results, the number of MC events are rescaled to the production cross-section of the sample processed multiplied by the total integrated luminosity of 2015 data (3.5 fb^{-1}). For the 125 GeV Higgs boson it is considered the SM gluon fusion Higgs production cross section, while for the 800 GeV heavy scalar boson a conventional cross section of 1.0 pb is used.

6.1. DATA-DRIVEN BACKGROUND ESTIMATION

Channel	Single LJ cut-flow	Full cut-flow
Type0 - Type0	13	9
Type0 - Type1	1	0
Type0 - Type2	61	37
Type1 - Type1	1	0
Type1 - Type2	8	0
Type2 - Type2	335	239

Table 6.1: For each channel of LJs pair, it is shown the number of events surviving the cut-flow on data from proton-proton collisions collected during 2015. In particular, the second column refers to the results obtained after applying the selection requirements on single LJ, while the third column refers to the observed events after the full cut-flow (single LJ selection and cuts on $|\Delta\phi|_{LJ}$ and $\text{Max}(\sum p_T^{LD})$).[\[112\]](#)[\[94\]](#)

Category	Observed events	Expected background
All channels	285	231 ± 12 (stat) ± 62 (syst)
Type2 - Type2 excluded	46	31.8 ± 3.8 (stat) ± 8.6 (syst)
Type2 - Type2 only	239	241 ± 41 (stat) ± 65 (syst)

Table 6.2: Number of observed events on data from proton-proton collisions collected during 2015, after the application of the whole cut-flow. The corresponding residual background estimated with the ABCD method are reported too.[\[77\]](#)

6.2. LIMITS IN FRVZ MODELS

Channel	$m_H = 125 \text{ GeV}$		$m_H = 800 \text{ GeV}$	
	$H \rightarrow 2\gamma_d + X$	$H \rightarrow 4\gamma_d + X$	$H \rightarrow 2\gamma_d + X$	$H \rightarrow 4\gamma_d + X$
Type0 - Type0	80 ± 2	70 ± 2	16.0 ± 0.2	56.0 ± 0.8
Type0 - Type1	-	16.0 ± 0.8	-	17.0 ± 0.4
Type0 - Type2	31 ± 1	9.0 ± 0.6	27.0 ± 0.5	31.0 ± 0.6
Type1 - Type1	-	1.0 ± 0.2	-	1.4 ± 0.1
Type1 - Type2	-	0.01 ± 0.01	-	3.3 ± 0.2
Type2 - Type2	2.0 ± 0.5	0.34 ± 0.10	10.0 ± 0.3	3.2 ± 0.2
All channels	113 ± 2	96 ± 2	53.0 ± 0.6	112 ± 1

Table 6.3: Number of LJ pairs surviving the full cut-flow on the FRVZ MC samples. The 2nd and 3rd column refer to the two FRVZ models with 125 Higgs boson, while the 4th and 5th refer to the same models with 800 GeV heavy scalar boson. In the last row is shown the total expected number of signal events.

Assuming that the branching ratio of 125 Higgs boson to Hidden Sector is 10%, the total expected number of signal events is 113 ± 2 for the FRVZ model with $2\gamma_D$, and 96 ± 2 for the FRVZ model with $4\gamma_D$, see Tab. 6.3.

On the other hand, assuming that the branching ratio of 800 GeV heavy scalar boson to Hidden Sector is 100%, the total expected number of signal events is 53.0 ± 0.6 for the FRVZ model with $2\gamma_D$, and 112 ± 1 for the FRVZ model with $4\gamma_D$, see Tab. 6.3.

6.2 Limits in FRVZ models

As seen in the previous section, no evidence of signal is observed in data from proton-proton collisions collected during 2015. Therefore, the result of the LJs search is used to set, for the two benchmark models, upper limits on the Higgs boson BR to LJs, as a function of the γ_D mean lifetime. Since the channel LJs Type2-Type2 has high background and low signal efficiency, it has been excluded.

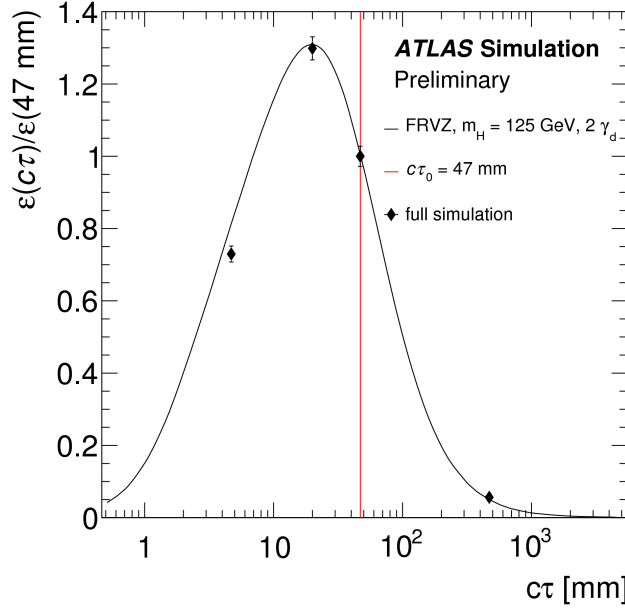


Figure 6.2: Ratio of the γ_D detection efficiency at a given $c\tau$ to that at $c\tau_0 = 47$ mm (red line) for the model 125 GeV $H \rightarrow 2\gamma_d + X$. The black points refer to the values of this ratio using MC full simulation at $c\tau = 4.7, 20, 47, 470$ mm, and they are in good agreement with the pseudo experiment process.^[77]

The limit setting as a function of the γ_D mean lifetime $c\tau$, is performed using the CLs method^[113], both for FRVZ models with $2\gamma_D$ and with $4\gamma_D$, considering both 125 GeV and 800 GeV Higgs bosons.

The CLs procedure begins with the set up of **MC pseudo experiments**, as described in the following steps:

1. The FRVZ MC signal sample 125 GeV $H \rightarrow 2\gamma_d + X$ with $c\tau_0 = 47$ mm is chosen as *MC reference sample*.
2. For this MC reference sample, have been evaluated the γ_D detection efficiency² after the full cut-flow, as a function of the γ_D decay length (L_{xy} in the barrel, L_z in the end-cap) and transverse momentum p_T . Therefore, two γ_D detection efficiency tables are produced: one as a function of L_{xy} and p_T , the other as a function of L_z and p_T .
3. A large number of *MC pseudo experiments* of the model $H \rightarrow 2\gamma_d + X$

²Efficiency is understood to mean acceptance times efficiency.

6.2. LIMITS IN FRVZ MODELS

are produced. Each i -th MC pseudo experiment has a different γ_D mean lifetime chosen in the range $0.5 \leq c\tau_i \leq 5000$ mm, while the p_T and η of the γ_D are extracted from the MC reference sample. For each i -th MC pseudo experiment, the γ_D decay length (L_{xy} and L_z) is obtained using an exponential distribution whose parameter is the mean lifetime $c\tau_i$.

4. Based on the γ_D transverse momentum and decay length, each i -th MC pseudo experiment is weighted by the corresponding γ_D detection efficiency (obtained from the efficiency tables built at 2).
5. The number of detected events in each i -th MC pseudo experiments, is rescaled by the ratio of the integrated detection efficiency at $c\tau_i$ to the integrated detection efficiency at $c\tau_0$. The distribution of this ratio is shown in Fig. 6.2.

This procedure is repeated for the other benchmark models: 125 GeV $H \rightarrow 4\gamma_d + X$ and 800 GeV $H \rightarrow 2(4)\gamma_d + X$.

The number of detected events from the MC pseudo experiments, and the expected number of background events in the signal region obtained from the ABCD method, are used as input of the **CLs method** to obtain upper limits at 95% on the cross section times branching ratio ($\sigma \times \text{BR}$) of Higgs boson to LJs in the benchmark models.

The exclusion limits on $\sigma \times \text{BR}$, as a function of γ_D mean lifetime, for the two FRVZ models with 125 GeV Higgs boson are shown in Fig. 6.3. The results are obtained excluding the channel LJs Type2-Type2, and assuming a $\sigma = 44.13$ pb (which is the SM gluon fusion Higgs production cross section). The expected limit is shown as the dashed curve, while the solid curve corresponds to the observed limit. The horizontal lines, which indicate $\sigma \times \text{BR}$ for the two possible values of SM Higgs boson branching ratio to dark photons, define the 95% CL exclusion limits. Therefore, using a $\text{BR}(125 \text{ GeV } H \rightarrow LJs) = 10\%$, the $\sigma \times \text{BR} \simeq 4.4 \text{ pb}$ and the range of γ_D mean lifetime excluded is **$2.2 \leq c\tau \leq 11.3$ mm for the FRVZ model with $2\gamma_D$, and $3.8 \leq c\tau \leq 163.0$ mm for the FRVZ model with $4\gamma_D$.**

6.2. LIMITS IN FRVZ MODELS

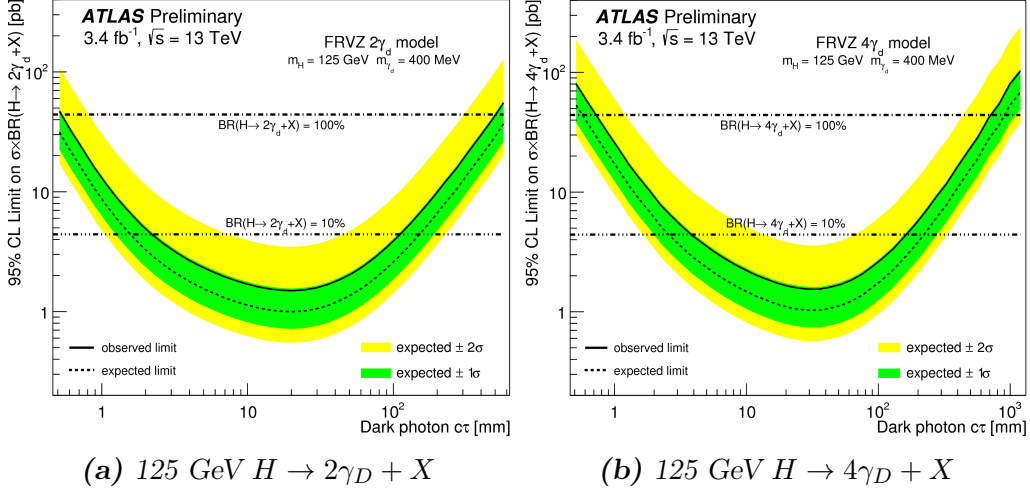


Figure 6.3: The 95% upper limits on the $\sigma \times BR$ as a function of the γ_D lifetime ($c\tau$), for the FRVZ models with 125 GeV Higgs. The Fig. 6.3a shows the limits for the FRVZ model $H \rightarrow 2\gamma_D + X$, while Fig. 6.3b for the FRVZ model $H \rightarrow 4\gamma_D + X$. The horizontal lines correspond to $\sigma \times BR$ for two values of the BR of the Higgs boson decay to dark photons.[77]

Similarly, the upper limits using 800 GeV Higgs-like heavy scalar boson are shown in Fig. 6.4. The channel LJs Type2-Type2 was excluded, and the 95% CL exclusion limits are obtained assuming a $\sigma \times BR$ of 5 pb (horizontal line) and a $BR(H \rightarrow LJs) = 100\%$ for the 800 GeV heavy scalar decay to FRVZ LJs. Therefore, the range of γ_D mean lifetime excluded is $0.6 \leq c\tau \leq 63 \text{ mm}$ for the FRVZ model with $2\gamma_D$, and $0.8 \leq c\tau \leq 186 \text{ mm}$ for the FRVZ model with $4\gamma_D$.

Recent observation of anomalous internal pair creation in Beryllium-8 (${}^8\text{Be}$), is interpreted as a possible signature of a light, neutral “protophobic” boson of 16.7 MeV decaying in e^-e^+ pairs from the dark sector.[114] A TYPE2-TYPE2 signal can be related to the framework of this protophobic boson assuming that a 800 GeV Higgs-like heavy scalar boson with a BR of 100% to $2\gamma_D + X$. The γ_D mass is assumed 16.7 MeV and it decays only to electron pairs. Fig. 6.5 shows the the 95% upper limits on the $\sigma \times BR$, as a function of γ_D mean lifetime $c\tau$. Assuming a $\sigma \times BR = 10 \text{ pb}$, the range excluded is $2.7 \leq c\tau \leq 21 \text{ mm}$.

6.2. LIMITS IN FRVZ MODELS

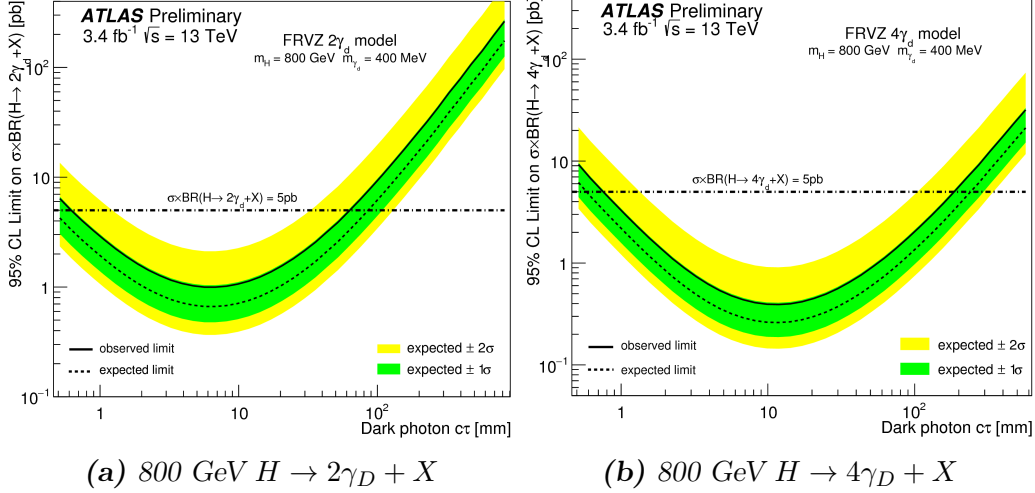


Figure 6.4: The 95% upper limits on the $\sigma \times BR$ as a function of the γ_D lifetime ($c\tau$), for the FRVZ models with 800 GeV Higgs-like heavy bosons. The horizontal lines correspond to a $\sigma \times BR$ of 5 pb.[77]

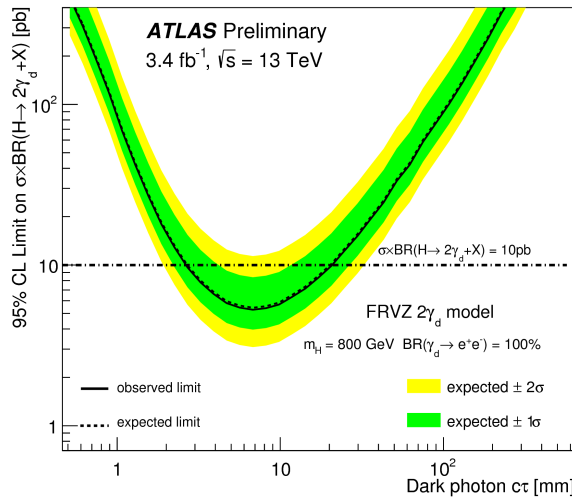


Figure 6.5: The 95% upper limits on the $\sigma \times BR$ as a function of the γ_D lifetime for the FRVZ model $H \rightarrow 2\gamma_D + X$, with a $m_{\gamma_D} = 16.7 \text{ MeV}$. The $BR(800 \text{ GeV } H \rightarrow LJs)$ is assumed of 100%. The horizontal line corresponds to $\sigma \times BR = 10 \text{ pb}$. [77]

Conclusions

This thesis broaches two complementary subjects: the searching for long lived particle decaying in LJs analyzing data collected by ATLAS experiments, and the construction of detectors that will be installed in ATLAS. In order to study new physics phenomena, in fact, it is necessary to have detector more and more efficient, developing both engineering and physics skills.

In the last century, the Standard Model has been widely verified by a large number of particle physics experiments. However, there are many theoretical and experimental unanswered questions, like the muon anomalous magnetic dipole moment and the Dark Matter mystery. In order to find a solution for these issues, recently, theories *beyond the Standard Model* arouse great interest in the international scientific community. In particular, at CERN thousand of particle physics use the most powerful particle accelerator, searching for evidences leading to an explanation.

Several theories beyond the Standard Model predict the existence of a *Hidden Sector* weakly coupled to the visible one. In order to consider the simplest case, in this thesis the Hidden Sector is a non abelian group $U(1)$, whose symmetry is broken at low energy scale, and the associated neutral gauge boson, called **dark photon** (γ_D), has mass in the range of MeV to GeV. The weakly coupling between Hidden Sector and Standard Model is obtained by a *low kinetic mixing* between the dark photon and the visible one, which allows dark photon decays in the Standard Model.

Due to the γ_D low mass and non-negligible lifetime, the dark photon decays at LHC produce **displaced Lepton Jets** structures. In order to

CONCLUSIONS

be as much as possible model independent, a generic definition of displaced Lepton Jets has been used in this thesis: collimated jets of high energetic muons, electrons and pions pairs produced far away from the proton-proton interaction point.

Although no evidence of signal is found analyzing proton-proton collisions at $\sqrt{s} = 13$ TeV, this work has successfully determined a set of selection criteria capable to isolate the dark photon signature in the ATLAS detector, and to reduce the Standard Model backgrounds. Moreover, this analysis uses as benchmark, two simplified *Falkowsky-Ruderman-Volansky-Zupan models*, in which the SM Higgs boson (or an 800 GeV Higgs-like heavy scalar boson) decays to dark photons of 400 MeV, producing a Lepton Jets pair. For the benchmark models, this analysis has set *upper limits* at 95% on the SM Higgs boson (and heavy scalar Higgs boson) branching ratio to Lepton Jets, as a function of γ_D mean lifetime $c\tau$.

In particular, for the benchmark model $H \rightarrow 2\gamma_d + X$, the exclusion limits found are $2.2 \text{ mm} \leq c\tau \leq 11.3 \text{ mm}$ and $0.6 \text{ mm} \leq c\tau \leq 63 \text{ mm}$, respectively for the 125 GeV and 800 GeV Higgs boson. On the other hand, for the benchmark model $H \rightarrow 4\gamma_d + X$, the ranges of γ_D mean lifetime excluded are $3.8 \text{ mm} \leq c\tau \leq 163.0 \text{ mm}$ and $0.8 \text{ mm} \leq c\tau \leq 186 \text{ mm}$, respectively for the 125 GeV and 800 GeV Higgs boson. Comparing these results to those obtained using data from proton-proton collisions as $\sqrt{s} = 8$ TeV (see [78]), this analysis has found stricter exclusion range, due to the improvements in trigger and reconstruction efficiencies.

In order to further improve the results of this analysis, besides increasing the integrated luminosity and the energy of the center of mass, it is very important to improve both trigger and reconstruction efficiency. In fact, the standard ATLAS triggers require tracks pointing back to the interaction point, therefore, they are not designed for exotic physics which predict the existence of long lived particles. Similarly, many Hidden Valley models (as the FRVZ described in this thesis) predict particles in the final states with very small opening angle. The current ATLAS tracking system is not designed for these kind of physics searches.

CONCLUSIONS

Therefore, the ATLAS Collaboration have planned the Phase-II TDAQ upgrade, which is designed to enable a wide range of precision measurements and searches for rare processes within or beyond the Standard Model. This upgrade will be performed in 2024 – 2027, and takes advantage of other ATLAS detector system that will be upgraded during the Phase-I (2019 – 2020) and Phase-II upgrades. In particular, the New Small Wheel, which will be installed during the Phase-I upgrade, meets the Phase-II requirements of angular resolution of 1 mrad, and are designed to operate at high luminosity conditions.[63] Therefore, the New Small Wheels are an important upgrade towards future improvements for the exotic physics searches.

During the *ATLAS Phase-I upgrade* (2019 – 2020);, the existing Small Wheels (SW) located in the inner layer of the end-cap region of the Muon Spectrometer, will be replaced by the **New Small Wheels** (NSW). The main reason of this upgrade lies in the necessity to improve the tracking performance and to reduce the trigger rate including the NSW in the Level-1 trigger, in order to consolidate and improve the physics capabilities of the ATLAS detector in view of the instantaneous luminosity increasing.

The NSW will be constituted by a set of precision tracking and trigger detectors able to work at high rates of incident particles, and it will ensure a momentum resolution of 15% for muons with $p_T \sim 1$ TeV. Each of the NSW will consist of 16 sectors constituted of a combination of “small-strip Thin Gas Chambers” (sTGC) and **Micro-MEsh Gaseous Structure detector** (MicroMegas). Although sTGC will be primarily dedicated to trigger, while MicroMegas to tracking, in order to obtain a redundant detector system, both detectors will be used for trigger and precision tracking measurements.

The NSW will be equipped with eight layers of MicroMegas detectors, arranged in two *quadruplets*, for a total of 1200 m² of active layers. All quadruplets have trapezoidal shapes with surface areas between 2 – 3 m². In order to achieve the NSW resolution requirements, the MicroMegas must have a spatial resolution of 100 μ m on the precision coordinate, of 2–3 mm in the azimuthal coordinate, and an angular resolution of 1 mrad. Therefore, a challenging mechanical precision is required, especially considering the large

CONCLUSIONS

detector dimensions.

This thesis has described the NSW MicroMegas detector technology, focusing on the construction procedure of the SM1 MicroMegas quadruplets.

Appendices

Appendix

I Interaction of charged particles with matter

When a charged particle passes through a gaseous medium, the most probable interaction is the electromagnetic one. In particular, the main process is the Coloumb interaction between the electromagnetic field of the incoming particle and of the medium, resulting in both *excitation* and *ionization* of the atoms of the medium itself.[6]

Moreover, if the particle is heavier than electron, processes like Cerenkov, bremsstrahlung and transition radiation can be neglected. In this condition, the average energy loss dE per unit length dx is described by the **Bethe and Block equation**:

$$\frac{dE}{dx} = -4\pi N_A r_e^2 m_e c^2 \frac{Z}{A} \frac{z^2}{\beta^2} \left(\ln \frac{2m_e c^2 \gamma^2 \beta^2}{I} - \beta^2 - \frac{\delta(\beta)}{2} \right) \quad (3)$$

where N_A is the Avogadro number; z , β and γ respectively are the charge, the velocity (in unit of c) and the Lorentz factor of the incident particle; Z and A are the atomic and mass number of the medium, respectively; I is the mean excitation energy of the atoms of the medium; m_e and r_e are the electron mass and radius. The $\delta(\beta)$, so-called density term, is a correction term introduced by Fermi. It depends on the material density, and for gases under normal pressure can be neglected.[68][71]

As shown in Fig. 6, at first the average energy loss decreases rapidly due to the term $1/\beta^2$. For relativistic energies (when the particle velocity is $\beta \simeq 0.95$, therefore $\beta\gamma \simeq 3$), the curve reaches a minimum. A particle

I. INTERACTION OF CHARGED PARTICLES WITH MATTER

at the energy loss minimum is called **minimum ionizing particle**. After the minimum, the energy loss increases due to the logarithmic term (see eq. 3). The logarithmic rise is limited by polarization of the medium, which is described by the density term. Therefore, at high $\gamma\beta$ values, the average energy loss reaches a plateau, see Fig. 6.

Bethe-Bloch equation gives only the average energy loss of charged particles by ionization and excitation processes. For thin absorbers like gaseous detectors, strong fluctuations around the average energy loss appear. Therefore, the shape of the energy loss distribution is described by the *Landau distribution*.^{[71][64]}

When a charged particle passes through a gaseous medium and ionizes it, pairs of electrons (so-called *primary electrons*) and ions are liberated. Once released in the gas, and under the influence of an applied electric field, electrons and ions drift in opposite directions and diffuse towards the electrodes. Sometimes the ejected electrons have energy larger than the ionization potential of the medium, therefore, they produce *secondary electrons*.^[71] This results in the creation of an **electron avalanche** with a drop-like shape, see Fig. 7. Since the electron drift faster than ions (because their mass is smaller), the electrons distribute on the head of the drop, leaving behind the ions.

Assuming that, for a constant electric field, the electron **drift velocity** is constant ($\dot{\vec{v}}_{drift} = 0$), it can be parameterized by:

$$\vec{v}_{drift} = \frac{\mu}{1 + \omega^2\tau^2} \left(\vec{E} + \frac{\omega\tau}{B}(\vec{E} \times \vec{B}) + \frac{\omega^2\tau^2}{B^2}(\vec{E} \cdot \vec{B})\vec{B} \right) \quad (4)$$

where \vec{B} and \vec{E} are the magnetic and electric field, respectively; τ is the average time between two electron-gas collisions; $\mu = \frac{e\tau}{m}$ is the mobility; $\omega = \frac{eB}{m}$ is the cyclotron frequency.^[115]

If $\vec{E} \perp \vec{B}$, the drift velocity becomes:

$$|\vec{v}_{drift}| = \frac{\mu E}{\sqrt{1 + \omega^2\tau^2}} \quad (5)$$

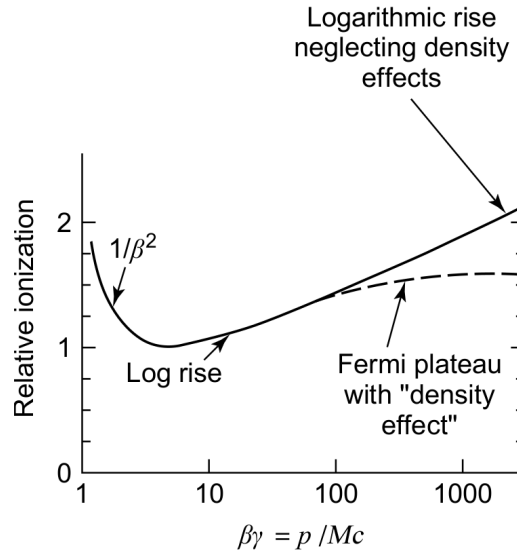


Figure 6: Ionization energy loss as a function of $\beta\gamma$, for a charged particle of mass M and momentum p . As it may be seen, the average energy loss decreases as $1/\beta^2$ in the low velocity region, reaching the energy loss minimum at $\beta\gamma \simeq 3$. After that, the curve is characterized by a logarithmic rising, and a plateau due to the density term.

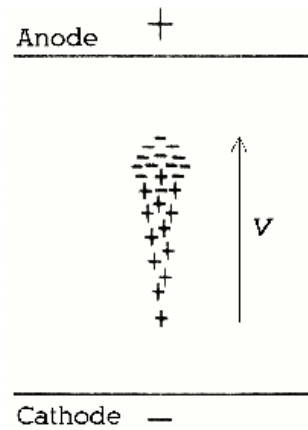


Figure 7: Sketch of the drop-like shape of an avalanche formation.

I. INTERACTION OF CHARGED PARTICLES WITH MATTER

In this condition, the angle α between the drift velocity and the electric field is called **Lorentz angle**, and it is described by:

$$tg(\alpha) = \omega\tau = v_{drift} \frac{B}{E} \quad (6)$$

As electrons and ions drift within the gas medium, they have multiple collisions with the gas atoms and molecules. These ionizations produce a deviation of electrons and ions from their initial trajectory. This process is called **diffusion** and can be described with by the following Gaussian distribution:

$$\frac{dN}{N} = \frac{1}{\sqrt{4\pi Dt}} \exp\left(-\frac{x^2}{4Dt}\right) dx \quad (7)$$

where $\frac{dN}{N}$ is the fraction of the charge which is found in the length element dx at a distance x after a time t , and D is the diffusion coefficient.[115] The standard deviations for a linear or volume diffusion are, respectively:

$$\begin{aligned} \sigma_x &= \sqrt{2Dt} \\ \sigma_y &= \sqrt{3}\sigma_x = \sqrt{6Dt} \end{aligned} \quad (8)$$

The drift velocity and diffusion of electrons depend on the nature of the gas. In fact, the inelastic cross-section involves the rotational and vibrational levels of molecules: in noble gases, the inelastic cross section is zero below excitation and ionization thresholds. Large drift velocities are achieved by adding *polyatomic gases* (usually CH_4 , CO_2 , or CF_4) having large inelastic cross sections at moderate energies, which results in “cooling” electrons into the energy range of the elastic cross-section of argon (~ 0.5 eV). The reduction in both the total electron scattering cross-section, and the electron energy results in a large increase of electron drift velocity.[68]

Another principal role of the polyatomic gas is to absorb the ultraviolet photons emitted by the excited noble gas atoms, for this reason they are called **quench gases**. The choice of the polyatomic gases depends also by other reasons like the ageing consequences and the safety. Especially for large gaseous detectors, it is important to use non-flammable and non-corrosive

gases.

II Gas tightness test of SM1 MicroMegas panel

The gas tightness test is one of the essential QA/QC test performed on the MicroMegas quadruplets. The pressure decay rate of an air volume contained in a single SM1 MicroMegas panel vessel is used to estimate the gas tightness of the panels of the NSW Micromegas Multiplets. Because the vessel volume changes sensibly during the gas fill to reach the overpressure from which the gas test starts, the gas leak rate must be deduced from the drop rate of the product between the pressure and volume PV of the gas-gap between the vessel and the panel. The volume variation is deduced from the relation between the air flow volume inserted into the gas-gap V_{air} and the relative pressure rise ΔP . The PV decay rate method and the influence of room temperature and atmospheric pressure on this estimate are described.

II.a Gas leak rate specification

The NSW MicroMegas quadruplets are filled with Ar:CO₂ (93:7) at an overpressure of 2 mbar and with a flux of 6.8 – 10.4 Nl/h. The main reason of flushing fresh gas into the chamber is to reduce the air contamination due to the gas sealing limit of the Micromegas Quadruplets. Calculations to determine the feasible gas sealing level of this detector were made by T. Alexopoulos, S. Maltezos et al., and are reported in [116]. The authors of this work employed the principles of the Contact Mechanics and the Percolation theory, taking into account: (i) the properties of the surfaces, (ii) the elastomer rope plane modulus, (iii) the parameters of the sealing system, and they determined the gas leak rate as a function of the squeezing pressure.

The elastomer used for the NSW MicroMegas quadruplets is EPDM shore A 70. It has 7 mm diameter, viscoelastic modulus $E = 0.675$ MPa and planar elastic modulus $E' = 0.892$ MPa. This elastomer is placed between two parallel different hard surfaces: the FR4 layer (of the drift panel), and the Kapton layer (of the readout panel). In the best case, the feasible gas leak

II. GAS TIGHTNESS TEST OF SM1 MICROME GAS PANEL

rate amounts to $0.07 \pm 30\%$ mbar/h when the gauge pressure is 3 mbar and the squeezing pressure is 3.2 bar (assumed uniform along the elastomer rope). This value is about 1/10 lower than the nominal acceptance limit set by the ATLAS-NSW specifications 0.6 mbar/h[59], and the reasonable leakage level of MicroMegas quadruplets have to be in the interval **0.07 - 0.6 mbar/h**.

Due to the different roughness of the two hard surface employed in the MicroMegas quadruplets, the gas leak is dominated by the small orifices present between the FR4 surface and the O-Ring (the Kapton does not contribute to the result since its roughness is much smaller compared to that of FR4). These orifices are seen also by the air molecules that can enter into the detector active volume and contaminate the gas mixture. The associated mechanism is the air binary diffusion to the Ar/CO₂ mixture. From empiric consideration it is possible to assume that the tightness to air (from exterior to interior) is of the same order of magnitude that to Ar/CO₂ (from the interior to exterior).

Theoretical calculation are ongoing to evaluate the quantity of air moles per time unit that enter into the detector active volume.

Detector performance simulations based on Garfield program and test with small prototypes, have demonstrated that the detector gain is reduced of 10% with an air contamination of 1%. This is due to the presence of electronegative gas molecules like oxygen that remove electrons from the multiplication process. If the air enters into the chamber approximatively at same rate as well as the Ar/CO₂ leak, and the gas renews at rate of 4 complete volume change per day, the air contamination will result at level of 0.3%.

II.b The measurement method

To estimate the amount of gas leak through the surface between the O-Ring and the the FR4 layer, a pair of aluminum panels with an aluminum honeycomb internal structure (so-called vessel panels) is built. These vessel panels have same shape and dimension of a SM1 MicroMegas drift panel, and they are built with the vacuum bag on a certificate granite table in order to

II. GAS TIGHTNESS TEST OF SM1 MICROMEGAS PANEL

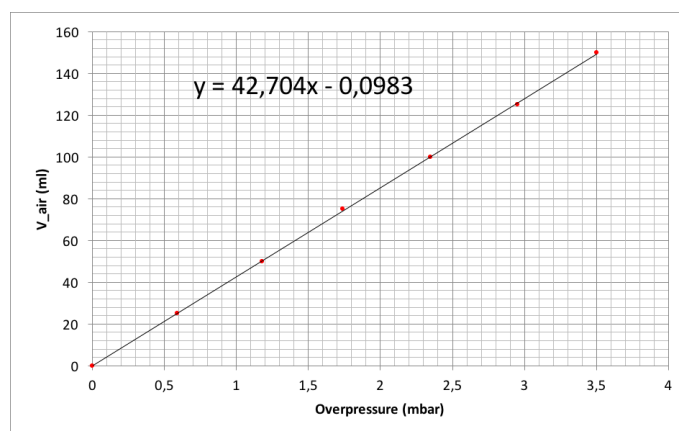


Figure 8: Air volume pushed into the vessel by a syringe as a function of the measured overpressure of the gas gap. The vessel encloses the central panel SM1C-0004. During these measurements the atmospheric pressure and the gas temperature are constant: 1000.2 mbar and 22.5 celsius, respectively.

be flat, moreover they don't have any holes, therefore they are gas tight.

The gas tightness test start enclosing a finalized drift panel (completed of mesh frame, gas-gap frame, interconnection drift spacers, O-Ring) in the vessel. If the SM1 drift panel to test is an external one, then it is paired with one vessel panel; while if the drift panel to test is a central one, it is enclosed inside both vessel panels, but only the gas tightness test is performed to one side per time. The, the gas outlet is closed and the gas-gap formed between the drift panel and the vessel panel is filled, usign the drift panel gas inlet, with air reaching 3 – 4 mbar differential pressure with respect to the exterior. During the test, to stiffer the vessel, avoiding deformations, an exoskeleton is added to the exterior.

The pressure drop is monitored for at least 2 hours. Because the vessel volume changes slightly during the gas fill, to measure the gas leak we have to measure first the overpressure as a function of the amount of air pushed into the chamber. Fig. 8 shows the total volume of air (in ml) pushed into the vessel that contain the central drift panel SM1C-0004, as a function of the overpressure (in mbar) measured at the end of each gas fill. The desired overpressure is reached by steps of 25 ml by means of a 50 ml syringe, as illustrated in Fig. 9.

II. GAS TIGHTNESS TEST OF SM1 MICROME GAS PANEL

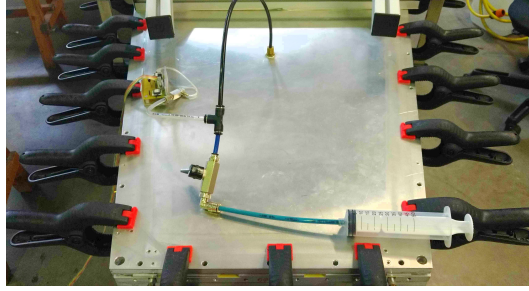


Figure 9: Set up employed to control the air volume pushed into the chamber. Each gas fill was 25 ml. The overpressure has been recorded at the end of each gas fill after 10 s from the filling.

The measurement time interval is normally less than a quarter of hour and during this interval neither the atmospheric pressure nor the temperature have been sensibly changed. The example reported in Fig. 8 refers to $P_{4_{atm}} = 1000.2$ mbar and $T = 295.6$ K and the data points are well represented by the linear equation:

$$V_{air} = 42.7 \cdot \Delta P + 0.098(ml) \quad (9)$$

The amount of air pushed into the chamber to raise its pressure of 1 mbar results equal to about 0.042 liters. For comparison the amount of air necessary to increase the pressure of 1 mbar in one gas-gap of the SM1 MicroMegas quadruplets, which volume is 7.5 l and in the ansatz of volume non-deformable by the overpressure, is 0.0075 l. This means that about 82% of the inserted air increases the initial volume. Moreover, the detector container reacts to the stress due to overpressure as well as an elastic medium. The linear relation between the overpressure (stress) and the increased volume (deformation) demonstrates the elastic behavior of the detector container.

At the end of the air fill of the gas-gap container, the overpressure ΔP is monitored for an adequate time period (> 1 h). The ΔP as a function of time for the central drift panel SM1C-0004 is shown in Fig. 10. In this example the differential pressure increases constantly during all the time period of the measurement (3.7 hours). The reasons of this behavior must be searched in the variation of the environmental conditions and it is crucial to

II. GAS TIGHTNESS TEST OF SM1 MICROMEGAS PANEL

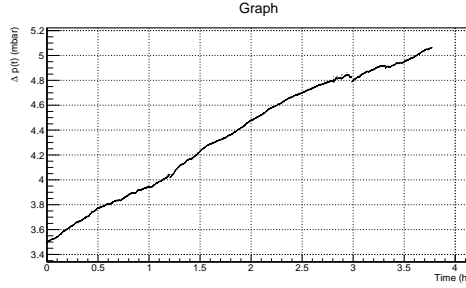


Figure 10: The gas-gap has been filled with 0.15 l of air reaching 3.5 mbar overpressure. Then the differential pressure has been monitored for about 3.7 hours. During this measurement both temperature and atmospheric pressure changed. To extract the correct leak rate from these data it is needed to correct them for the environmental condition variations.

estimate the effects of it to determine correctly the leak rate of the panel. If both temperature and atmospheric pressure do not change during this time interval, the overpressure will show a characteristic decay function and eq. 9 can be used to obtain directly the air leak rate. On the contrary if the environmental conditions change, as in this example, the leak rate must be obtained only after applying the necessary corrections to ΔP . The following sections treats separately the effects of temperature and atmospheric pressure on the overpressure measurements.

II.c Pressure drop correction for temperature

During the differential pressure monitor, the temperature may changes. This temperature variation produces an unexpected change of the internal pressure that it is necessary to evaluate and correct.

The correction can be estimate using the equation of state of ideal gas. If the container is gas tight and the atmospheric pressure doesn't change during the measurement, the internal pressure can change only if the temperature changes. In the example considered here the geometrical gas-gap volume is $V_0 = 7.5 \cdot 10^{-3} m^3$ and that one of the syringe is $(0.15) \cdot 10^{-3} m^3$, the starting temperature is $T_0 = 295.6$ K and the air pressure is the atmospheric one $P_{atm} = 1000.2$ mbar. Using these values it is possible to compute the

II. GAS TIGHTNESS TEST OF SM1 MICROMEGAS PANEL

total number of moles: $n_0 = \frac{(7.5+0.15) \cdot 10^{-3} P_{atm}}{R \cdot T_0} = 0.311$ mole. When the air contained into the syringe is pushed into the gas-gap both the pressure of the air in the gas-gap and the volume of the container increase. The worth of the quantity PV is

$$(PV)_{t=0} = n_0 \cdot R \cdot T_0 \quad (10)$$

The subscript "t=0" stays for the instant at which the air contained into the syringe is pushed into the gas-gap and internal pressure monitor starts. Because, for hypothesis, the container is gas tight and the atmospheric pressure doesn't change during the measurement period, the value of $PV(t)$ can change only if temperature changes

$$PV(t) = n_0 \cdot R \cdot T(t) \quad (11)$$

and the correction to apply to data can be obtained from the difference between eq. 10 and eq. 11

$$(PV)_{t=0} = PV(t) + n_0 \cdot R \cdot [T_0 - T(t)] \quad (12)$$

The quantity $PV(t)$ at generic instant time t is bring back to the value at instant time t=0 when the temperature was T_0 . This quantity can be re-write in the following way

$$(PV)(t) = n(t) \cdot R \cdot T_0 = \frac{[V_0 + V_{syringe}(t)] \cdot P_{atm}}{R \cdot T_0} \cdot R \cdot T_0 \quad (13)$$

where $V_{syringe}(t)$, deduced from eq. 9, is the amount of air to be added into the gas-gap to obtain the measured differential pressure at instant time t. In other words, the quantity $PV(t)$ is expressed in term of number of mole variation. Therefore eq. 12 become

$$(PV)_{t=0} = \frac{[V_0 + V_{syringe}(t)] \cdot P_{atm}}{R \cdot T_0} \cdot R \cdot T_0 + n_0 \cdot R \cdot [T_0 - T(t)] \quad (14)$$

and after some simplifications the quantity PV with the temperature

II. GAS TIGHTNESS TEST OF SM1 MICROMEGAS PANEL

correction is

$$(PV)_{t=0} = [V_0 + V_{syringe}(t)] \cdot P_{atm} + n_0 \cdot R \cdot [T_0 - T(t)] \quad (15)$$

In the gas tightness measurement of the SM1C-0004 drift panel, the gas-gap internal pressure and the air temperature, $\Delta P(t)$ and $T(t)$, are recorded on a text file every 3 seconds using a microcontroller STM32-F03. For every instant time t the overpressure is put in eq. 9 to compute the corresponding amount of the inserted air $V_{air}(t)$. This value and the air temperature are used to compute the first and second term of eq. 15, respectively. Figure 11 shows the behavior of the natural logarithm of the quantity $[V_0 + V_{syringe}(t)] \cdot P_{atm}$ (black dots) and of $\ln(PV)_{t=0}$ computed using the eq. 15 (green dots). The raw data increases with time instead after the temperature correction the data decreases following an exponential relation as expected in the Laminar Leak Model [116]. By this model the leakage takes place in a viscous channel with laminar flow where the leak rate is a linear function of the gauge pressure ($Q_L = s \cdot p$ where s is a scale factor and p is the gauge pressure). The fit of temperature corrected data is performed using the function $\ln PV(t) = at + b$ and the leak rate at $t=0$ is $-0.00072 \cdot e^{7.322} = 1.09 Pa \cdot m^3/h = 3 \cdot 10^{-6} bar \cdot l/s$ and corresponds to the leak rate at 3.5mbar of gauge pressure. To express the leak rate at 3mbar gauge pressure it is necessary to apply the following proportion $\frac{Q_L(p_1)}{p_1} = \frac{Q_L(p_2)}{p_2}$. In this case $Q_L(3mbar) = \frac{Q_L(3.5mbar)}{3.5mbar} \cdot 3mbar = 2.6 \cdot 10^{-6} bar \cdot l/s$. The ATLAS requirements for the gas tightness of the panels is $2.5 \cdot 10^{-6} bar \cdot l/s$.

Instead to present data using eq. 15, it is possible to show them in terms of the air remnant $V_{air}(t)$ from eq. 9. In this way the leak rate is directly given in liter/h at the atmospheric pressure, and it results independent to the inflation of the volume due to the overpressure. The correction to apply to the variable $V_{air}(t)$ to take in consideration the temperature variation can be extracted in the following way. If the gas-gap is gas tight and the temperature doesn't change, the ideal gas law can be written as following

$$P_{atm} \cdot [V_0 + V_{air}^{T_0}(t)] = n_0 \cdot R \cdot T_0 \quad (16)$$

II. GAS TIGHTNESS TEST OF SM1 MICROMEGAS PANEL

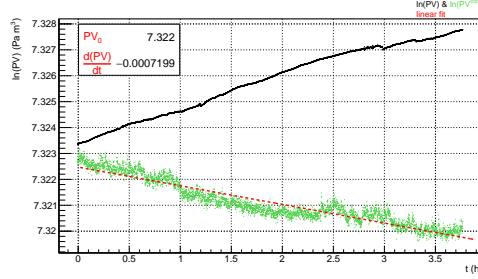


Figure 11: Natural logarithm of the variable PV computed starting from the gas-gap overpressure measurement and the relation between air flow rate and pressure rise into the gas-gap (eq. 9). The raw data are the black dots, instead the data after air temperature correction are the green dots. These last one are well fitted with the function $\ln PV(t) = at + b$.

If the gas-gap is tight but the temperature varies, the eq. 16 become

$$P_{atm} \cdot [V_0 + V_{air}^{T(t)}(t)] = n_0 \cdot R \cdot T(t) \quad (17)$$

being P_{atm} the atmospheric pressure measured at the beginning of the data tacking. Taking the difference between eq. 16 and 17 and using little algebra, the corrected value of lose air volume become

$$V_{air}^{T_0}(t) = V_{air}^{T(t)}(t) + \frac{n_0 \cdot R}{P_{atm}} \cdot [T_0 - T(t)] \quad (18)$$

Figure 12 shows the raw data (black dots) and those after temperature correction (green dots). The last one are fitted with the function $V_{air}(t) = A + Be^{\lambda t}$. The leak rate at $t=0$ amount to $\frac{V_{air}}{dt}|_{t=0} = B \cdot \lambda = 0.19 \text{ ml/min}$ and corresponds to a gauge pressure of 3.5mbar. This result converted to 3mbar gauge pressure gives $Q_L(3\text{mbar}) = 0.16 \text{ ml/min}$. The ATLAS requirements for the panel tightness is $V \cdot 10^{-5} \text{ l/min} = 0.15 \text{ ml/min}$.

Figures 13 shows the positive correlation between the differential pressure of the gas gap with respect to the exterior and the air temperature. Because ΔP depends also from the leak rate and from the atmospheric pressure it is possible to conclude that in this particular case the differential pressure increase with temperature at rate of $\frac{d\Delta P}{dT} = 0.73 \text{ mbar/C}$.

Figures 14 and 15 show the behavior of the room temperature and atmo-

II. GAS TIGHTNESS TEST OF SM1 MICROMEGAS PANEL

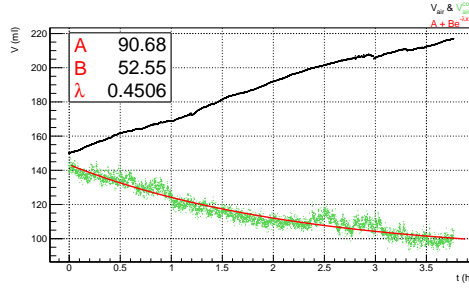


Figure 12: Remnant volume of air pushed into the gas-gap obtained from eq. 9 (black dots) and that one after air temperature correction from eq. 18 (green dots). The data with temperature correction are well fitted with the function $V_{air}(t) = A + Be^{-\lambda t}$.

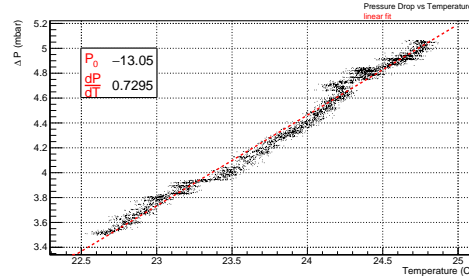


Figure 13: Differential pressure of the gas gap as a function of the environmental temperature. A positive correlation between these two variables is clear.

spheric pressure during the SM1C-0004 gas tight measurement campaign. The air temperature has slowly and continuously increased from 22.5 C and 24.7 C, instead the atmospheric pressure has decreased in average from 1000.0mbar to 997.5mbar.

II.d The atmospheric pressure effect on the gas leak

Due to the elastic behavior of the vessel when the air is pushed into the vessel, changes in atmospheric pressure are almost compensated by the deformation of the vessel itself. When P_{atm} increases/decreases of dP the vessel deforms in order to reduce/enlarge the gas-gap volume and consequently increases/decreases the internal pressure of dP . In other words the effect of

II. GAS TIGHTNESS TEST OF SM1 MICROMEGAS PANEL

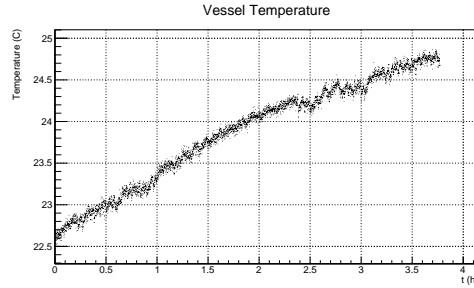


Figure 14: Air temperature during the SM1C-0004 gas tightness test. It rises slowly and continuously during the measurement campaign at constant rate of 0.3 K/h.

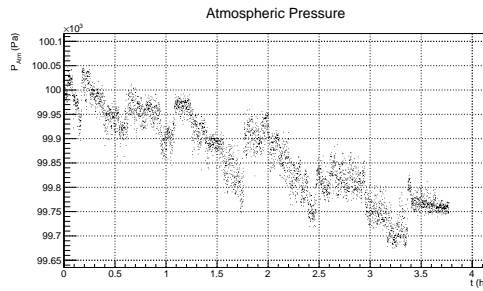


Figure 15: Atmospheric pressure during the SM1C-0004 gas tightness test. It decreases slowly and continuously during the measurement campaign at constant rate of 0.67 mbar/h. The sharp jumps are due to the resolution of the ADC employed to acquire the barometric sensor.

II. GAS TIGHTNESS TEST OF SM1 MICROMEGAS PANEL

atmospheric pressure is to vary the gas-gap volume and consequently the internal pressure, but in such a way that the internal pressure balances the external one, leaving the difference practically unchanged. It should be said that the gas leak changes with absolute internal pressure because both density and velocity of molecules change and consequently the probability of escaping from the volume through the gas leak holes. The effect is under study and at present it is considered a second order correction.

References

- [1] F. Mandl and G. Shaw, *Quantum Field Theory*. John Wiley and Sons, 2013.
- [2] Aitchison and Hey, *Gauge Theories in Particle Physics: a practical introduction*. University of Minnesota, 1989.
- [3] M. Gell-Mann, *The Quark and the Jaguar: Adventures in the Simple and the Complex*. 1995.
- [4] E. Amaldi, *From the discovery of the neutron to the discovery of nuclear fission*. 1984, vol. 111, pp. 1–331.
- [5] Donald H. Perkins, *Introduction to High Energy Physics*. Cambridge University Press, 2000.
- [6] B. Povh, *Particles and Nuclei: an introduction to the physical concepts*. Springer.
- [7] A. N. Schellekens, *Beyond the Standard Model*, <https://www.nikhef.nl/~t58/BSM.pdf>, 2017.
- [8] Jegerlehner, “The hierarchy problem of the electroweak standard model revisited”, *ArXiv e-prints*, 2013, <http://arxiv.org/abs/1305.6652>.
- [9] T. e. a. Blum, “The muon (g-2) theory value: present and future”, 2013. eprint: [1311.2198](https://arxiv.org/abs/1311.2198).
- [10] CERN, *Dark matter*, <https://home.cern/about/physics/dark-matter>.
- [11] M. Ackermann *et al.*, “Searching for Dark Matter Annihilation from Milky Way Dwarf Spheroidal Galaxies with Six Years of Fermi Large Area Telescope Data”, *Phys. Rev. Lett.*, vol. 115, no. 23, p. 231 301, 2015.
- [12] Adriani and et al., “An anomalous positron abundance in cosmic rays with energies 1.5-100gev”, 2009, <http://arxiv.org/abs/0810.4995v1>.

REFERENCES

- [13] Joshua Thomas Ruderman, “Light Hidden Sectors: Dark Matter and Lepton Jets”, <https://www.princeton.edu/physics/graduate-program/theses/theses-from-2011-1/j.rudermanthesis.pdf>, PhD thesis, Princeton University, 2011.
- [14] *Large Hadron Collider*, <http://www.pindex.com/b/curiosity/large-hadron-collider>.
- [15] ATLAS Collaboration, *Luminosity summary plots for Run-2 ATLAS data taking*, <https://twiki.cern.ch/twiki/bin/view/AtlasPublic/LuminosityPublicResultsRun2>.
- [16] L. Evans and P. Bryant, “Lhc machine”, *Journal of Instrumentation*, 2008, <http://jinst.sissa.it/LHC/>.
- [17] T. S. Pettersson and P. Lefevre, “The large hadron collider: conceptual design”, Tech. Rep. CERN-AC-95-05 LHC, 1995, <http://cdsweb.cern.ch/record/291782>.
- [18] ATLAS Collaboration, *ATLAS: technical proposal for a general purpose pp experiment at the Large Hadron Collider at CERN*, ser. LHC Tech. Proposal. 1994, <http://cds.cern.ch/record/290968>.
- [19] ALICE Collaboration, *Technical proposal for A Large Ion Collider Experiment at the CERN LHC*, ser. LHC Tech. Proposal. 1995, <http://cds.cern.ch/record/293391/files/cer-000214817.pdf>.
- [20] CMS Collaboration, *Technical proposal*, ser. LHC Tech. Proposal. 1994, <https://cds.cern.ch/record/290969>.
- [21] LHCb Collaboration, *LHCb : Technical Proposal*, ser. Tech. Proposal. Geneva: CERN, 1998, <https://cds.cern.ch/record/622031>.
- [22] CERN, *The accelerator complex*, <https://home.cern/about/accelerators>.
- [23] *Atlas experiment*, <http://atlas.cern/discover/physics>.
- [24] M. Del Gaudio, *Detection efficiency for Hidden Valley Lepton Jets using ATLAS detector at LHC*, Master Thesis, 2013/2014.

REFERENCES

- [25] D. Griffiths, *Introduction to elementary particles*, ser. Physics Textbook. Wiley, 1987.
- [26] A. Venturini, “Searching for dark matter in the mono-jet channel with the atlas detector”, PhD thesis, Brandeis University, 2016.
- [27] Wikipedia, *Pseudorapidity*, <https://en.wikipedia.org/w/index.php?title=Pseudorapidity&oldid=799351373>, 2017.
- [28] ATLAS Collaboration, *ATLAS Magnet System*, <https://atlas.cern/discover/detector/magnet-system>.
- [29] —, *ATLAS central solenoid: technical design report*, ser. Technical Design Report ATLAS. 1997, <https://cds.cern.ch/record/331067>.
- [30] —, “ATLAS barrel toroid: Technical design report”, 1997.
- [31] —, “Atlas endcap toroids: technical design report”, 1997.
- [32] H. Herman and J. ten Kate, “ATLAS Superconducting Magnet System Performance”, *Preprint paper*, vol. LX, 2006, <https://edms.cern.ch/file/774395/ASC2006-1LX02-preprint.pdf>.
- [33] ATLAS Collaboration, “The ATLAS Experiment at the CERN Large Hadron Collider”, *Journal of Instrumentation*, 2008, <http://jinst.sissa.it/LHC/>.
- [34] —, *ATLAS inner detector: Technical Design Report, 1*, ser. Technical Design Report ATLAS. 1997, <http://cds.cern.ch/record/331063>.
- [35] Wermes, Norbert and Hallewel, *ATLAS pixel detector: Technical Design Report*, ser. Technical Design Report ATLAS. 1998, <https://cds.cern.ch/record/381263?ln=it>.
- [36] M. Capeans and G. e. a. Darbo, “ATLAS Insertable B-Layer Technical Design Report”, Tech. Rep. CERN-LHCC-2010-013. 2010, <http://cds.cern.ch/record/1291633>.
- [37] ATLAS Collaboration, *The Inner Detector*, <https://atlas.cern/discover/detector/inner-detector>.

REFERENCES

- [38] E. Abat, T. N. Addy, and Akesson, “The ATLAS Transition Radiation Tracker (TRT) proportional drift tube: design and performance”, *J. Instrum.*, vol. 3, P02013, 2008, <https://cds.cern.ch/record/1094549?ln=it>.
- [39] M. V.A., “The ATLAS Transition Radiation Tracker”, http://people.na.infn.it/~elly/TesiAtlas/SeminariAtlas/Detector/Bibliografia/Atlas_TRT.pdf, 2013.
- [40] ATLAS Collaboration, *ATLAS Calorimeter*, <https://atlas.cern/discover/detector/calorimeter>.
- [41] P. Schwemling, “ATLAS electromagnetic calorimetry and performance of electron/photon detection”, *Eur. Phys. J. C*, vol. 34, s129–s137, 2004, <https://cds.cern.ch/record/807238?ln=it>.
- [42] Z. Meng, “Performance of the ATLAS liquid argon calorimeter”, <http://dx.doi.org/10.3204/DESY-PROC-2010-01/meng>, 2010.
- [43] B. Caron, “Hadronic Calorimetry and $\text{Jet}/\tau/E_T^{\text{miss}}$ Performance Studies in ATLAS”, 2003, <https://cds.cern.ch/record/676895?ln=it>.
- [44] ATLAS Collaboration, *ATLAS tile calorimeter: Technical Design Report*, ser. Technical Design Report ATLAS. 1996, <https://cds.cern.ch/record/331062>.
- [45] —, *ATLAS muon spectrometer: Technical Design Report*, ser. Technical Design Report ATLAS. 1997, <https://cds.cern.ch/record/331068>.
- [46] A. Policicchio, “Study of rare beauty decays with ATLAS detector at LHC and MDT chamber performance”, PhD thesis, Università della Calabria, 2006.
- [47] ATLAS Collaboration, *Atlas muon spectrometer*, <https://atlas.cern/discover/detector/muon-spectrometer>.
- [48] K. Nikolopoulos *et al.*, “Cathode strip chambers in ATLAS : Installation, commissioning and in situ performance”, in *Proceedings, NSS/MIC 2008 / RTSD 2008): Dresden, Germany*, 2008, pp. 2819–2824.

REFERENCES

- [49] G. Cattani and the RPC group, “The resistive plate chambers of the atlas experiment: performance studies”, *Journal of Physics: Conference Series*, 2011, <http://stacks.iop.org/1742-6596/280/i=1/a=012001>.
- [50] G. Chiodini, N. Orlando, and S. Spagnolo, “ATLAS RPC time-of-flight performance”, CERN, Tech. Rep. ATL-MUON-PROC-2012-002, 2012, <https://cds.cern.ch/record/1437020>.
- [51] G. Chiodini and S. Spagnolo, “Off-line time calibration of the ATLAS RPC system”, CERN, Tech. Rep. ATL-MUON-PROC-2012-008, 2012, <https://cds.cern.ch/record/1491576>.
- [52] D. Caforio, “The ATLAS Forward Detectors - LUCID, ALFA and AFP: Past, Present and Future”, 2013, <https://cds.cern.ch/record/1514203?ln=it>.
- [53] Viazlo, Oleksandr and ATLAS LUCID Collaboration, “ATLAS LUCID detector upgrade for LHC Run 2”, Tech. Rep. ATL-FWD-PROC-2015-004, 2015, <https://cds.cern.ch/record/2062038>.
- [54] Lasagni Manghi, F. and ATLAS LUCID Collaboration, “The LUCID detector ATLAS luminosity monitor and its electronic system”, Tech. Rep. ATL-FWD-PROC-2015-003, 2015, <http://cds.cern.ch/record/2027724>.
- [55] Ruiz-Martinez, A. and ATLAS Collaboration, “The Run-2 ATLAS Trigger System”, Tech. Rep. ATL-DAQ-PROC-2016-003, 2016, <https://cds.cern.ch/record/2133909>.
- [56] F. Pastore, “The ATLAS Trigger System: Past, Present and Future”, *Nucl. Part. Phys. Proc.*, vol. 273-275, pp. 1065–1071, 2016.
- [57] “Letter of Intent for the Phase-I Upgrade of the ATLAS Experiment”, CERN, Tech. Rep. CERN-LHCC-2011-012, 2011, <https://cds.cern.ch/record/1402470>.
- [58] M. e. a. Shochet, “Fast TracKer (FTK) Technical Design Report”, Tech. Rep. CERN-LHCC-2013-007. ATLAS-TDR-021, 2013, <https://cds.cern.ch/record/1552953>.

REFERENCES

- [59] T. Kawamoto, S. Vlachos, and L. e. a. Pontecorvo, “New Small Wheel Technical Design Report”, Tech. Rep. CERN-LHCC-2013-006. ATLAS-TDR-020, 2013, <https://cds.cern.ch/record/1552862>.
- [60] L. e. a. Adamczyk, “Technical Design Report for the ATLAS Forward Proton Detector”, Tech. Rep. CERN-LHCC-2015-009. ATLAS-TDR-024, 2015, <https://cds.cern.ch/record/2017378>.
- [61] M. e. a. Aleksa, “ATLAS Liquid Argon Calorimeter Phase-I Upgrade Technical Design Report”, Tech. Rep. CERN-LHCC-2013-017. ATLAS-TDR-022, 2013, <https://cds.cern.ch/record/1602230>.
- [62] ATLAS Collaboration, “Technical Design Report for the Phase-I Upgrade of the ATLAS TDAQ System”, Tech. Rep. CERN-LHCC-2013-018. ATLAS-TDR-023, 2013, <https://cds.cern.ch/record/1602235>.
- [63] “ATLAS Trigger and Data Acquisition Phase-II Upgrade Technical Design Report”, CERN, Tech. Rep., 2017, <https://cds.cern.ch/record/2055248>.
- [64] G. Iakovidis and T. Alexopoulos, “Research and development in Micromegas detector for the ATLAS Upgrade”, <https://cds.cern.ch/record/1955475>, PhD thesis, 2014.
- [65] F. Jeanneau, “Design and construction of large size Micromegas chambers for the ATLAS upgrade of the Muon Spectrometer”, CERN, Tech. Rep., 2016, <https://cds.cern.ch/record/2196546>.
- [66] M. Vanadia, “Study of the performance of the Micromegas chambers for the ATLAS Muon Spectrometer Upgrade”, 2015, <https://cds.cern.ch/record/2010490>.
- [67] P. Lösel and R. Müller, “Design and Construction of Large Size Micromegas Chambers for the Upgrade of the ATLAS Muon Spectrometer”, Tech. Rep., 2015, <https://cds.cern.ch/record/2042404>.
- [68] P. D. Group, “Review of particle physics”, *Phys. Rev. D*, vol. 86, 1 2012, <https://link.aps.org/doi/10.1103/PhysRevD.86.010001>.

REFERENCES

- [69] Giomataris, Y. and Rebourgeard, P. and Robert, J. P. and Charpak, Georges, “Micromegas: a high granularity position sensitive gaseous detector for high particle flux environments”, *Nucl. Instrum. Meth.*, vol. A376, pp. 29–35, 1996, <https://cds.cern.ch/record/299159>.
- [70] Del Gaudio, M., “Search for long-lived neutral particles decaying into Lepton-Jets with the ATLAS detector in proton-proton collision data at $\sqrt{s} = 13$ TeV”, Tech. Rep. ATL-COM-PHYS-2017-1211, 2017, <https://cds.cern.ch/record/2279925>.
- [71] T. Ferbel, *Experimental techniques in high-energy nuclear and particle physics*. Singapore, 1991, <https://books.google.it/books>.
- [72] M. Del Gaudio, “The INFN MicroMegas Module-0 Prototype for the Muon Spectrometer upgrade of the ATLAS Experiment”, 2016, <http://cds.cern.ch/record/2233687>.
- [73] M. Iodice, “Resistive Micromegas for the Muon Spectrometer Upgrade of the ATLAS experiment”, CERN, Tech. Rep., 2016, <https://cds.cern.ch/record/2231836>.
- [74] A. e. a. Kourkoumeli-Charalampidi, “Construction and QA/QC of the Micromegas Pavia Readout Panels for the Muon Spectrometer Upgrade of the ATLAS New Small Wheel”, Tech. Rep. ATL-MUON-PROC-2016-014, 2016, <https://cds.cern.ch/record/2238629>.
- [75] Hashemi, K. S., “Pixel CCD Rasnik DAQ”, CERN, Tech. Rep., 1997, <http://cds.cern.ch/record/685581>.
- [76] Rome1, “The vacuum bag technique for the MicroMega panel construction.”, Tech. Rep. ATL-COM-MUON-2014-024, 2014, <https://cds.cern.ch/record/1692626>.
- [77] G. Ciapetti, M. Del Gaudio, M. Diamond, S. Giagu, R. Les, A. Policichio, M. Schioppa, M. Testa, and M. Verducci, “Search for long-lived neutral particles decaying into displaced lepton jets in proton-proton collisions at $\sqrt{s} = 13$ TeV with the ATLAS detector”, Tech. Rep. ATL-COM-PHYS-2016-924, 2016, <https://cds.cern.ch/record/2199400>.

REFERENCES

- [78] ATLAS Collaboration, “Search for long-lived neutral particles decaying into lepton jets in proton-proton collisions at $\sqrt{s} = 8$ TeV with the ATLAS detector”, 2014, <http://arxiv.org/abs/1409.0746>.
- [79] A. Falkowski, J. T. Ruderman, and Volansky, “Discovering Higgs Boson Decays to Lepton Jets at Hadron Colliders”, *Physical Review Letters*, 2010, <http://arxiv.org/abs/1007.3496>.
- [80] ATLAS Collaboration, “Search for Higgs boson decays to Beyond-the-Standard-Model light bosons in four-lepton events with the ATLAS detector at $\sqrt{s} = 13$ TeV”, Tech. Rep., 2017, <http://cds.cern.ch/record/2273848>.
- [81] Curtin, D. et al., “Exotic decays of the 125 gev higgs boson”, *Phys. Rev. D*, vol. 90, 7 2014, <https://link.aps.org/doi/10.1103/PhysRevD.90.075004>.
- [82] Alexander, J. et al, “Dark sectors 2016 workshop: community report”, <https://inspirehep.net/record/1484628/files/arXiv:1608.08632.pdf>, 2016. arXiv: 1608.08632.
- [83] A. Falkowski, J. T. Ruderman, and Volansky, “Hidden higgs decaying to lepton jets”, *Journal of High Energy Physics*, 2010, <http://arxiv.org/abs/1002.2952>.
- [84] T. Han, Z. Si, K. M. Zurek, and M. J. Strassler, “Phenomenology of hidden valleys at hadron colliders”, *Journal of High Energy Physics*, 2008, <http://arxiv.org/abs/0712.2041v2>.
- [85] Andreas, S. and Ringwald, A., “Status of sub-gev hidden particle searches”, 2010, <https://inspirehep.net/record/866276>.
- [86] Cheung, C. and Ruderman, J. T. and Wang, L. and Yavin, I., “Kinetic mixing as the origin of a light dark-gauge-group scale”, *Phys. Rev. D*, vol. 80, 3 2009, <https://link.aps.org/doi/10.1103/PhysRevD.80.035008>.
- [87] B. Batell, M. Pospelov, and A. Ritz, “Probing a secluded u(1) at B factories”, *Phys. Rev. D*, vol. 79, 11 2009, <https://link.aps.org/doi/10.1103/PhysRevD.79.115008>.

REFERENCES

- [88] M. Schioppa, “Search for long-lived neutral particles decaying into lepton-jets in 20.3 fb^{-1} proton-proton collisions at $\sqrt{s} = 8 \text{ TeV}$ with the ATLAS detector”, Tech. Rep. ATL-PHYS-PROC-2015-195, 2015, <https://cds.cern.ch/record/2117068>.
- [89] A. Policicchio, “Search for long-lived neutral particles decaying into lepton-jets with the ATLAS detector in proton-proton collision data at $\sqrt{s} = 13 \text{ TeV}$ ”, Tech. Rep. ATL-PHYS-PROC-2016-176, 2016, <https://cds.cern.ch/record/2226421>.
- [90] Strassler, M. J. and Zurek, K. M., “Discovering the Higgs through highly-displaced vertices”, *Physics Letters B*, vol. 661, no. 4, pp. 263–267, 2008, <http://www.sciencedirect.com/science/article/pii/S0370269308001846>.
- [91] S. Andreas, “Dark Forces and Dark Matter in a Hidden Sector”, K. Zioutas and M. Schumann, Eds., <http://arxiv.org/abs/1110.2636>, 2012.
- [92] —, “Update on hidden sectors with dark forces and dark matter”, 2012, <http://arxiv.org/abs/1211.5160>.
- [93] D. Curtin, Essig, and et al., “Exotic Decays of the 125 GeV Higgs Boson”, 2013, <http://arxiv.org/abs/1312.4992>.
- [94] G. Ciapetti, M. Del Gaudio, M. Diamond, S. Giagu, R. Les, A. Policicchio, M. Schioppa, M. Testa, and M. Verducci, “Search for long-lived neutral particles decaying into lepton jets in proton-proton collisions at $\sqrt{s} = 13 \text{ TeV}$ with the ATLAS detector”, CERN, Tech. Rep. ATL-COM-PHYS-2016-010, 2016, <https://cds.cern.ch/record/2119557>.
- [95] Sjostrand, T. and Mrenna, S. and Skands, P. Z., “A Brief Introduction to PYTHIA 8.1”, *Comput. Phys. Commun.*, vol. 178, pp. 852–867, 2008, <https://arxiv.org/pdf/0710.3820.pdf>.
- [96] J. Alwall and H. et al., “Madgraph 5: going beyond”, *JHEP*, vol. 06, p. 128, 2011, <https://arxiv.org/pdf/1106.0522.pdf>.

REFERENCES

- [97] S. Agostinelli, J. Allison, K. Amako, and et al., “Geant4 a simulation toolkit”, *Nuclear Instruments and Methods in Physics Research*, 2003, <http://www.sciencedirect.com/science/article/pii/S0168900203013688>.
- [98] ATLAS Collaboration, “Selection of jets produced in 13 TeV proton-proton collisions with the ATLAS detector.”, CERN, Tech. Rep. ATL-CONF-2015-029, 2015, <https://cds.cern.ch/record/2037702>.
- [99] —, “Jet Calibration and Systematic Uncertainties for Jets Reconstructed in the ATLAS Detector at $\sqrt{s} = 13$ TeV”, CERN, Tech. Rep. ATL-PHYS-PUB-2015-015, 2015, <https://cds.cern.ch/record/2037613>.
- [100] G. Aad, B. Abbott, Abdallah, and et al., “Triggering on long-lived neutral particles in the ATLAS detector”, CERN, Geneva, Tech. Rep., 2009, <http://cds.cern.ch/record/1175196?ln=it>.
- [101] “Triggers for displaced decays of long-lived neutral particles in the atlas detector”, *Journal of Instrumentation*, 2013, <http://arxiv.org/pdf/1305.2284v2.pdf>.
- [102] G. Ciapetti, M. Del Gaudio, M. Diamond, S. Giagu, R. Les, A. Policicchio, M. Schioppa, M. Testa, and M. Verducci, “Expected performance for displaced Lepton Jets: ATLAS trigger and reconstruction efficiency in LHC 2015 run.”, Tech. Rep. ATL-COM-PHYS-2016-272, 2016, <https://cds.cern.ch/record/2140313>.
- [103] Ciapetti, G. and Del Gaudio, M. and Giagu, S. and Policicchio, A. and Schioppa M., “Displaced Lepton Jets search. Efficiency tables for gamma dark reconstruction in ATLAS”, Tech. Rep. ATL-COM-PHYS-2015-248, 2015.
- [104] ATLAS Collaboration, “Beam-induced and cosmic-ray backgrounds observed in the atlas detector during the lhc 2012 proton-proton running period”, *JINST*, vol. 11, no. CERN-EP-2016-029, 2016, <https://cds.cern.ch/record/2141086>.

REFERENCES

- [105] —, “Characterisation and mitigation of beam-induced backgrounds observed in the atlas detector during the 2011 proton-proton run”, *JINST*, vol. 8, 2013, <https://cds.cern.ch/record/1523620>.
- [106] *Atlas experiment photos*, <http://atlasexperiment.org/photos/events-beam-halo.html>.
- [107] Aad, Georges and others, “Performance of pile-up mitigation techniques for jets in p-p collisions at $\sqrt{s} = 8$ tev using the atlas detector”, *Eur. Phys. J.*, vol. C76, no. 11, p. 581, 2016, <https://arxiv.org/abs/1510.03823>.
- [108] Hoecker, A. and Speckmayer, P. and others, “Toolkit for multivariate data analysis”, *ArXiv Physics and Probability*, 2007, <https://arxiv.org/abs/physics/0703039>. eprint: [physics/0703039](https://arxiv.org/abs/physics/0703039).
- [109] ATLAS Collaboration, “Jet calibration and systematic uncertainties for jets reconstructed in the atlas detector at $\sqrt{s} = 13$ tev”, CERN, Tech. Rep., 2015, <http://cds.cern.ch/record/2037613>.
- [110] ATLAS statistics forum, *Abcd method in searches*, <https://twiki.cern.ch/twiki/pub/AtlasProtected/ATLASStatisticsFAQ/ABCD.pdf>.
- [111] A. statistics forum, “Extensions to the frequentist recommendation”, 2014, <https://twiki.cern.ch/twiki/pub/AtlasProtected/StatisticsTools/ExtendedStatForumRecommendations.pdf>.
- [112] D. M., “Search for dark gauge bosons decaying into displaced lepton-jets in proton-proton collisions at $\sqrt{s} = 13$ TeV with the ATLAS detector”, PhD thesis, University of Toronto, 2017.
- [113] A. L. Read, “Presentation of search results: the CL_s technique”, *J. Phys. G*, vol. 28, no. 10, 2002, <https://cds.cern.ch/record/722145>.
- [114] A. J. Krasznahorkay *et al.*, “Observation of anomalous internal pair creation in be8: a possible indication of a light, neutral boson”, *Phys. Rev. Lett.*, vol. 116, no. 4, 2016, <https://arxiv.org/abs/1504.01527>.

REFERENCES

- [115] L. Landau, “On the energy loss of fast particles by ionization”, *J. Phys. (USSR)*, vol. 8, pp. 201–205, 1944.
- [116] T. Alexopoulos, E. Gazis, M. Iodice, S. Maltezos, G. Sekhniaidze, A. Antoniou, and G. Koutelieris, “Determination of the feasible gas sealing level of the NSW Micromegas quadruplets”, CERN, Tech. Rep., 2017, <https://cds.cern.ch/record/2252456>.
- [117] Weinberg Steven, “A model of leptons”, *Phys. Rev. Lett.*, vol. 19, 1264–1266, 1967, <http://link.aps.org/doi/10.1103/PhysRevLett.19.1264>.
- [118] M. J. Strassler and K. M. Zurek, “Echoes of a hidden valley at hadron colliders”, *Physics Letters B*, 2007, <http://arxiv.org/abs/hep-ph/0604261v2>.
- [119] H. Petra, “The ATLAS Silicon Microstrip Tracker”, Tech. Rep. ATL-INDET-PROC-2010-036, 2010, <https://cds.cern.ch/record/1305173?ln=it>.

Declaration

I herewith declare that I have produced this paper without the prohibited assistance of third parties and without making use of aids other than those specified; notions taken over directly or indirectly from other sources have been identified as such. This paper has not previously been presented to any other Italian or foreign examination board.

The thesis work was conducted from 2014 to 2017 under the supervision of prof. Marco Schioppa.

Cosenza - Università della Calabria, November 2017

Acknowledgements

Versione italiana:

Ringrazio il Prof. Marco Schioppa per avermi insegnato il mestiere del fisico e per il supporto che sempre mi ha dato. Scrivere una tesi è il risultato di anni di ricerca e lo ringrazio per avermi seguita in ogni fase.

Ringrazio il Dr. Antonio Policicchio per la disponibilità e la gentilezza con cui ha risposto alle troppe mie domande, ma anche gli altri colleghi del gruppo UEH-LLP-LJ: M. Diamond, S. Giagu, R. Les, D. Salvatore, C. Sebastiani, M. Testa, M. Verducci.

Devo ringraziare anche l'intero gruppo NSW Italia: Cosenza, Lecce, Frascati, Napoli, Pavia, Roma1, Roma3 con cui ho avuto la possibilità di lavorare in questi tre anni e scoprire quanto lavoro si nasconde dietro la realizzazione di un esperimento, grazie anche per il calore umano che è necessario per sopravvivere ore in camera pulita.

Grazie a tutto il gruppo NSW. In particolare, grazie ai Proff. Theodoros Alexopoulos e Stavros Maltezos (National Technical University of Athens) per le conversazioni private e le dettagliate spiegazioni riguardo le performance e la modellizzazione del gas leak nei rivelatori MicroMegas. Grazie anche alla Dr. Kim Temming (Friburgo) senza le nostre chiacchierate su Skype ad ogni ora del giorno (e della notte) starei ancora impazzendo sul DataBase!

Voglio ringraziare Paola Turco per il buonumore che ogni giorno porta in ufficio, ma anche i miei nuovi colleghi Alessandro e Giovandomenico.

Soprattutto ringrazio il Prof. Guido Ciapetti che mi ha mostrato l'umiltà che solo i grandi scienziati possiedono.

ACKNOWLEDGEMENTS

Ringrazio la mia famiglia che mi ha sempre supportato: mio padre Tonino che fin da piccola ha stimolato la mia curiosità, mia madre Anna che mi è sempre stata accanto, e mio fratello Domenico che sento vicino anche a chilometri di distanza.

Ringrazio Leonardo che crede in me più di quanto faccia io, e la sig. Rita e il sig. Tonino che negli anni sono diventati la mia seconda famiglia.

Ringrazio Francesco & Francesco che hanno reso fantastici gli anni a Cosangeles, ma anche le persone sulla cui amicizia posso sempre contare: Francesca Cuteri, e i suoi saggi consigli, Emilia Russo e i cornetti a fine serata.

E perchè no, grazie anche a me stessa per l'impegno che ho sempre messo nel fare il lavoro più bello del mondo.

English version:

I thank Prof. Marco Schioppa who thought me the real work of a experimental physics and for the support he always gave me. Writing a thesis is the result of years of study and research and I have to thank him to be present in each moment.

Thanks to Dr. Antonio Policicchio: he answers all my questions with patience and kindness, but also thank to the other members of the UEH-LLP-LJ group: M. Diamond, S. Giagu, R. Les, D. Salvatore, C. Sebastiani, M. Testa, M. Verducci.

I have to thank the whole NWS Italian group: Cosenza, Lecce, Frascati, Napoli, Pavia, Roma¹ and Rome³. I had the change to work with you in the past three years and I discovered how much work is needed to build an experiment. Moreover thanks for your humanity which is important when you spent so many hours in a clean room!

Thanks to all the members of the international community NWS Project. In particular, I would like to thank Prof. Theodoros Alexopoulos and Prof.

ACKNOWLEDGEMENTS

Stavros Maltezos (National Technical University of Athens) for all the precious explanations regarding the performance and the gas leak modelling of MicroMegas detectors. Thanks also to the Dr. Kim Temming (Freiburg), without our morning (and nightly) Skype discussions I was still going crazy on the Logistic DB!

Thanks to Paola Turco, every morning she carries cheerfulness in the office, and thanks also to my new colleagues Alessandro Alessio and Giovandomenico Carducci.

Above all I thank to Prof. Guido Ciapetti: he showed the humbleness that only the great scientist have.

I thank my family who always supported me: my dad Tonino teased my curiosity since childhood, my mum Anna always by my side and my little brother Domenico so close even to miles away.

I thank Leonardo who believes in me more than I do, and thank to Mrs. Rita and Mr. Tonino a kind of my second family.

I thank Francesco & Francesco for the amazing years we spent in Cosenza, and also thanks to truly friends: Francesca Cuteri with her wise advices, Emilia Russo for her special nightly-croissants.

And why not! I thank my self for the commitment I put in the most beautiful job of the world.